nature portfolio

Peer Review File

Heterogeneous photonic integration of single-crystalline nanomembranes

Corresponding Author: Professor Sang-Hoon Bae

This file contains all reviewer reports in order by version, followed by all author rebuttals in order by version.

Version 0:

Reviewer comments:

Referee #1

(Remarks to the Author)
The manuscript presents an ambitious and compelling vision of “photonic Lego” based on van der Waals (vdW) integration of diverse functional nanomembranes. The concept of vdW integration was originally developed for atomically thin or quasi–atomically thin material systems, where interlayer interactions are dominantly governed by vdW forces. In this work, however, functional membranes, such as BTO, CFO, and GaAs with thicknesses ranging from several tens to over one hundred nanometers, were transferred to silicon photonics platform, enabling functionalities like EO modulation, non-reciprocity, and photodetection that are otherwise not accessible in native silicon. The authors performed a very comprehensive investigation that starts from material synthesis and characterization, to heterogeneous vdW integration, device fabrication, and functional testing, on a variety of material systems. Results suggest that the transferred materials have largely maintained their good native crystalline properties. The measured device performances, although not record-breaking, are also compelling especially compared with other previous heterogeneous integration methods.

My main concern is regarding the most critical innovation in the paper, which I hope the authors could more clearly discuss. The concept of vdW integration has been hot in recent years due to its powerfulness in 2D material engineering, but I would argue that almost any heterogeneous integration approaches that already exist in the integrated photonics community are based on vdW interactions too, e.g. existing wafer or die bonding techniques between III-V, LN/LT and Si/SiO2. In my understanding, the main difference between the current and these past works lies in the way that the thin films were exfoliated, e.g. via 2DLT and ELO methods. Between these two methods, 2DLT is a recently emerging and interesting one, while ELO based on wet etching of sacrificial layer seems to have been adopted in III-V thin-film preparation for quite some time. However, if I understand correctly most of the actual devices demonstrated in this work were prepared using the more traditional ELO method. Apart from vdW and thin-film preparation, the achieved device performances are not exotic; the prospect for multi-layer stacking is interesting, but it is unclear what application would require such stacks. To summarize, I believe the achieved material properties in the final devices in this paper are good, and the method is general and proven applicable to a variety of materials, but it is unclear what is the key innovation here that has enabled these.

Apart from this main concern, I hope the authors could also address the following technical comments:

1. Following my comment above, I hope the authors could more explicitly point out the membrane preparation methods (2DLT or ELO) for each material. At the moment the information is scattered here and there but difficult to find.

2. The authors have quoted several times the extracted EO coefficient being 40 times higher than LN. However, the finally achieved device Vpi-L values, which users care about at the end of the day, are not improved by such a dramatic value (~ 8 times for low-speed device and almost comparable for the high-speed device). The authors have attributed the increased Vpi-L in high-speed case to fabrication imperfections in the electrodes, which may have played a role; but I believe more of this trade-off originated from the large dielectric constant of BTO that pose challenges in RF design. It is also well known that BTO’s EO coefficient drops at higher frequency, which may have also been a critical limiting factor of the EO bandwidth. These trade-offs, although not having much to do with the heterogeneous integration method proposed in this paper, should be discussed in more details.

3. Similar to the above comment, the authors have mainly quoted the extracted Faraday rotation coefficient of the MO material, but it would be beneficial if the authors could directly compare the device performance (e.g. NRPS) with previous reports. It is also important to include and compare the propagation loss of the device with previous works.

4. For the BTO device, the measured additional propagation loss is 2.5 dB/cm, which is quite substantial. Please comment on the origin of this extra loss. Since this device does not involve patterning BTO, I would assume this came from material itself, which raises questions on the material quality prepared using the proposed method, as recent papers have demonstrated propagation loss as low as 0.32 dB/cm in etched BTO devices (arXiv:2507.17150).

5. For the photodetectors, the dark currents are not explicitly quoted but looking from the figures they seem to be not particularly low. Please quote the numbers and discuss potential causes in more details.

6. The experiment of vertical stacking EO and MO nanomembranes is interesting. Could the authors provide more discussions on the potential application scenes of this?

Typo: Section 3, paragraph 3, first line, “Here we report…”

Referee #2

(Remarks to the Author)
I co-reviewed this manuscript with one of the reviewers who provided the listed reports.

Referee #3

(Remarks to the Author)
The paper presents a scheme to heterogeneously integrate multiple crystalline membranes onto silicon and silicon nitride photonics for a variety of applications which include high-speed modulation, non-reciprocal magneto-optic isolators, and photodetection. This comprises of variety of different epitaxially grown crystalline materials on different substrates: thin-film barium titanate (BTO), cobalt ferrite (CFO) and yttrium iron garnet (YIG), gallium nitride (GaN) and gallium arsenide (GaAs). While all these materials have previously been heterogeneously integrated onto Si and SiN photonic circuits, the real advance here is the nature of remote epitaxy demonstrated where each crystalline thin-film can be easily separated from its host substrate with relative ease using techniques of epitaxial lift-off (ELO) and 2D-materials-assisted layer transfer (2D-LT). In many cases, the substrate removal process after hetero-integration via bonding (i.e. van der Waals) is a real challenge and detrimental to the core bond itself. There is no real substitute to crystalline thin-film quality from growth on native substrate. Direct growth on photonic platforms results in poor amorphous or at best poly-crystalline films with low yield and performance compared to their crystalline counterparts.

While this work focused on remote-epitaxial transfer of thin-films for photonic applications is of note, the manuscript can benefit from the below feedback.

1. One of the main claims of this paper is the reduction of defect density in this approach of remote epitaxy transfer compared to other methods. It would be useful to characterize both local and global defect density of all these thin-film materials with sacrificial layers compared to growth on native substrates without the sacrificial layers. In other words, what is the compromise here in terms of defect density and other material properties?

2. For the integrated GaAs and GaN detectors, these thin-films were bonded to SiN for demonstration purposes only whereas they were placed/compressed on top of a metallic film (i.e. Au) for the actual devices where this metal served as the back contact. This invalidates the ‘van der Waals integration’ claim for the photodetectors. As I understand, top-side contacts are feasible for these HI devices without the air-gap. Would the lack of an air-gap improve the coupling performance or overall responsivity of these detectors?

3. Regarding the IV of the detectors, especially the GaAs, the dark is quite high at ~1uA. While the zoomed-in TEMs look impeccable, this leaves the reader wondering if there are quite a few crystal defects outside of the zoomed-in TEM. Is the high dark current the result of higher defect density? Moreover, the responsivities of both detectors are lower than expected for these materials especially the 16.6mA/W at 405nm. Is there an explanation for this?

4. There is a demonstration of MO CFO optical isolator. Was there also an MO isolator using YIG as it is mentioned including the growth of thin-film YIG?

5. CFO is mentioned as being magnetizable with a few hour demonstration. How does this approach compare with using harder thin-film magnets such as FeCoB in conjunction with softer magnetic materials such as YIG or Ce:YIG? In principle, the latter approach can hold state for much longer durations (years or decades).

6. Why is the co-integration of EO BTO material and MO CFO materials into a single ring-resonator device relevant or important? The authors make it clear that the EO modulation device is functioning only for the TE mode while the MO isolation device is working for only the TM mode. While intriguing, one would need to have both TE and TM modes in this

device whereas most applications typically have one or the other. Does this introduce un-necessary material losses especially from evanescent mode coupling to CFO thin-film atop the BTO film? The losses for CFO are listed in Figure 5c.

Minor comments:

1. Please define acronyms in the main manuscript, not just in figure captions (i.e. PDMS, TRT, etc)

2. Placement of figure 1f is a bit confusing (perhaps have this also read horizontally like the other sub figures)

3. For Figure 3 caption for photodetectors, please state the wavelength of operation and responsivity values in the caption text (easily missed in the figure insets).

4. Figure 5a is not referenced in the manuscript. Also Figure 4g-k are mis-labeled in the text on page 10 as Figures 5g-k.

5. At the end of section 4, please specify which material (GaAs or GaN) was used for each wavelength. The assumption is GaN at 520nm wavelength and the IV data is not shown for this.

Overall, this paper is an amalgamation of different thin-film materials being integrated onto Si and SiN photonic circuits. All of these materials have been integrated onto Si and SiN in other works with far better performance on the individual devices than reported here in this paper. The true novelty is perhaps in the material science aspect of remote epitaxy. The sheer volume of work reported here is impressive and perhaps too much for a single journal paper and could be split into 4 or 5 individual papers. With all that said, this paper is not a good fit for Nature. Perhaps it is a better fit for Nature Materials.

Referee #4

(Remarks to the Author)
I co-reviewed this manuscript with one of the reviewers who provided the listed reports.

Version 1:

Reviewer comments:

Referee #1

(Remarks to the Author)
I appreciate the additional explanations and experimental data by the authors and have no further comments.

Referee #2

(Remarks to the Author)
I co-reviewed this manuscript with one of the reviewers who provided the listed reports.

Referee #3

(Remarks to the Author)
We would like to thank the authors for the extensive effort they have taken to address the concerns of the reviewers. We acknowledge the impressive work and effort that went into this manuscript and the response, however, we still feel that the work feels dis-jointed, attempting to cover too much material for one article. We don't feel it is appropriate for Nature in it's current form.

Referee #4

(Remarks to the Author)
I co-reviewed this manuscript with one of the reviewers who provided the listed reports.

Responses Letter to Reviewers

We would like to first sincerely thank all the reviewers for their careful assessment of our manuscript with the constructive and positive comments. We have carefully revised our manuscript and Supplementary Information, accordingly. Additional experiments and simulations are supplemented to further validate related discussions. The novelty and further impact of this work are also carefully benchmarked and highlighted in revised manuscript. Detailed responses and revisions are as follows.

Table of Contents

Responses to Referee 1: 3
- Comment: 3
- Response: 3
- Comment: 3
- Response: 3
- Comment 1: 16
- Response 1: 16
- Comment 2: 17
- Response 2: 17
- Comment 3: 22
- Response 3: 22
- Comment 4: 23
- Response 4: 24
- Comment 5: 29
- Response 5: 29
- Comment 6: 32
- Response 6: 32
- Comment 7: 33
- Response 7: 34

Responses to Referee 2: 35
- Comment: 35
- Response: 35

References for Reviewer 1 and Reviewer 2: 35

Responses to Referee 3: 37
- Comment: 37

Response: 37
Comment 1: 37
Response 1: 37
Comment 2: 44
Response 2: 44
Comment 3: 48
Response 3: 48
Comment 4: 52
Response 4: 52
Comment 5: 53
Response 5: 53
Comment 6: 56
Response 6: 56
Comment 7.1: 59
Response 7.1: 59
Comment 7.2: 60
Response 7.2: 60
Comment 7.3: 61
Response 7.3: 61
Comment 7.4: 61
Response 7.4: 61
Comment 7.5 61
Response 7.5: 62
Comment 8: 62
Response 8: 62
Responses to Referee 4: 73
Comment: 73
Response: 73
References for Reviewer 3 and Reviewer 4: 73

Responses to Referee 1:

Comment:

The manuscript presents an ambitious and compelling vision of "photonic Lego" based on van der Waals (vdW) integration of diverse functional nanomembranes. The concept of vdW integration was originally developed for atomically thin or quasi–atomically thin material systems, where interlayer interactions are dominantly governed by vdW forces. In this work, however, functional membranes, such as BTO, CFO, and GaAs with thicknesses ranging from several tens to over one hundred nanometers, were transferred to silicon photonics platform, enabling functionalities like EO modulation, non-reciprocity, and photodetection that are otherwise not accessible in native silicon. The authors performed a very comprehensive investigation that starts from material synthesis and characterization, to heterogeneous vdW integration, device fabrication, and functional testing, on a variety of material systems. Results suggest that the transferred materials have largely maintained their good native crystalline properties. The measured device performances, although not record-breaking, are also compelling especially compared with other previous heterogeneous integration methods.

Response:

We sincerely thank the reviewer for the careful assessment and positive remarks. We are grateful for the detailed and constructive comments that greatly helped us to further improve and clarify our manuscript. Below are the detailed responses with corresponding revisions made to the manuscript.

Comment:

My main concern is regarding the most critical innovation in the paper, which I hope the authors could more clearly discuss. The concept of vdW integration has been hot in recent years due to its powerfulness in 2D material engineering, but I would argue that almost any heterogeneous integration approaches that already exist in the integrated photonics community are based on vdW interactions too, e.g. existing wafer or die bonding techniques between III-V, LN/LT and Si/SiO2. In my understanding, the main difference between the current and these past works lies in the way that the thin films were exfoliated, e.g. via 2DLT and ELO methods. Between these two methods, 2DLT is a recently emerging and interesting one, while ELO based on wet etching of sacrificial layer seems to have been adopted in III-V thin-film preparation for quite some time. However, if I understand correctly most of the actual devices demonstrated in this work were prepared using the more traditional ELO method.

Apart from vdW and thin-film preparation, the achieved device performances are not exotic; the prospect for multi-layer stacking is interesting, but it is unclear what application would require such stacks. To summarize, I believe the achieved material properties in the final devices in this paper are good, and the method is general and proven applicable to a variety of materials, but it is unclear what is the key innovation here that has enabled these.

Response:

We thank the reviewer for raising this constructive concern. This suggestion is taken fully.

The key innovations of this work against prior literature lay in the synthesis and transfer engineering of diverse functional 3D nanomembranes with single-crystalline material quality and artificially delaminated freestanding form for unbounded vdW integration, and their device implementation in realizing high-performance heterogeneous integrated photonic devices. Specifically, it can be categorized as follows:

(1) **For single-crystal nanomembranes preparation**, the innovations include both fundamental thin-film growth engineering and layer exfoliation for van der Waals (vdW) integration.

The optimal single-crystalline quality of these freestanding thin films with well-defined crystallographic orientations are the keys to enable the record-setting thin-film material properties reported in this work, which are vital for various photonic and optoelectronic applications, such as the Pockels coefficient for electro-optical (EO) applications, Faraday rotation coefficient for magneto-optical (MO) applications, and photoresponsivity for broad optoelectronic applications.

(1.1) For example of thin-films growth, the ability to precisely control the crystalline quality and crystallographic orientations is crucial for the Pockels response of EO material barium titanate (BTO), leading to significant distinctions on material and device performances.

Tremendous and varying endeavors have been devoted so far to developing BTO-based photonic devices, targeting to harness its giant Pockels coefficient (about 40 times higher than lithium niobate (LN) and lithium tantalate (LT) for bulk BTO crystals) for ultraefficient integrated EO applications. However, dramatic variations exist in the reported BTO effective Pockels coefficient r_{eff}, ranging from merely 22 pm/V (Ref.[1]) to over 600 pm/V (Refs.[2,3]). A brief benchmark of this work against prior publications is summarized below as Table R1-1 (detailed discussions are made in Supplementary Note S12 and Table S1 in the revised Supplementary Information).

Table R1-1. Brief benchmarks of this work with prior references using BTO or other EO materials

EO Material	**Hybrid waveguide?**	**$r_{\text{eff}}^{\parallel}$ (pm/V)**	**Largest r_{ij} (pm/V)**	**Notes on material preparations**	**Reference**
BTO	Yes (Si–BTO)	680*	923	MBE BTO on Si with STO buffer. Wafer bonding & substrate grinding applied.	Nature Materials 18, 42–47 (2019)
BTO	Yes (Si–BTO)	213	—	MBE BTO on SOI with engineered STO buffer layer. Top Si hybrid slab WG.	Nano Lett. 14 (3), 1419–1425 (2014).
		—	—		
BTO	Yes (Si–BTO)	48	—	Transferred freestanding *c*-axis-domain BTO.	Light: Adv. Manufact. 5, 31 (2024)
BTO	Yes (Si–BTO & SiN-BTO)	200	—	MBE BTO on Si with engineered STO buffer.	Nature Materials 19, 1164-1168 (2020)
BTO	Yes (SiN–BTO)	624*	> 1000⍰	BTO growth with engineered STO buffer.	Nature 641, 876-883 (2025)
BTO	N/A	388*	<500*	RF sputtered BTO on SiO_2 with buffer.	Nature Materials 24, 868-875 (2025).
BTO	N/A	121	—	BTO epitaxy on STO with $BaSnO_3$ buffer.	Phys. Rev. Mater. 5, 035201 (2021).
BTO	No (BTO WG)	—	358	PLD BTO. Material study only - no devices.	Light: Sci. & Applications 15, 21 (2026)
BTO	No (BTO WG)	22	—	Poly-crystal BTO grown on glass.	Optics Lett. 28 (24), 2527-2529 (2003)
BTO	No (BTO WG)	162	—	RF sputtered BTO with STO buffer layer.	arXiv:2507.17150 (2025)
BTO	No (BTO WG)	300*	—	MBE BTO on Si with engineered STO buffer.	J. Lightwave Technol. 34, 1688 (2016).
BTO	No (BTO WG)	89	—	RF sputter BTO on SOI.	ACS Photonics 10, 4367-4376 (2023).
BTO	Yes (Si–BTO)	950*	1290	vdW integration of freestanding single-crystalline *a*-axis-domain BTO thin-film.	This work
		880*	1190		
LN	Yes (SiN–LN)	—	30.9	Wafer bonding LNOI with SiNOI.	Nature Communications 14, 3499 (2023)
LN	Yes (SiN–LN)	—	30.9	Wafer bonding LNOI with SiNOI.	Optica 10 (5), 578-584 (2023)
LT	Yes (SiN–LT)	—	30*	Wafer bonding LTOI with SiNOI.	Nature 629, 784–790 (2024)
LT	Yes (SiN–LT)	—	30*	Wafer bonding LTOI with SiNOI.	Nature Communications 17, 3314 (2026)

Notes: WG: waveguide. Only in-plane (film-parallel) effective Pockels coefficients $r_{\text{eff}}^{\parallel}$ are marked by default. Pockels tensor components that are perpendicular to film plane and ineffective to on-chip EO applications are marked out with ⍰ superscript. N/A denotes material study only. Detailed explanations are made in Table S1 of the Supplementary Information.

The core reason for these drastic variations manifested in Table R1-1 lies in the BTO crystal quality and its crystallographic orientation.

Firstly, for BTO grown with poor crystal quality (such sputtered BTO in many lattice-mismatched substrates shown in Table R1-1 above), its EO response is largely deteriorated compared to bulk crystal. For poor polycrystalline BTO, its effective Pockels coefficient can be even lower than LN or even negligible for amorphous BTO (Ref: Nature Communications 4, 1671, 2013).

Secondly, even for single-crystalline BTO, its crystallographic orientation still plays a crucial role in affecting the overall EO performance. As the EO Pockels effect is excessively dependent on the construction of the 3-order Pockels tensor $\mathbf{r}_{\mathrm{BTO}}$ and the vectorial orientations of the light polarization, radio frequency (RF) electric field $\mathbf{E}_{\mathrm{RF}} = [E_x^{\mathrm{RF}}, E_y^{\mathrm{RF}}, E_z^{\mathrm{RF}}]^T$, and the crystallographic orientation of the BTO c-axis[4],

$$\Delta\boldsymbol{\eta}_{\mathrm{BTO}} = \begin{bmatrix} \Delta(1/n^2)_1 \\ \Delta(1/n^2)_2 \\ \Delta(1/n^2)_3 \\ \Delta(1/n^2)_4 \\ \Delta(1/n^2)_5 \\ \Delta(1/n^2)_6 \end{bmatrix} = \mathbf{r}_{\mathrm{EO}} \cdot \mathbf{E}_{\mathrm{RF}} = \begin{bmatrix} 0 & 0 & r_{13} \\ 0 & 0 & r_{13} \\ 0 & 0 & r_{33} \\ 0 & r_{42} & 0 \\ r_{42} & 0 & 0 \\ 0 & 0 & 0 \end{bmatrix} \begin{bmatrix} E_x^{\mathrm{RF}} \\ E_y^{\mathrm{RF}} \\ E_z^{\mathrm{RF}} \end{bmatrix}$$

where $\Delta\boldsymbol{\eta}_{\mathrm{BTO}}$ is the impermeability tensor describing the refractive index change of BTO under the EO modulation of applied electric field $\mathbf{E}_{\mathrm{RF}}$, and the specific equation of $\mathbf{r}_{\mathrm{BTO}}$ relies on device design and the judicious arrangement of BTO crystal c-axis (detailed in Supplementary Note S7, and Fig. S14). For BTO bulk crystal, its Pockels tensor components have very big distinctions in numerical values: r_{13}~20 pm/V, r_{33}~100 pm/V, r_{42}~1600 pm/V (Ref: R. W. Boyd, Nonlinear Optics, 511-523 Springer, 2008. Ref: Nature Materials 19, 1164-1168, 2020). Consequently, if the crystallographic orientation of BTO is not judiciously controlled, other Pockels components are probed instead of the biggest tensor component r_{42}, which will lead to dramatically decreased EO response — almost 100 times variation in the measured effective Pockels coefficient r_{eff}.

• Despite that efforts on controlling the crystallinity and crystallographic orientations of BTO were also made in previous works (e.g. Ref: Nature Materials, 18, 42–47, 2019; Ref: Nature, 641, 876-883, 2025; Ref: Nature Materials 24, 868-875, 2025), they majorly rely on the direct heteroepitaxy of BTO on optical substrates such as Si with disparately mismatched crystal structures. Although thin strontium titanate ($SrTiO_3$, STO) buffer layers were applied, the quality of the resultant BTO epilayers are still limited by the fundamental epitaxial lattice-matching constraints.

In contrast, we have thoroughly addressed this critical hurdle (i.e. compromised BTO Pockels response shown in Table R1-1) of BTO-based EO applications in this work, by utilizing a fundamentally distinctive strategy: creating freestanding single-crystalline BTO nanomembranes with engineered crystal orientations, in optimal lattice-matched parent substrates and then get transferred to photonic templates for heterogeneous photonic integration, instead of direct heteroepitaxy used most prior references. As a result, we have experimentally demonstrated record-setting BTO *in-plane* effective Pockels coefficient r_{eff} about 950 pm/V, corresponding to a giant EO Pockels tensor component r_{42} of 1290 pm/V, which are the highest values reported so far in integrated photonics to the best of our knowledge.

• We note that in some literature, *out-of-plane* Pockels coefficients of BTO were measured and reported (e.g. Ref: Nano Letters, 25, 11089-11096, 2025, and Ref: Nature, 641, 876-883, 2025), where free-space light was injected perpendicular to the BTO films in experimental setups. However, these reported r_{eff}[?], contributed by c-axis-domain (i.e. (001) crystal plane orientation) BTO, are ineffective to be leveraged in integrated photonics, as light signals are all propagating along the waveguides parallel to the photonic chip plane, instead of perpendicular to the chip plane set in the free-space-based BTO EO property measurements.

Therefore, the tensor nature of the Pockels effect determined that only *in-plane* Pockels coefficient $r_{\mathrm{eff}}^{\parallel}$ can effectively contribute to EO applications in PICs, which requires engineered a-axis-domain (i.e. (100) or (010) crystal plane orientations) BTO demonstrated in this work. Detailed discussions are made in the last paragraph of Supplementary Note S12 below Table S1 in the Supplementary Information.

• Indeed, epitaxial lift-off (ELO) was previously proposed to create III-V nanomembranes. However, comparatively fewer attentions were devoted to synthetizing freestanding functional complex oxide films for integrated photonics, with judiciously selected sacrificial layer that simultaneously promote the crystal quality and the lift-off the desired epilayer (e.g. Ref: Science 383, 388-394, 2024). Specifically, the ELO method for BTO via $Sr_3Al_2O_6$ (SAO) sacrificial layer was indeed explored in Ref: Science, 384, 312-317, 2024 (as our prior work), and Ref: Light: Advanced Manufacturing 5 (31), 479-489 (2025). However, for the former Science paper (Ref.[5]), only the ferroelectric polarization of BTO was studied for pure electronic and energy applications (not related to photonics). For the later paper (Ref.[6]), a low BTO experimental effective Pockels coefficient r_{eff} of only 48 pm/V was realized, with a $V_\pi \cdot L$ of 1.67 V·cm measured at DC voltages. The critical factors of BTO crystal axis orientation engineering were not explored in this reference, which actually leads to drastic variations on BTO EO response. In contrast, in this work, we have experimentally realized a giant BTO r_{eff} of 950 pm/V (about 20-fold improvement), with a low $V_\pi \cdot L$ of 0.29 V·cm measured at low frequencies. This is made possible by systematic engineering on both BTO crystallinity and crystallographic orientations through the synergistic control over the BTO film epitaxy, annealing, and cooling processes beyond ELO method (detailed discussions made in Supplementary Note S4), serving as a very helpful guidance for future research on BTO-based EO applications.

(1.2) Besides EO material BTO, systematic studies are made on an ultraefficient magneto-optical (MO) material cobalt ferrite (CFO), which attracts comparatively fewer attentions before than garnets.

• A giant Faraday rotation coefficient θ_{F} of 33,800 °/cm is experimentally demonstrated, which is about 100 times higher than current mainstream MO material YIG, and 8~10 times higher than Ce: YIG (Ref: Nature Electronics 5, 604–610, 2022; Ref: Nature Photonics 5, 758-762, 2011; and Ref: Nature Photonics 19, 54-62, 2025), setting a positive reference for developing future ultracompact and high-efficiency non-reciprocal optical applications.

• This remains the first demonstration of single-crystalline CFO thin-film based non-reciprocal integrated photonic devices via layer transfer to the best of our knowledge.

Compared with previous approaches relying on direct heteroepitaxy of CFO on Si, we have vastly promoted the crystal quality of the functional CFO films with largely enhanced material and device performances. A detailed benchmark of the CFO film in this work against prior publications is made in Supplementary Note S24 and Table S3 in Supplementary Information.

• Compared with MO devices based on YIG and Ce: YIG, which are soft magnetic materials, the large coercive field of CFO (as a hard ferromagnet) enables on-chip non-reciprocal transmission without external magnets after proper magnetization, which is not possible by using other garnets-based photonic devices.

(1.3) The synthesis of other high-quality nanomembranes such as group III-V semiconductors GaAs and GaN, and MO material YIG are also technically advanced.

• Exploiting both remote epitaxy with 2D-materials-based layer transfer (2DLT, Ref: Nature 614, 81-87, 2023. Ref: Nature Reviews Methods Primers 2, 40, 2022) we further promote the crystal quality with strengthened defects reduction for freestanding GaAs and GaN nanomembranes[7,8], enabling cost-saving substrate recycling and fast layer-release speed (detailed in Supplementary Note S16).

• Further optimization and benchmarks of freestanding yttrium iron garnet (YIG) nanomembranes using 2DLT and ELO with technical details important for thin-film synthesis and device applications (discussed in Supplementary Note S5).

(2) **For freestanding functional optical layer transfer**, this work establishes a comprehensive framework for freestanding nanomembranes-based photonic heterogeneous integration platform with experimentally verified feasibility and unique strengths.

(2.1) We agree with the reviewer that most of current heterogeneous integration schemes are indeed based on van der Waals (vdW) interactions. However, in prior research on hetero-integrated photonics, the critical role of creating and integration with freestanding single-crystalline nanomembrane as building blocks was not fully acknowledged or explicitly manifested.

• For example, in current wafer bonding processes for LN and LT, the exact form of freestanding nanomembranes actually were not emphasized: the top LN or LT layers are directly bound to oxide substrates after ion implantation, and followed by lengthy bulk substrate removal with chemical mechanical polishings (no freestanding films). This is actually a very sophisticated procedure requiring extensive stringent process engineering, with inevitable crystal ion damage. If the target substrate is changed, for instance, to Si, silicon nitride, or other photonic platforms with different material surface characteristics, or changed to certain prefabricated photonic templates, big and lengthy modifications and re-optimizations will be necessitated for current LN and LT bonding processes to ensure successful layer bonding.

Taking another example of current BTO hetero-integration (layer bonding also used), crystalline BTO is first deposited on attentively engineered STO buffer layer grown and annealed by molecular beam epitaxy (MBE) on Si, followed by oxides (such as Al_2O_3) mediated BTO layer bonding and complex substrate grinding, etching, and polishing processes (Ref: Nature Materials 18, 42–47, 2019; Ref: Nature Materials 19, 1164-1168, 2020) before a device can be made.

In contrast, in this work our freestanding nanomembranes-based vdW integration strategy is a universal method applicable to arbitrary desired functional optical materials and arbitrary optical substrates, in a fast, cost-saving (detailed in Supplementary Note S27), convenient-to-implement, and with approaching atomic-level precision on the resultant integrated optical layer thickness. It does not require the complex ion implantation slicing or the time-consuming substrate grinding and polishing procedures indispensable in the abovementioned approaches to get the functional optical layer transferred. Our proposed freestanding nanomembrane-based vdW integration method thus exhibits great versatility and ultrahigh degrees of freedom in unlocking novel photonic heterogeneous integration structures and new multifunctional applications.

• For III-V nanomembranes, compared to semi-device level die-bonding and micro-transfers, the freestanding thin-films based integration enables wide applications from device to system level. The 2DLT III-V thin films in this work feature high-throughput multi-layer production of freestanding single-crystal nanomembranes (Ref: Nature Nanotechnology 18, 464-470, 2023), buffer-free precise layer separation (Ref: Nature 641, 98-105, 2025), and efficient film defects reduction (discussed in Supplementary Note S16).

(2.2) Current established photonic heterogeneous approaches can be mainly categorized into two directions: (i) Direct heteroepitaxy of the desired functional optical materials, and (ii) wafer bonding of target photonic layers. The formal approach suffers from typically poor epilayer crystal quality with deteriorated material performance, while the later approach (primarily researched in group III-V semiconductors) lacks general method versatility and is constrained by the complex substrates removal and polishing procedures.

• Here in this work, we explicitly demonstrated and verified the critical benefits of using single-crystalline freestanding nanomembranes. Both the single-crystalline film quality and its freestanding form with artificially laminated vdW interfaces are the keys for enabling boundless and high-performance photonic heterogeneous integrations reported in this work.

The formation and integration of freestanding 3D nanomembranes were not virtually standing, or were not clearly elucidated with careful attention, in prior direct growth-based or wafer-bonding-based photonic hetero-integration studies. This vdW integration concept so far is still largely restricted to 2D materials research communities, as the creation and handling of 3D freestanding nanomembranes with high crystallinity and well-preserved optical functionality to their bulk counterparts is still in its early stages of study.

• This work can thus establish a comprehensive baseline for the vdW integration of 3D freestanding films, covering freestanding nanomembranes synthesis, lift-off, integration, device design, and implementation, to embody a promising alternative pathway towards photonic heterogeneous integration (besides the two established common approaches discussed above), for enabling exotic hybrid and hetero-integration layouts and prototyping record-setting high-performance photonic applications. Previously inaccessible heterogeneously integrated device structures can now be made possible by this vdW integration of 3D freestanding thin-films with the highest available material quality.

Besides, this method also does not require lengthy and expensive layer integration facilities, showing great values and conveniences with further impacts for both small-scale lab research and large-scale foundry-based heterogeneous integration after adopting autonomous layer transfer tools in future, with faster integration process, lower cost, and much higher versatility than wafer bonding. These are the above reasons that we emphasize the freestanding nanomembranes and the vdW integration concepts here in this work.

(3) **For device implementations and performances evaluation**, this work remains the first systematic demonstration on the vdW integration of multiple functional freestanding 3D single-crystals for hetero-integrated photonics, to the best of our knowledge, with experimentally verified superior, or comparable performance to state-of-the-art devices of similar configurations.

We would like to make the following justifications on the advancement of the achieved device performances, where we believe a unified comparison criterion can make a more reasonable and clearer benchmarks between devices under same configuration. This is because different device structures highly affect the performance parameters including driving voltages, optical loss, and device EO bandwidth etc. with varying pros and cons and their unique advantages.

(3.1) **For BTO-based device performances**, majority of prior research only conducted DC or low-frequency measurements (briefly summarized as Table R1-2 below). Our experimental device half-wave voltage-length product $V_\pi \cdot L$ of 0.29 V·cm (measured at 1 kHz frequency, under device Design B shown in main text Fig. 2h), which is among the lowest in most previous publications with $V_\pi \cdot L$ ranging from 0.3 ~ 1.67 V·cm if compared with other hybrid EO waveguides (i.e. EO materials coupled with Si or silicon nitride (SiN) waveguides).

Table R1-2. Brief benchmarks the BTO-based EO device performances of this work against prior publications

EO Material	Hybrid waveguide	Structure	$r_{eff}^{\parallel}$ (pm/V)	$V_\pi \cdot L$ (V·cm)	EO 3dB BW (GHz)	Ref
BTO	Yes (Si–BTO)	Microring	680*	—	30	Nature Materials 18, 42-47 (2019)

BTO	Yes (Si–BTO)	MZI	213	1.5	0.8	Nano Letters 14, 1419-1425 (2014)
		Microring	—	—	4.9	
BTO	Yes (Si–BTO)	Microring	380	—	12*	J. Lightw. Technol. 37, 1456-1462 (2019)
BTO	Yes (Si–BTO)	MZI	48	1.67	—	Light: Adv. Manufact. 5, 479-489 (2025)
BTO	Yes (Si–BTO & SiN-BTO)	Microring MZI	200	— (Ring) 5 (MZI)	~30* (ring) ~20* (MZI)	Nature Materials 19, 1164-1168 (2020)
BTO	Yes (SiN–BTO)	Microring	343	0.3	DC/NA	ACS Photonics 6, 2677-2684 (2019)
BTO	Yes (SiN–BTO)	MZI	360	0.5	DC/NA	J. Opt. Soc. Am. B 22, 240-253 (2005)
BTO	Yes (SiN–BTO)	MZI	38	4.5	DC/NA	IEEE PTL. 16, 1837-1839 (2004)
BTO	Yes (SiN–BTO)	MZI	624*	0.62	6.9	Nature 641, 876-883 (2025)
BTO	No (BTO WG)	MZI	22	5.7	—	Opt. Lett. 28, 2527-2529 (2003)
BTO	No (BTO WG)	MZI	162	0.54	—	arXiv:2507.17150 (2025)
BTO	No (BTO WG)	MZI	150	1.248	3.7	Opt. Express 12, 5962-5967 (2004)
BTO	No (BTO WG)	MZI	89	2.32	> 5.9*	ACS Photonics 10, 4367-4376 (2023)
BTO This work	Yes (Si–BTO)	MZI	950*	0.29	DC/NA	This work
			880*	1.4	> 23	
LN	Yes (SiN–LN)	MZI	~30*	8.2~8.8	—	Nature Communications 14, 4856 (2023)
LN	No (LN WG)	MZI	~30*	3.67	22	Optics Express 29, 17710–17717 (2021).
LT	Yes (SiN–LT)	MZI	~30*	4.08	> 70*	Nature Communications 17, 3314 (2026)
LT	Yes (SiN–LT)	MZI	~30*	3.5	70*	Nature Photonics 20, 225–231 (2026)

Notes: Superscript * denotes calibration or calculated estimations applied. Entry — represents not reported or studied in the reference. DC/NA denotes only DC or low-frequency characterizations were reported. MZI: Mach-Zehnder interferometer. WG: waveguide. LN: lithium niobate. LT: lithium tantalate. Detailed explanations are made in Table S1 of the Supplementary Information in Supplementary Note S12.

• We selected a balanced $V_\pi \cdot L$ and device EO 3 dB bandwidth for the high-speed EO Mach-Zehnder modulator (MZM) shown in main text Fig. 2k, under a device structure namely Design A (illustrated as Fig. R1-1a below). The experimentally measured device $V_\pi \cdot L$ and EO 3 dB bandwidth for this BTO MZM are 1.4 V·cm and 23 GHz respectively.

(i) In the design, we sacrificed $V_\pi \cdot L$, by using a thinner BTO film and introducing a thick SiO_2 buffer layer between the electrodes and BTO layer (in order to reduce device microwave impedance Z_0 and for better velocity matching of travelling wave electrodes), to trade for higher device EO bandwidth. Detailed reasons and design trade-offs considerations are discussed in the revised Supplementary Note S10 in the Supplementary Information (Page 18).

(ii) The achieved 23 GHz EO 3 dB bandwidth is also among the highest or comparable to previous MZM-structure-based modulators (as Table R1-2 above). The majority of prior BTO-based MZMs show quite low EO bandwidth, due to the mismatched Z_0 and group velocities in modulation (detailed in Supplementary Note S10).

For example, for hybrid waveguide-structured devices, in Ref: Nature 641, 876-883 (2025), and Ref: Nano Letters 14, 1419-1425 (2014), the reported BTO MZM 3 dB EO bandwidths are only 6.9 GHz and 4.9 GHz respectively. For devices with directly EO material (BTO)-as-waveguide structures, such as Ref: ACS Photonics 10, 4367-4376 (2023), the 3 dB EO bandwidth is over 5.9 GHz. Our experimental 23 GHz 3 dB EO bandwidth remains much higher than those prior similar works.

Besides, current 23 GHz EO 3 dB bandwidth in this work is also limited by the device fabrication and non-ideal electrodes formation (discussed in Supplementary Notes S15) with future room of improvement. For some micro-ring-based EO modulator devices, higher EO bandwidths were indeed reported (Table R1-2). However, those devices have intrinsically, and significantly narrower spectral operation range compared to the EO MZMs demonstrated in this work, with high sensitivity to temperature variations as well, limited by their fundamental tuning nature on the optical resonance change of the micro-rings. Mach-Zehnder modulators (MZMs) are still the current mainstream solutions for EO modulation applications.

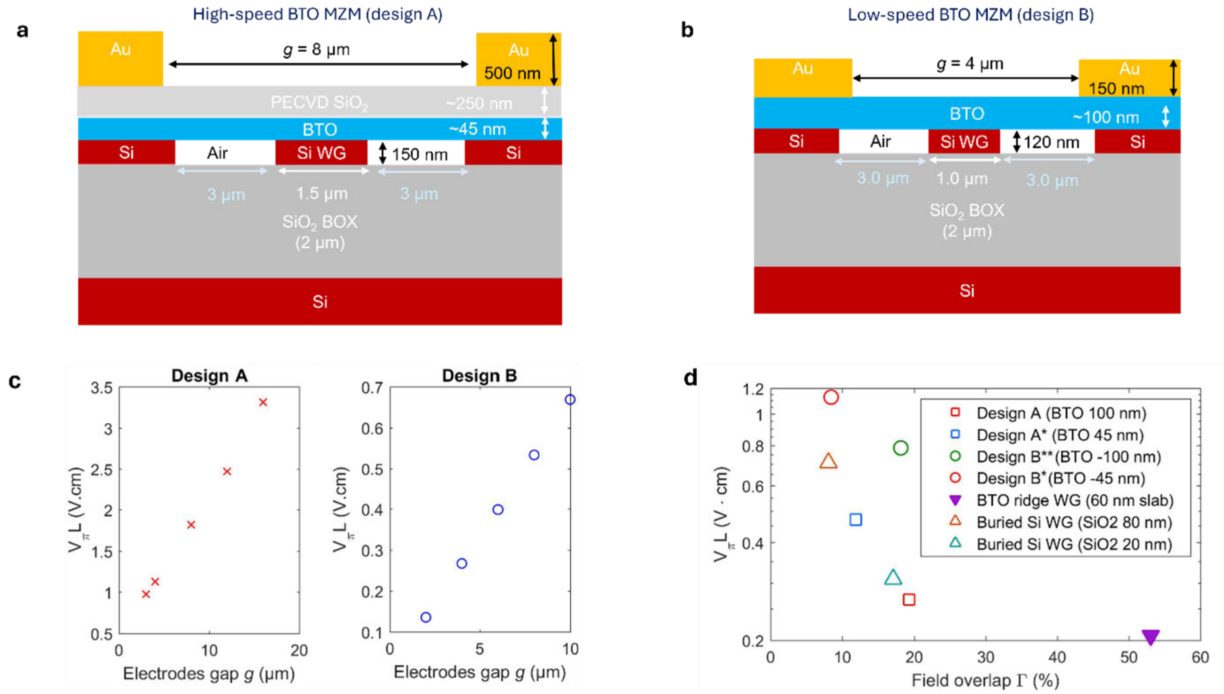

Fig. R1-1. Device structure and design trade-offs summary. (a) Device structure schematics (namely design A) corresponding to the high-speed BTO MZM shown in Fig. 2k in manuscript main text. (b) Device structure schematics (namely design B) for the low-speed BTO MZM shown in Fig. 2h in main text. (c) Device half-wave voltage-length product $V_\pi \cdot L$ as a function of electrodes gap distance g of different device structures. (d) Scatter plot of $V_\pi \cdot L$ and optical field overlap factor Γ (i.e. the portion of optical power inside BTO EO layer) under different device structures (details are made in Response 2 at Page 18 of this response letter).

(iii) Despite that we sacrificed $V_\pi \cdot L$ for enhanced device EO bandwidth, the achieved 1.4 V·cm $V_\pi \cdot L$ for the MZM (under device structure A illustrated below in Fig. R1-1) is still comparable to or better than many previous publications based on BTO (Table R1-2). For example, in Ref: Nature Materials 19, 1164-1168 (2020), the reported $V_\pi \cdot L$ is over 5 V·cm for the BTO MZM (with a big driving voltage ~ 50 V), which is much higher than this work.

Specifically, this value exhibits clearer advantages when compared to prior works using LN- or LT-based hybrid-waveguide MZMs. For example, for previous LN hetero-integrated SiN waveguides, the resultant EO MZM reports a $V_\pi \cdot L$ over 8.2 V·cm in Ref: Nature Communications 14, 4856 (2023), which is about 6 times higher than our work. For the very recent papers utilizing transferred LT films, the reported $V_\pi \cdot L$ are about 4.08 V·cm for Ref[9]: Nature Communications 17, 3314 (2026) (our collaborator's work using wafer bonding), and 3.5 V·cm for Ref[10]: Nature Photonics 20, 225–231 (2026) (micro-transfer of LN films etched and lifted off from LNOI wafers).

• The driving voltage or $V_\pi \cdot L$ is also highly dependent on the portion of the optical power inside the EO material (i.e. the optical field overlap factor Γ) to facilitate EO modulation, and distance between the electrodes g.

If targeting for smaller modulation voltage solely, we have conducted supplementary simulations showing that the $V_\pi \cdot L$ of our current BTO MZM devices can be further reduced to 0.13 V·cm and 0.97 V·cm for MZM structures of Design B and Design A respectively, by altering the electrodes gap distance g to 2 μm and 3 μm respectively, at the cost of drastically reduced 3 dB EO bandwidth and increased optical loss. These results are briefly summarized as Fig. R1-1a and R1-1b above. Detailed discussions are made in Response 2 on Page 18 of this Response Letter.

Actions taken:

We have added additional simulation results and discussions on the design considerations and justifications on device performance on Supplementary Notes S10 and S12.
Revisions on Supplementary Note S10 (highlighted in yellow, on Page 21 of Supplementary Information).

> robustness of current Si and SiN photonic technologies[60,77,78]. If compared to prior hybrid-waveguides-based EO MZMs using LT or LN[77,78], our experimental $V_\pi \cdot L$ values for BTO-MZMs are about 3~6 times (for 'design A') and 12~28 times (for 'design B') lower. Compared to previous publications directly using patterned BTO material as waveguides[79,80], despite their intrinsically higher optical field overlap factor Γ than hybrid EO waveguide configurations, this work still shows better EO modulator $V_\pi \cdot L$, thanks to the significantly higher BTO Pockels coefficients by fundamentally circumventing the lattice mismatch limit in direct BTO heteroepitaxy from those prior works (Supplementary Note S12). If solely pursuing for lower driving voltage, the $V_\pi \cdot L$ for the BTO MZMs in this work can be further reduced below 0.2 V·cm, by altering the electrodes gap distance g at the cost of increased loss and deteriorated device EO bandwidth (Figs. S19g and S19h).

(3.2) **For CFO-based non-reciprocal device performance**, we have achieved high non-reciprocal phase shift (NRPS) 4.68 rad/mm within an ultrashort magneto-optical (MO) waveguide length L_{MO} of only 0.026 mm (shown as main text Fig. 4c). The achieved NRPS is about 3 ~ 9 times higher than previous works using Ce: YIG (e.g. Ref: Nature Electronics, 5, 604-610, 2022; Ref: Nature Photonics, 5, 758-762, 2011; Ref: Optica, 6, 473-478, 2019), while the effective interaction device length L_{MO} is about 9 ~ 70 times shorter than previous works (Ref: Nature Photonics, 19, 54–62, 2025), which is made possible by the record-high experimental CFO Faraday rotation coefficient θ_F.

If further compared to previous publications using CFO (based on direct RF sputtering of CFO on lattice-mismatched Si surface despite buffer layer applied), our experimental device parameters including NRPS and L_{MO} are also show better performance. The 18.9 dB isolation ratio of this work is also higher than previous works based on CFO: e.g. 9.6 dB in Ref: IEICE Electronics Express 19, 20210500 (2022); and 5.5 dB in Ref: Applied Physics Express 8, 082201 (2015).

Further, the CFO-hetero-integrated Si microring isolators in this work have much reduced optical loss thanks to the optimal single-crystallinity of our vdW-integrated CFO films with significantly suppressed scattering loss from CFO film defects (as compared in Fig. R1-2 below). Detailed discussions are made in Supplementary Note S24.

Table R1-3. Brief performance benchmarks of non-reciprocal devices in this work (CFO) to prior publications

MO Material	θ_F (°/cm)	α_m (dB/cm)	NRPS (mm^{-1})	L_{MO} (mm)	Notes on material preparations	Ref
Ce:YIG	-1500	—	1.9*	0.85*	Sputtered Ce: YIG on Si with YIG buffer.	Optica 6, 473-478 (2019)
Ce:YIG	-3000	—	0.55*	5.6*	Wafer bonding of Ce:YIG to SOI ring.	Opt. Exp. 19, 11740-11745 (2011)
Ce:YIG	-3200	60*	0.79*	2*	Wafer bonding of Ce:YIG film to SOI.	Appl. Phys. Lett. 92, 071117 (2008)

Ce:YIG	−5900	137*	1.57*	1*	PLD Ce:YIG on SiN with YIG buffer layer.	Optica 7, 1555-1562 (2020)
Ce:YIG	-4000	—	0.98*	0.92*	Wafer bonding of Ce: YIG dies.	Opt. Exp. 20, 1839-1848 (2012)
Ce:YIG	−1263	—	0.63*	0.2*	PLD poly-crystal Ce: YIG on Si.	Nature Photon. 5, 758-762 (2011).
Ce:YIG	-3500	—	0.5*	0.22*	Wafer bonding of Ce:YIG/GGG to Si chip.	Nature Electron. 5, 604-610 (2022).
YIG	120	60*	—	—	RF sputtered poly-crystal YIG.	Journal of Materials Chemistry C 13, 12628-12649 (2025)
Bi:YIG	−1200	200*	—	—	RF sputtered poly-crystal Bi: YIG on Si.	
Ce:TbIG	−3200	—	—	—	Sputtered Ce:TbIG on Si.	ACS Photon. 6, 2455–2461 (2019)
CAFO	12000	8300	—	—	RF sputtered CAFO with buffer layers.	Optica 11, 889-895 (2024).
CFO	25600	34000	—	—	Sputtered poly-CFO on Si.	Appl. Phys. Exp. 13, 062002 (2020)
CFO	15500	—	3.6*	0.04*	Sputtered poly-CFO on Si.	IEICE Exp. 19, 20210500 (2022)
γ-Fe_2O_3	25000	350000*	—	—	—	Materials 6, 5094-5117 (2013)
This work (CFO)	33800	5400*	4.7*	0.026	vdW integration of single-crystalline CFO.	This work

Notes: MO: Magneto-optical. θ_F: Faraday rotation coefficient. α_m: material absorption loss. NRPS: non-reciprocal phase shift (based on calculation estimation), unit: rad/mm (i.e. mm^{-1}). L_{MO}: length of the MO material on waveguide. YIG: yttrium iron garnet ($Y_3Fe_5O_{12}$), TbIG: terbium iron garnet ($Tb_3Fe_5O_{12}$), CFO: cobalt ferrite ($CoFe_2O_4$), CAFO: aluminum-substituted cobalt ferrite ($CoAl_xFe_{2-x}O_4$), GGG: gadolinium gallium garnet ($Gd_3Ga_5O_{12}$), STO: strontium titanate ($SrTiO_3$). Estimated Faraday rotation values are marked with * superscript. Not reported values are marked by — symbol. Detailed explanations are made in Supplementary Note S24 in Supplementary Information.

[Redacted figure and text below]

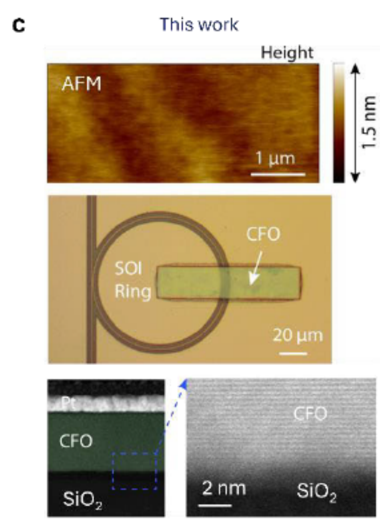

Fig. R1-2. Comparison of CFO quality to previous work. [redacted] (c) vdW-integrated single-crystalline CFO film in this work with high-quality and uniform smooth film morphology. Top panels: device optical micrographs. Bottom panels: cross-sectional SEM or TEM.

(3.3) **For III-V films vdW-integrated photodetectors performances**, this work has realized comparable photoresponsivity to previous publications using waveguides-based on-chip configurations. Specifically, by lateral stitching of freestanding GaAs and GaN nanomembranes with single-crystallinity on the same SiN photonic chip, we achieved extended wide-spectrum photodetection from 405 nm to 780 nm: 0.3 A/W at light wavelength λ = 780 nm (via GaAs-integrated photodetector), 0.16 A/W at λ = 520 nm (via GaAs), and 17 mA/W at λ = 405 nm (via GaN). This work also permits future multifunctional hetero-integrated optoelectronic applications with multi-materials co-integration on a single chip.

Detailed benchmarks on the photodetector performances of this work against state-of-the-art prior publications are made in Supplementary Note S19 (Table S2) in Supplementary Information.

(4) For the comments **regarding the applications that require the hetero-integrated stacks**, we thank the reviewer for pointing out this constructive comment. We have clarified the value, application scenarios, and potential impact of the artificial 3D heterostructures made by proposed photonic vdW integration.

• The ability to stack high-quality optical layers is crucial to realize high-performance and multifunctional hetero-integrated photonic systems, embodying the concept of '3D photonic integration'[13-15] (Ref: Nature 620, 78–85, 2023; Ref: Nature Electronics 7, 422–424, 2024), which has proven unparallelled advantages in realizing high-performance lasers (e.g. Ref: Nature 615, 411–417, 2023), amplifiers (Ref: Nature 639, 928–934, 2025), signal processing (Ref: Nature 610, 54–60, 2022), and datalinks (Ref: Nature Photonics 19, 502–509, 2025), to name a few, with fruitful achievements in recent years, by vertically integrating group III-V semiconductors and EO materials to Si and SiN photonic platforms.

• To embody this concept, we demonstrated proof-of-concept devices: (i) Lateral stitched GaAs and GaN films for expanded photodetection spectrum, and (ii) vertically stacked CFO/BTO 3D heterostructure on Si micro-ring for simultaneous EO and MO tuning. Non-reciprocal EO modulators with mitigated back-reflections for in-memory computing tasks (Ref: Nature Photonics 19, 54–62, 2025) with modified device structure, or dual-functional optical modulators for mode-division-multiplexing (MDM) applications can be enabled by the single-crystalline BTO/CFO hetero-integrated devices demonstrated in this work.

We note that only prototypical devices were demonstrated in this work to exemplify the unique advantages of photonic vdW integration approach. Armed with these single-crystalline 3D vdW building blocks, further powerful examples of 3D-stacked photonic systems are beyond the scope of this work and can be explored in future research. Further discussions are elaborated in Response 6 of this Response Letter on Page 33.

Actions taken:

We have clarified the application scenarios and vital value for the ability to construct single-crystalline 3D artificial heterostructures, with arbitrary desired functional materials on arbitrary photonic substrates in revised Supplementary Note S3 (as highlighted in yellow, on Page 8 of the Supplementary Information).

> artificial heterostructure stacked on SiO_2 substrate (Fig. S10d), GaAs, BTO, GaN, and STO are colored as yellow, green, red, and blue in the first panel, respectively. We note that this artificial heterostructure stack of GaAs/BTO/GaN/STO is only an example to embody the capability of photonic vdW integration for constructing arbitrary desired high-quality functional optical layers on arbitrary substrate, which can find great value and broad applications in multifunctional hetero-integrated photonics[41-43] and 3D photonics integration[44,45]. A more specific demonstration of such stacked photonic system is beyond the scope of this work. A versatile platform is thus created for advancing nanomembranes technology[18,46-48], studying physical coupling[2,49,50], and prototyping exotic heterogeneous integrated photonic applications[15,25,51-53].

(5) In summary, the novelty and impact of this work are clarified in three folds as below, where the crucial role of creating and integration of single-crystalline freestanding 3D nanomembranes (distinctive from conventional approaches) is highlighted for realizing heterogeneous integration and beyond.

(5.1) Advancement on the epitaxy of a library of ultrahigh-quality freestanding functional 3D nanomembranes with single-crystallinity and well-defined crystallographic orientation, demonstrating its crucial impact on various important photonic applications.

• Experimental record-high effective *in-plane* Pockels coefficient (essential for integrated photonics) for BTO r_{eff} of 950 pm/V to the best of our knowledge, corresponding to a giant r_{42} ~ 1290 pm/V approaching bulk BTO crystal, which is over 30 times higher than lithium niobate (LN) and lithium tantalate (LT). Systematic technical engineering on controlling both the crystallographic orientation and crystal quality of BTO nanomembranes, which is critical to realize efficient on-chip EO applications. By applying a-axis-domain BTO single-crystals, we achieved 153% ~ 4300%-fold performance improvement on BTO *in-plane*

r_{eff} compared to previous works (Ref: Nature Materials 18, 42–47, 2019; Ref: Nature Materials 24, 868-875, 2025. Ref: Nature 641, 876-883, 2025; Ref: Optics Lett. 28 (24), 2527-2529, 2003).

• First demonstration of freestanding single-crystalline CFO film for heterogeneous integrated non-reciprocal photonics, to the best of our knowledge.

Experimental record-high Faraday rotation coefficient θ_{F} of 33800 °/cm, which is over 100 times higher than YIG and ~10 times higher than Ce: YIG (Ref: Nature Electronics 5, 604-610, 2022; Ref: Optica 6, 473-478, 2019; Ref: Nature Photonics 19, 54–62, 2025).

• Single-crystalline GaAs and GaN freestanding nanomembranes synthesis with significantly reduced film defects.

(5.2) The first comprehensive framework on the van der Waals (vdW) integration of diverse freestanding 3D nanomembranes for heterogeneous integrated photonics, to the best of our knowledge. This method is general and widely applicable to various 3D materials.

• Demonstrating the crucial role of freestanding single-crystal 3D nanomembranes: both the freestanding form of the 3D films with artificial-delaminated vdW interfaces, and the single-crystal thin-film quality are key to enabling future advanced hetero-integrated photonic applications.

• We extend the vdW integration approach and concept to various 3D materials-based thin-films, showcasing systematic study covering single-crystal film growth, exfoliation, transfer, and device implementations.

• Compared to previous methods of direct heteroepitaxy and wafer bonding, this work serves a viable and promising alternative baseline to realize photonic hetero-integration with significantly better material quality (compared to heteroepitaxy), in a fast, convenient-to-implement, cost-saving, versatile manner (compared to wafer/die-bonding).

(5.3) Experimentally verified advantageous device performance (on par with or better than state-of-the-art levels) using photonic vdW integration of freestanding 3D thin-films, with comprehensive technical key points studied, covering optimized 3D layer transfer, design trade-offs, and device implementations that are pivotal for developing high-performance heterogeneous integrated photonics.

• For BTO EO modulators: (i) Efficient $V_{\pi} \cdot L$ of 0.29 V·cm for low-frequency MZM using BTO-Si hybrid photonic waveguide, which is among the lowest compared to most of previous BTO-based hybrid-waveguide MZMs.

(ii) A balanced and competitive experimental $V_{\pi} \cdot L$ (1.4 V·cm, limited by device fabrication, etc.) and 3 dB EO bandwidth (>23 GHz) realized simultaneously in modified device structure, by trading driving voltage to faster device speed. The experimental $V_{\pi} \cdot L$ is comparable to previous BTO-based MZMs, but the device EO bandwidth is about 3~29 times higher than previous BTO-based modulators under MZI structures (Ref: Nano Letters 14, 1419-1425, 2014; Ref: Nature 641, 876-883, 2025).

(iii) Compared to micro-ring-structure based EO modulators, the BTO Mach-Zehnder modulators (MZMs) demonstrated in this work have much broader optical operation spectrum and wider applications. If compared with LN- or LT-hetero-integrated hybrid-waveguide EO MZMs, the $V_{\pi} \cdot L$ here is over 3~6 times lower (compared to Ref: Nature Communications 17, 3314, 2026; Ref: Nature Communications 14, 4856, 2023).

• For CFO-based nonreciprocal devices: (i) High non-reciprocal phase shift (NRPS) of 4.68 rad/mm, realized within an ultrashort magneto-optical (MO) waveguide length L_{MO} of only 0.026 mm, which is $9 \sim 70$ times shorter than previous works (e.g. Ref: Optica, 6, 473-478, 2019; Ref: Nature Photonics, 19, 54–62, 2025; Ref: Nature Photonics, 5, 758-762, 2011), thanks to the giant CFO Faraday rotation coefficient.

(ii) Competitive isolation extinction ratio of 18.9 dB and mitigated optical scattering loss from CFO defects compared to previous MO devices based on CFO with poor crystal quality.

• For III-V nanomembranes vdW-integrated photodetectors: We demonstrated expanded wide photodetection from 405 nm to 780 nm, with state-of-the-art-comparable photoresponsivity by co-integrating single-crystal GaAs and GaN films on the same SiN chip.

• For additional novelty and further impact: This work experimentally verified the feasibility and unique advantages of creating exotic high-quality heterostructures using vdW integration of single-crystalline 3D photonic nanomembranes that are previously inaccessible by conventional approaches.

For instance, (i) the vertical stacking and lateral stitching of GaAs/BTO/GaN/STO artificial 3D heterostructures atop SiO_2 substrate, where all stacked layers are optimal single-crystalline but with radically distinct crystal structures. This is hardly possible via other approaches (detailed in Fig. S10 in Supplementary Note S3).

(ii) The heterogeneous co-integration and coupling of multiple different functional optical layers to prototype multifunctional integrated photonic applications. Desired optical functionality can be infused to established photonic platforms such as Si and SiN photonics by selecting the desired '3D Lego bricks' with optimal material quality.

For example, the lateral stitched GaAs and GaN single-crystals with expanded photodetection spectrum, and the vertically stacked CFO/BTO heterostructures for simultaneous EO and MO tuning of the Si micro-ring resonator. Further multifunctional or 3D hetero-integrated photonic systems synergizing different functional optical materials can be also made possible, but beyond the scope of this paper.

(iii) This work also establishes a viable future playground to study the coupling of diverse 3D nanomembranes with highest available single-crystal film quality, extending fundamental physics study from 2D heterostructures to 2D/3D (Ref: Science 384, 312-317, 2024), 3D/3D (Ref: Nature 626, 529-534, 2024; Ref: Nature Nanotechnology 20, 881-888, 2025), and beyond, without necessitating expensive facilities or lengthy process engineering.

Therefore, we sincerely believe this work has justified novelty and sufficient technical advances to be published on Nature, encompassing ultrahigh thin-film material quality, competitive device performance, and technical key points on device design and implementation, with broad potential impact from nanomaterials community to heterogeneous integrated photonics.

Actions taken:

We have further highlighted the manuscript novelty in revised main text, with detailed novelty and impact clarifications discussed in revised Supplementary Note S27 (on Page 40 of the Supplementary Information, as highlighted in yellow, shown below).

> This work can serve as a comprehensive baseline on leveraging the versatile vdW integration platform for realizing various heterogeneous integrated photonic applications, with diverse functional freestanding 3D nanomembranes, covering thin film epitaxy, lift off, and device implementations with verified unique advantages. Both the single-crystalline film quality (with well-defined crystallographic orientations) and its freestanding form with artificially laminated vdW interfaces are the two keys for enabling boundless and high-performance photonic heterogeneous integrations reported in this work. We thus highlight the critical role of creating and integrating these freestanding 3D single-crystalline films in photonics, which were not clearly elucidated with careful attention in conventional hetero-integration strategies such as direct heteroepitaxy or wafer bonding. New opportunities await in further leveraging the versatile photonic vdW integration platform to develop 3D photonic integration[44] with ultracompact footprint and unparalleled multifunctionality[1,45,165,166]. An intriguing playground thus unfolds to coalesce various functional optical layers with optimal single-crystallinity but distinct crystal structures that are hardly accessible via direct heteroepitaxial approaches, permitting emerging opportunities for heterogeneous photonic integration[1,2,15,25] and nanomembranes-related physics and technologies[7,18,19,46-49,167-169].

Comment 1:

Apart from this main concern, I hope the authors could also address the following technical comments:

1. Following my comment above, I hope the authors could more explicitly point out the membrane preparation methods (2DLT or ELO) for each material. At the moment the information is scattered here and there but difficult to find.

Response 1:

We thank the reviewer for the considerate suggestion. The methods to prepare the nanomembranes discussed in this manuscript are clarified as Table R1-4 below.

Table R1-4. Preparation methods for the single-crystalline 3D nanomembranes in this work

Thin film material		**BTO**	**CFO**	**YIG**	**GaAs**	**GaN**
Film lift-off methods studied in this work	**ELO**	✓	✓	✓	✓	✗
	2DLT	✗	✗	✓	✓	✓
Methods used for making photonic devices in this work		ELO BTO	ELO CFO	2DLT YIG* ELO YIG*	ELO GaAs	2DLT GaN
Device notes		EO modulators	MO isolators	N/A	Photodetectors	Photodetectors

Notes: ELO: epitaxial lift-off. 2DLT: 2D-materials-based layer transfer. Superscript * and N/A denote only freestanding YIG film transfer was studied, while non-reciprocal device demonstration was not carried out (discussed in Supplementary Note S25).

For freestanding nanomembranes discussed in this work, both ELO and 2DLT are studied (Table R1-4). In photonic device implementation, ELO BTO, ELO CFO, 2DLT GaN, and ELO GaAs freestanding thin films are selected.

• For EO material BTO, despite 2DLT BTO briefly studied in our prior work (Ref: Nature 578, 75-81, 2020) for pure electronic applications, the resultant remote epitaxial BTO films are predominantly *c*-axis-domain (i.e. (001) crystal plane orientation) BTO, which is unable to work effectively for integrated EO photonics (as explained in the response to previous comment).

Therefore, ELO BTO is adopted here, which allows for stronger crystallographic orientation control by simultaneously engineering the growth condition, sacrificial and buffer layers for on-chip EO applications (detailed in Methods – Thin film growth, and Supplementary Note S4).

• For MO material CFO, ELO CFO films are selected for its high-crystallinity and robustness. For freestanding YIG films, both 2DLT and ELO methods are studied and compared in this work, with their pros and cons discussed in Supplementary Note S5).

We have studied the transfer and vdW-integration of our YIG films. However, YIG-based non-reciprocal device demonstration was not carried out in this work for three reasons: (i) CFO film has more novelty and distinguished giant Faraday rotation coefficient θ_F than YIG (as YIG-based MO non-reciprocity has already been reported in prior works), and (ii) Ideal YIG film patterning is not fully optimized yet, as our current on-chip non-reciprocal devices operating at external magnetic field and TM mode require patterned MO film to facilitate evident NRPS. (iii) CFO can enable 'magnet-less' isolators without external magnets.

• For freestanding III-V nanomembranes GaAs, ELO method is applied, because we have fully optimized the desired p-i-n-doping structure (shown as Supplementary Fig. S3a) via MOCVD and ELO method. 2DLT GaAs was also explored in this work (shown as Supplementary Fig. S12c), yet our current MBE chamber for 2DLT GaAs has not been fully optimized to create desired p-i-n doping heterostructures for efficient photodetectors.

2DLT GaN films are applied for photodetector devices in this work (unintentionally doped/UID GaN, due to no optimized p-i-n doped GaN growth structure available for now), for the favorable threading dislocation density reduction of the GaN single-crystals (see Supplementary Fig. S30 in Supplementary Note S16).

Actions taken:

We have added explicit information summarizing the preparation methods of the single-crystalline 3D nanomembranes discussed in this manuscript in the revised Methods – Section 2 (Freestanding films lift-off and transfer), and in Supplementary Note S1.

Revisions made in Methods – Section 2 (as highlighted in yellow, shown below).

> transfer, and TRT-combined with Ni adhesive (and stressor) layer was found effective for most 2DLT cases. For device implementations, ELO BTO, ELO CFO, 2DLT GaN, and ELO GaAs nanomembranes are selected (detailed in Supplementary Note S1).
>
> **2DLT**
>
> Ni stressor layer sputtering (1~2×10^{-3} torr pressure, Ar flow: 8 sccm) was first conducted for as-

Revisions made in the last paragraph (Page 6) of Supplementary Note S1 (shown below) for films summary.

> In summary, a library of freestanding single-crystalline 3D nanomembranes with pivotal functionalities for integrated photonics are studied in this work, including EO material BTO (prepared via ELO method), MO material CFO (prepared via ELO) and YIG (prepared via 2DLT and ELO), and group III-V semiconductors GaN (prepared via 2DLT) and GaAs (prepared via 2DLT and ELO). Among them, ELO BTO (with favorable controllability over crystallographic orientation), ELO CFO, 2DLT GaN, and ELO GaAs nanomembranes are selected for heterogeneously integrated photonic device demonstrations.

Comment 2:

2. The authors have quoted several times the extracted EO coefficient being 40 times higher than LN. However, the finally achieved device Vpi-L values, which users care about at the end of the day, are not improved by such a dramatic value (~ 8 times for low-speed device and almost comparable for the high-speed device).

The authors have attributed the increased Vpi-L in high-speed case to fabrication imperfections in the electrodes, which may have played a role; but I believe more of this trade-off originated from the large dielectric constant of BTO that poses challenges in RF design. It is also well known that BTO's EO coefficient drops at higher frequency, which may have also been a critical limiting factor of the EO bandwidth. These trade-offs, although not having much to do with the heterogeneous integration method proposed in this paper, should be discussed in more details.

Response 2:

We appreciate the review for pointing out this important and insightful suggestion. The suggestion is well taken.

We fully agree with the reviewer on the necessity of supplementing more detailed discussions on the design, trade-offs, limitations, and practical considerations for our BTO-based modulators. Careful revisions are also made to clarify the fundamental reasons that may lead to potential confusion on the appearing discrepancy of the BTO giant r_{eff} and final device $V_{\pi} \cdot L$.

(1) **Benchmark criterion**. For comparing $V_{\pi} \cdot L$, we would like to justify that devices under similar configurations can be benchmarked together for more explicit and holistic evaluation, given that device

structure parameters, such as the optical field overlap Γ (of the EO material) and electrodes gap distance g, have drastic impact on overall $V_\pi \cdot L$ and device performance.

For device configurations, hybrid EO waveguides (i.e. the waveguide core with highest refractive index is non-EO material, such as Si and SiN; the EO modulation is realized by the evanescent coupling between the hetero-integrated EO layer and the waveguide core), and direct EO waveguides (i.e. the waveguide is directly and solely made from EO materials, such as the patterned BTO, LNOI or LTOI waveguides) also make a big difference with varying pros and cons.

(1.1) For the impact of optical field overlap Γ, it is highly dependent on device structure. This Γ largely affects $V_\pi \cdot L$, as only the optical power inside the EO material can facilitate EO modulation, the optical power in the non-EO materials (such as the SiO_2 substrate or Si waveguide core in this work) makes no contribution to overall EO modulation efficiency.

We have conducted supplementary simulations (by COMSOL Multiphysics) to illustrate the variation of $V_\pi \cdot L$ under different structures (as Table R1-5 below). The BTO ridge waveguide (the 3rd row in Table R1-5) has the highest overlap factor Γ between the guided mode and EO material (i.e. the BTO waveguide core), leading to the smallest $V_\pi \cdot L$ of 0.21 V·cm under a fixed electrodes gap distance of $g = 4$ µm.

For other hybrid EO waveguides-based modulators in Table R1-5, at fixed electrodes gap g, the resultant device $V_\pi \cdot L$ primarily depends on the portion of the optical power inside BTO (i.e. Γ), the BTO layer thickness, and the RF electrical field intensity inside BTO. As summarized in Fig. R1-3a below, thicker BTO layer and bigger Γ can generally produce smaller $V_\pi \cdot L$.

However, the high microwave impedance of BTO significantly pulls up device impedance Z_0 from the 50 Ω target value, which leads to strong RF signal reflection and poor modulator EO bandwidth. Therefore, compared to Design B (electrodes directly fabricated on BTO layer), we introduced a thick SiO_2 layer between the electrodes and BTO layer (as Design A). This drags down device Z_0 to enhance EO bandwidth, at a cost of reduced RF electric field intensity at BTO layer (i.e. increased $V_\pi \cdot L$).

Table R1-5. Benchmarks on device structure and optical field overlap Γ on device $V_\pi \cdot L$

Device structure	Key parameters	Structure illustrations	$V_\pi \cdot L$ (V·cm)	Overlap factor Γ	Optical field |**E**| distribution (fundamental TE mode)
Buried Si waveguide + BTO	t_{BTO} fixed 100 nm SiO2 spacer thickness t_{SiO2} = 20 nm	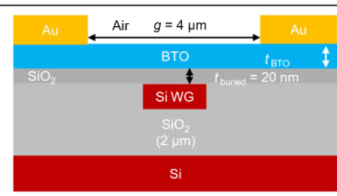	0.31	17.1%	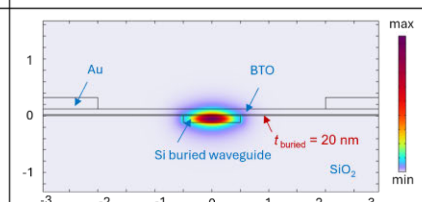
Buried Si waveguide + BTO	t_{BTO} fixed 100 nm SiO2 spacer thickness t_{SiO2} = 80 nm	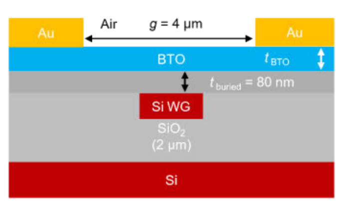	0.71	8.1%	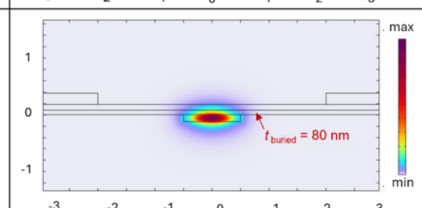
BTO ridge waveguide (Direct EO material WG)	BTO ridge height t_{ridge} = 160 nm BTO total thickness t_{BTO} = 220 nm	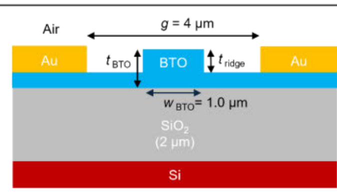	0.21	55.9%	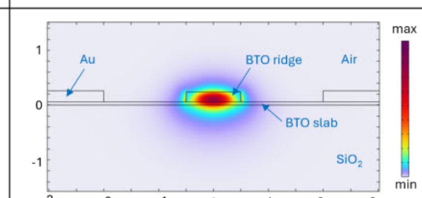

Design B	BTO thickness t_{BTO} = 100 nm Fixed g = 4 μm	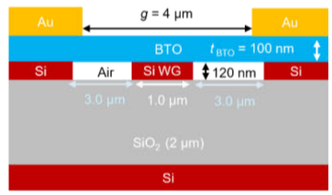	0.27	19.3%	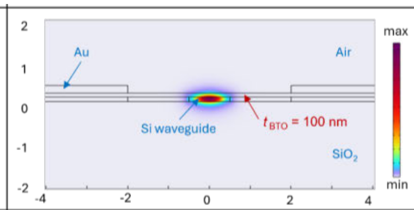
Design B*	BTO thickness t_{BTO} = 45 nm Fixed g = 4 μm	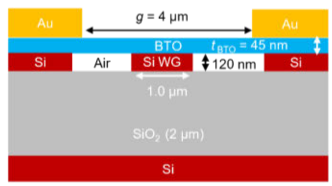	0.47	11.9%	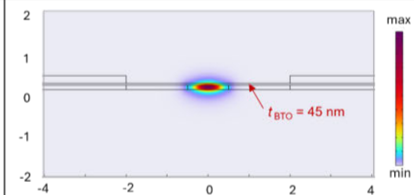
Design A*	BTO thickness t_{BTO} = 45 nm Fixed electrodes gap g = 4 μm	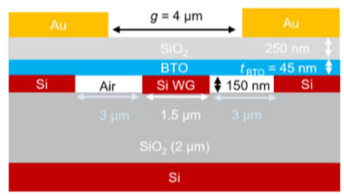	1.12	8.4%	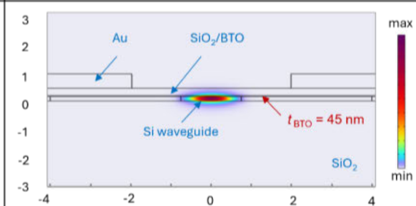
Design A**	BTO thickness t_{BTO} = 100 nm Fixed electrodes gap g = 4 μm	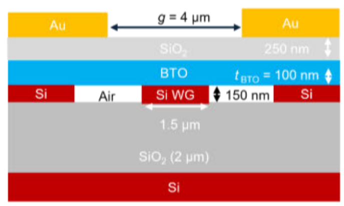	0.78	18.1%	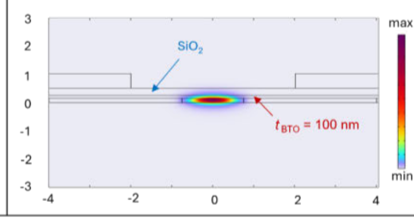

Notes: Results are calculated via COMSOL Multiphysics. Different device configurations are explored, while the BTO r_{eff} is set as 900 pm/V, and the electrodes gap distance is fixed as $g = 4$ μm for all simulations. Design B* is modified from design B (with increased BTO layer thickness). Design A* and design A** has modified structure parameters from the original design A (with changed electrodes gap g and BTO layer thickness). Except for the 'BTO ridge waveguide' (where the waveguide is directly made by patterned BTO), all other device configurations shown in this table are 'hybrid EO waveguide' structures.

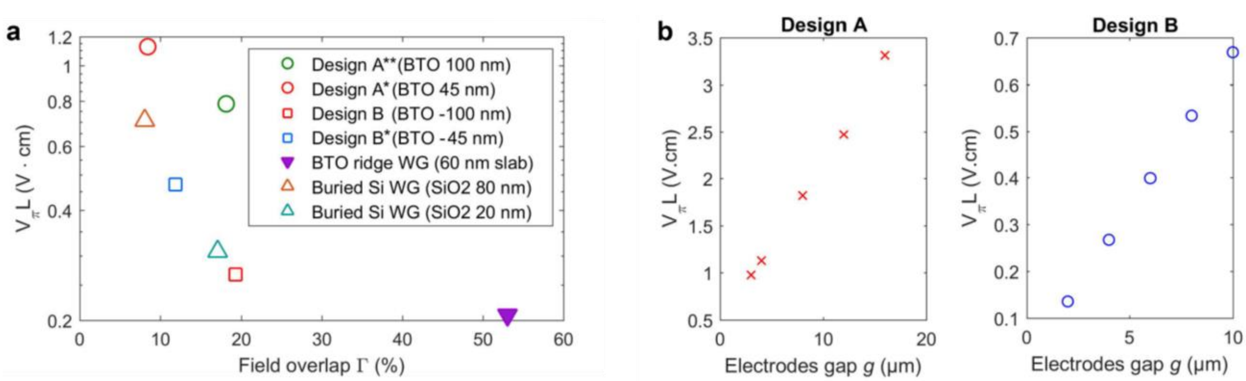

Fig. R1-3. (a) Comparison of EO modulator $V_\pi \cdot L$ under different device structures and field overlap Γ. Open symbols: hybrid waveguide structure. Filled symbol: EO material directly as waveguide core. (b) Device $V_\pi \cdot L$ as a function of electrodes gap distance g under different device structures.

(1.2) For the impact of electrodes gap distance g, we have summarized the supplementary simulation results as Fig. R1-3b above, and Table R1-6 below.

Table R1-6. Benchmarks on electrodes gap distance g on device $V_\pi \cdot L$

Electrode gap	$V_\pi \cdot L$ (V·cm)	Design B – Static electric field intensity |**E**| (V/m)	Electrode gap	$V_\pi \cdot L$ (V·cm)	Design A – Static electric field intensity |**E**| (V/m)
g = 2 μm Γ = 19.3%	0.13	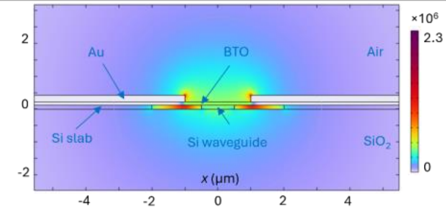	g = 3 μm Γ = 8.47%	0.97	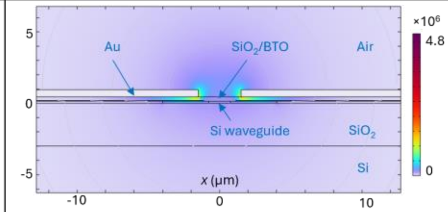
g = 4 μm	0.27	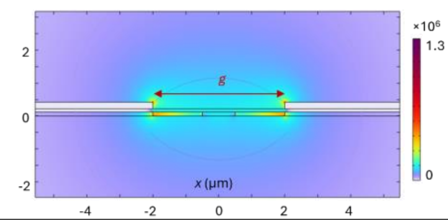	g = 4 μm	1.12	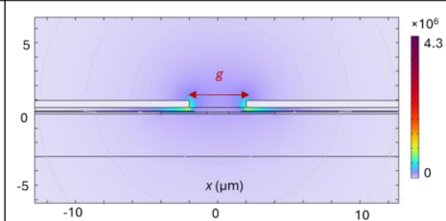
g = 6 μm	0.39	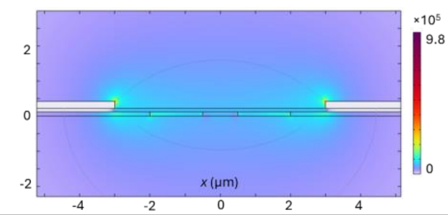	g = 8 μm	1.76	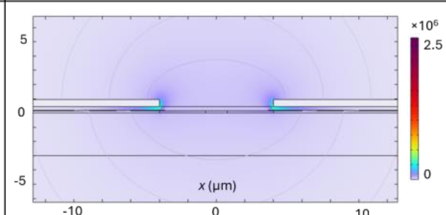
g = 8 μm	0.53	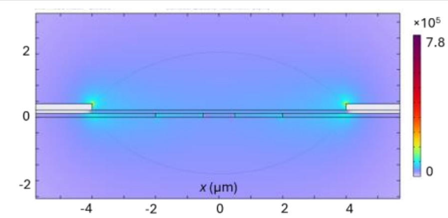	g = 12 μm	2.46	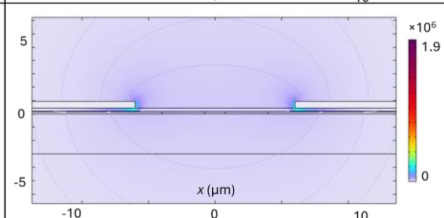
g = 10 μm	0.67	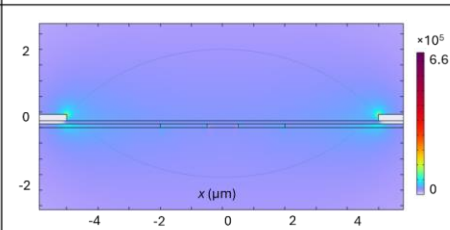	g = 16 μm	3.31	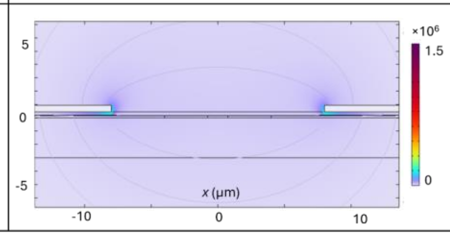

Notes: Results are simulated by COMSOL Multiphysics. Applied bias voltage between electrodes is fixed as 1 V. The optical field overlap factor Γ barely changes with g under same device design configuration. Electrodes gap distance g is marked out for comparison. In simulation, only g is altered from original device structures shown in Fig. S17a (Design A) and S17b (Design B); other device structure parameters are unchanged.

Evidently, a smaller g leads to higher electric field intensity in EO layer under given bias voltage, and thus a smaller $V_\pi \cdot L$. By reducing electrodes gap g to 3 μm and 2 μm for modified Design A and Design B respectively, the corresponding device $V_\pi \cdot L$ can be further decreased to 0.97 V·cm and 0.13 V·cm respectively, at the cost of increased optical loss and further deteriorated EO bandwidth. Therefore, we have selected the balanced designs in this work (detailed in revised Supplementary Note S10).

(2) We selected hybrid BTO-Si waveguide configuration for the EO modulators for the following reasons.

• In this work, we aim to demonstrate the concept of infusing arbitrary desired optical functionalities to established photonic platforms by selecting the single-crystalline freestanding 3D vdW building blocks, to realize boundless photonic heterogeneous integration on arbitrary substrates but with highest available material quality. This vdW integration strategy for 3D freestanding layers may further reshape the landscape of photonic hetero-integration by providing another viable alternative for established foundries for future large-scale hetero-integrated PICs.

• Leverage the maturity of established Si and silicon nitride (SiN) photonics platform. For instance, despite LNOI and LTOI photonics are already available, the heterogeneous integration of LN (Ref: Nature Communications 14, 4856, 2023) and LT (Ref: Nature Communications 17, 3314, 2026; Ref: Nature Photonics 20, 225–231, 2026) to Si and SiN photonics as hybrid EO waveguides still shows good performance and broad impact. This is because for foundry and especially commercialization level, the robustness and maturity of pure LNOI and LTOI are still under developing and are not yet comparable to Si or SiN photonics so far in terms of reliability, yield, and cost.

• The hybrid EO waveguide configurations used in this work circumvent the lengthy and stringent optimization process required for BTO drying etching demanding smooth waveguide side walls.

(3) In summary, the potential confusion of the giant BTO effective Pockels coefficient r_{eff} with overall device $V_\pi \cdot L$ mainly comes from two folds.

• The $V_\pi \cdot L$ for devices realized in this work are based on BTO-Si hybrid waveguide structures. Despite the experimental BTO r_{eff} about 40 times higher than LN, the devices $V_\pi \cdot L$ in this work can appear to be not so drastically improved, if directly compared to LNOI or LTOI-based EO modulators (i.e. not hybrid waveguide configurations). This is because they have different device structures, and the optical field overlap factors Γ for direct LNOI modulators are intrinsically higher than hybrid EO waveguides.

• BTO-based MZMs are distinctive from LNOI- and LTOI-based EO modulators, especially the orders of magnitudes higher microwave permittivity of BTO than LN. This poses non-negligible attention required for designers to catch the 50 Ω device impedance Z_0, and match the group velocities between the microwave and optical signals for high-speed travelling wave electrodes.
Consequently, we intentionally sacrificed device $V_\pi \cdot L$ in this work for higher device EO bandwidth, which is one of the front-standing issues for BTO-based MZMs in previous works.

(4) Despite the abovementioned factors, the overall devices $V_\pi \cdot L$ realized in this work still show evident improvements compared to LN- and LT-based EO modulators.

Conventional LNOI-based EO MZMs (not hybrid waveguide) have typical $V_\pi \cdot L$ around 2~3 V·cm (Ref: Advances in Optics and Photonics 13, 242, 2021), which is about 8~12 times higher than the $V_\pi \cdot L$ for BTO-based MZMs reported in this work. If we further fairly compare this work with prior publications using similar hybrid EO waveguide configurations, our resultant BTO $V_\pi \cdot L$ in this work is about 3~6 times (for 'Design A') and 12~28 times (for 'Design B') lower than previous works (Ref: Nature Communications 14, 4856, 2023; Ref: Nature Photonics 20, 225–231, 2026).

Actions taken:

We agree with the reviewer that the large BTO microwave dielectric constant indeed poses challenges in high-speed EO device design. The gradual drop of BTO EO Pockels coefficient at higher frequency, and the nonideal electrode fabrication factors all contribute to overall device performance (revised accordingly).

For the variation of BTO Pockels coefficients at high frequencies, according to the published Fig. 4b in Ref[16]: Nature Materials 24, 868–875, 2025), its Pockels coefficient drops about ~50% from ~1 MHz to 100 GHz. Nevertheless, the dropped Pockels coefficient value is still over 10-fold higher than LN and LT, and the gradual decreasing r_{eff} may still find value in majority of integrated EO applications from 10- to 100-GHz and beyond. This is also an interesting and fundamental question to explore its physical origins from BTO ferroelectric domains and analyze its further impact on BTO-based integrated EO applications. Nevertheless, this direction is beyond the scope of this work, which can be further studied in future works.

We sincerely appreciate the reviewer for this constructive comment. We have added extended detailed discussions on these trade-offs and practical design considerations to the revised Supplementary Note S10 (highlighted in yellow, on Page 19 of the Supplementary Information).

> Therefore, we applied a balanced device structure (namely 'design A') to trade device $V_\pi \cdot L$ for a higher EO bandwidth for realizing high-speed BTO MZMs, with reduced electrodes microwave loss (Fig. S19a) and a better catch device impedance Z_0 to the target value of 50 Ω (Fig. S19b). Compared to 'design B' (Fig. S17b), device configuration 'design A' (Fig. S17a) exhibits a largely improved theoretical EO 3 dB bandwidth (Figs. S19c-S19f, simulated via COMSOL Multiphysics). The large BTO microwave permittivity, varying BTO Pockels coefficients at higher frequency (Ref.[37]), and especially the non-ideal device electrodes fabrication (Supplementary Note S15) all contribute to the discrepancy between the theoretical and experimental device EO bandwidth, for challenges in designing ideal ultrahigh-speed BTO MZMs. We note that this proof-of-concept 23 GHz experimental 3 dB EO bandwidth for our current BTO MZMs has already outperformed previous works using similar designs (i.e. BTO MZMs)[74-76] (detailed in Supplementary Note S12) with further room of improvement. Compared to prior microring resonators-based BTO EO modulators[35,36,54], the BTO MZMs demonstrated in this work have significantly broader operation spectrum than microring modulators.

Comment 3:

3. Similar to the above comment, the authors have mainly quoted the extracted Faraday rotation coefficient of the MO material, but it would be beneficial if the authors could directly compare the device performance (e.g. NRPS) with previous reports. It is also important to include and compare the propagation loss of the device with previous works.

Response 3:

We thank the reviewer for the constructive comment. The suggestion is taken fully.

Actions taken:

We have modified the benchmark table (Table S3) for magneto-optical (MO)-materials-integrated devices, including device performance parameters for direction comparison: nonreciprocal phase shift (NRPS), device propagation loss, and the effective length of the MO waveguide L_{MO}, as revised Table S3 (appended below, highlighted in yellow) in Supplementary Note S24 with comparative discussions added accordingly.

Table S3 – Benchmarks of reported MO materials and devices.

MO Material	θ_F (°/cm)	Material loss α_m (dB/cm)	Propag. loss α_{wg} (dB/cm)	Operation λ (nm)	FOM (°/dB)	NRPS (rad/mm)	MO WG length L_{MO} (mm)	Notes on material preparations	Ref
Ce:YIG	-1500	—	—	1550	—	1.9*	0.85*	Sputtered Ce: YIG film on Si with YIG buffer.	141
Ce:YIG	-3000	—	31.9	~1550	—	0.55*	5.6*	Wafer bonding of Ce:YIG film to SOI microring.	142
Ce:YIG	-3200	60*	6.3*	1550	53	0.79*	2*	Wafer bonding of Ce:YIG film to SOI.	143
Ce:YIG	−5900	137*	31.7	1550–1570	43	1.57*	1*	PLD Ce: YIG on SiN with YIG buffer layer.	144
Ce:YIG	-4000	—	14.5	1550	—	0.98*	0.92*	Wafer bonding of Ce: YIG dies.	145
Ce:YIG	-830	45	—	1550	21	—	—	Poly-crystal YIG growth.	146

Ce:YIG	−1263	—	—	1540–1550	—	0.63*	0.2*	PLD poly-crystal Ce: YIG on Si.	147
Ce:YIG	-3500	—	13	1550	—	0.5*	0.22*	Wafer bonding of Ce: YIG/GGG to Si photonics.	54
YIG	100	50*	—	1550	2	—	—	Direct grown poly-crystal YIG.	146
YIG	120	60*	—	1550	2	—	—	RF sputtered poly-crystal YIG.	131
Bi:YIG	−1200	200	50*	1550	6	—	—	RF sputtered poly-crystal Bi: YIG on Si.	131
Bi:YIG	-838	150	—	1550	5.6	—	—	liquid phase epitaxy on GGG.	131
Ce:TbIG	−3200	—	15*	1550	—	—	—	Sputtered Ce:TbIG on Si.	148
TbIG	-1100	—	20*	1550	—	—	—	Sputtered Ce:TbIG.	131
CAFO	12000	8300*	—	~1550	1.5	—	—	RF sputtered CAFO with different buffer layers.	135
CFO NPs	310	130*	—	820, 1550	2.4	—	—	CFO nanoparticle composites.	133
CFO	25600	34000	—	1550	0.8	—	—	Sputtered CFO on Si.	134
CFO	15500	—	210	1545–1550	—	3.6*	0.04*	Sputtered CFO on Si.	132
$BaFe_{12}O_{19}$	5000*	60000*	—	~1550	0.08	—	—	PLD growth. Magnet-less operation.	149
γ-Fe_2O_3	25000	350000*	—	1550	0.07	—	—	—	146
LSMO	2000	80000*	—	460, ~1550	0.025	—	—	Ion-plasma evaporation on STO substrates.	150
Ga:STF	-400	110*	—	1550	3.6	—	—	—	146
STC	-500	350*	—	1550	1.4	—	—	—	146
STF	-780	700*	—	1550	1.1	—	—	—	146
This work (CFO)	33800	5400*	9*	1550	6	4.68	0.026	vdW integration of single-crystalline CFO film. Magnet-less optical isolation.	\

Notes: θ_F: Faraday rotation coefficient. α_m: material absorption loss. α_{wg}: the estimated device propagation loss for the magneto-optical (MO) waveguide. λ: Light wavelength. FOM: figure of merit, defined as $|\theta_F|/\alpha_m$. NRPS: non-reciprocal phase shift (based on calculation estimation). L_{MO}: length of the MO material-integrated waveguide (WG). YIG: yttrium iron garnet ($Y_3Fe_5O_{12}$), TbIG: terbium iron garnet ($Tb_3Fe_5O_{12}$), CFO: cobalt ferrite ($CoFe_2O_4$), CAFO: aluminum-substituted cobalt ferrite ($CoAl_xFe_{2-x}O_4$), GGG: gadolinium gallium garnet ($Gd_3Ga_5O_{12}$), STO: strontium titanate ($SrTiO_3$). NPs: nanoparticles, LSMO: lanthanum strontium manganite ($La_{0.7}Sr_{0.3}MnO_{3-\delta}$), STF: strontium titanate-ferrite oxide ($Sr(Ti,Fe)O_{3-\delta}$), STC: strontium titanium cobalt oxide ($Sr(Ti,Co)O_{3-\delta}$), Estimated Faraday rotation values are marked with * superscript. Not reported values are marked by — symbol. Approximate operation wavelengths are marked with ~ symbol. Most directly grown MO films are polycrystalline.

Revised discussions in Supplementary Note S24 (shown below) on Page 37 of Supplementary Information.

S24. Benchmarks of MO material CFO

The benchmark details for different MO materials are shown in Fig. S36 and Table S3. CFO exhibits giant Faraday rotation coefficients and magnet-less operation capability compared to other magnetic materials. Device performance parameters, such as the non-reciprocal phase shift (NRPS), effective length of the magneto-optical (MO) waveguide L_{MO}, and propagation loss of the MO waveguides α_{wg} are benchmarked as well in Table S3. Thanks to the giant CFO Faraday rotation coefficient, a big NRPS can be realized in an ultracompact length L_{MO} of about 26 µm. The optimal single-crystalline nanomembrane quality also enhances magnetic response and reduces optical losses from defects scattering and imperfect CFO crystal quality found in previous works[21,137,139], circumventing the prior obstacles of lattice mismatching for defective heteroepitaxial CFO layer by applying photonic vdW integration[25].

As manifested in Table S3, large device NRPS is achieved in this work, thanks to the giant Faraday rotation coefficient of CFO compared to YIG. The MO waveguide propagation loss is mitigated as well, if compared to previous works based on poly-crystalline CFO directly sputtered on Si with significant material defects.

Comment 4:

4. For the BTO device, the measured additional propagation loss is 2.5 dB/cm, which is quite substantial. Please comment on the origin of this extra loss. Since this device does not involve patterning BTO, I would

assume this came from material itself, which raises questions on the material quality prepared using the proposed method, as recent papers have demonstrated propagation loss as low as 0.32 dB/cm in etched BTO devices (arXiv:2507.17150).

<u>Response 4</u>:

We thank the reviewer for raising this important comment. We agree with reviewer on the necessity of clarifying the origin of extra optical loss. We have thus performed additional experiments to confirm that this additional loss mainly comes from the film transfer and non-ideal device fabrication processes.

(1) For the intrinsic BTO material loss, we have measured the spectroscopic ellipsometry (SE) of the as grown BTO sample, confirming low BTO material loss.

• We measured the real (n) and imaginary part (k) of an 80-nm-thick BTO grown on STO ($SrTiO_3$) substrate with thin buffer layer (via J.A. Woollam alpha-SE Spectroscopic Ellipsometer). The measured BTO (n, k) is shown as Fig. R1-3a below, which is limited by the maximum measurement range of the ellipsometer tool (~890 nm).

The measured BTO k is about 2×10^{-6} at 890 nm (Fig. R1-3a), with a good model fit (Fig. R1-3b), which corresponds to an optical loss around 1 dB/cm at 890 nm. In near infrared (NIR) wavelength (1550 nm), the expected BTO k and loss will be much lower (Ref: R. W. Boyd, Nonlinear Optics, 511-523 Springer, 2008).

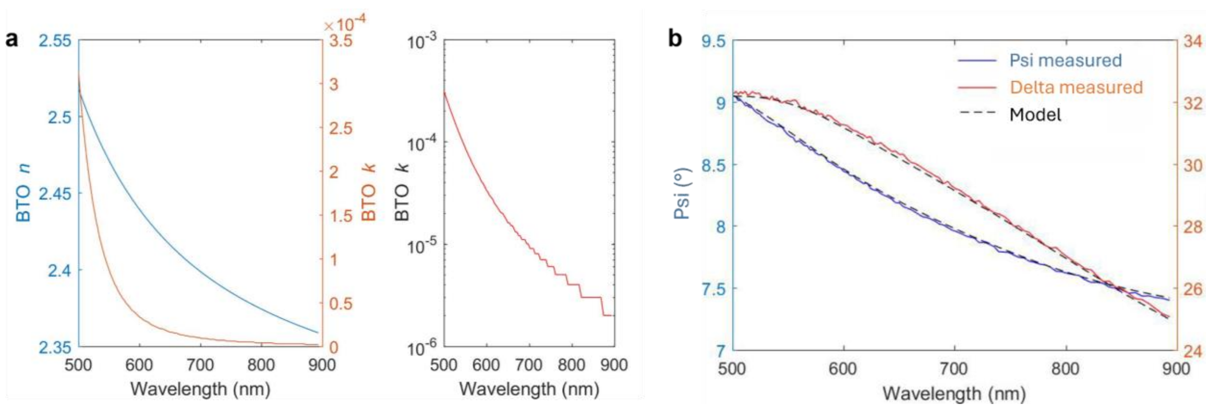

Fig. R1-3. (a) Spectroscopic ellipsometer (SE) measured BTO film complex refractive index (n, k) (left panel) and replotted BTO k in logarithmic y-scale (right panel). The stairs-like shape in BTO k curve is due to the limited SE tool measurement resolution in k and the logarithmic scale plot in y-axis. (b) Spectroscopic ellipsometer model fit.

• To further confirm BTO intrinsic material loss at the telecom wavelength, the as-grown BTO sample is further measured by a variable angle spectroscopic ellipsometer (J.A. Woollam VASE). Due to the unsatisfactory wide-spectrum fitting error of the multi-layers-stack BTO/SAO/STO samples (Fig. R1-4a), we measured a 50-nm-thick BTO film k directly grown on STO substrate (i.e. BTO/STO) instead with similar crystallinity and theoretically identical optical index at near infrared wavelengths. The measured BTO k is below 2×10^{-7} at 1550 nm (shown as Fig. R1-4b below), corresponding to a low material loss of about 0.07 dB/cm, which is sufficiently low for most integrated photonic applications.

Therefore, based on the spectroscopic ellipsometry and BTO material characterization results (including the XRD and EBSD mapping shown in Fig. 1 in main text, and the HR-TEM shown in Supplementary Fig. S24), we can conclude that the intrinsic material loss of our grown BTO films remains low, thanks to its single-crystal high-quality with minimal material defects.

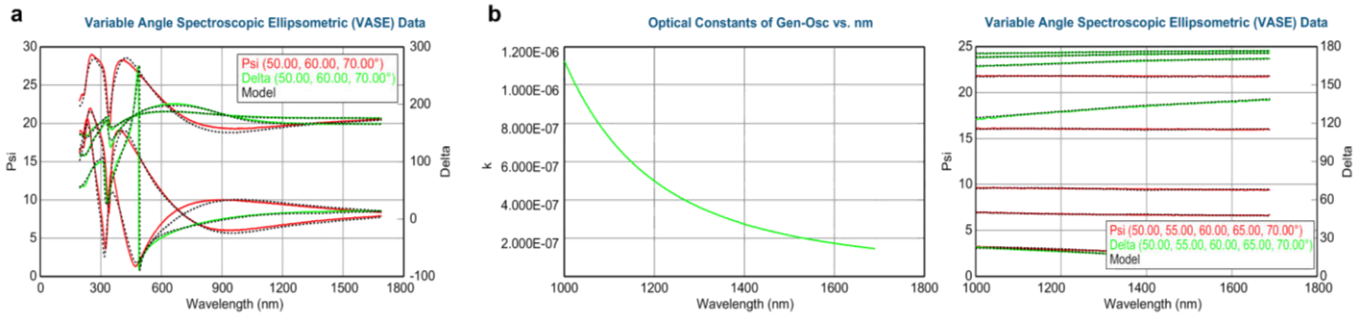

Fig. R1-4. (a) Variable angle spectroscopic ellipsometer (VASE) model fit for BTO/SAO/STO sample. (b) Left panel: Measured BTO film k at near infrared (NIR) wavelength for the BTO/STO sample. Right panel: corresponding VASE model fit.

(2) The extra optical loss thus mainly comes from the 3D functional layer transfer and nonideal device fabrication processes.

• The major contributing factor is imperfect device fabrication. Due to the facility limitations (in WUSTL IMSE cleanroom) for BTO MZMs device fabrication, we applied aligned e-beam lithography (EBL) with PMMA for thick electrodes fabrication instead of photolithography due to its unsatisfactory tool alignment resolution here. This process leads to non-vertical and sometimes burred electrodes side walls (highlighted in the red dashed rectangle in Fig. R1-5b below, right panel).

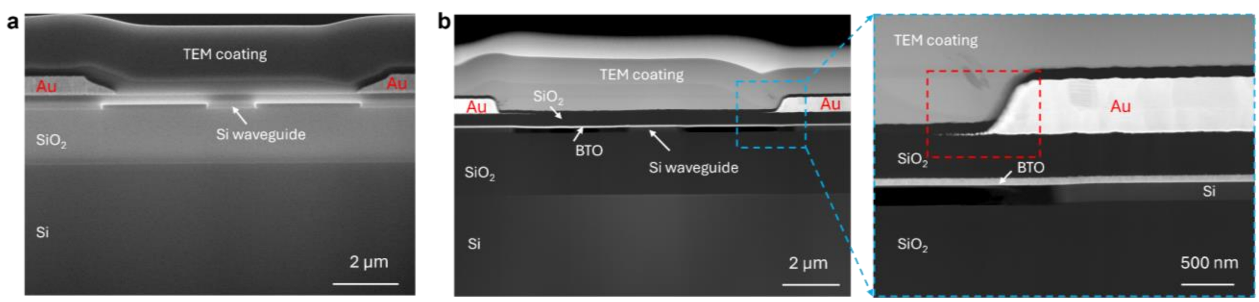

Fig. R1-5. Device cross-sectional TEM images for two different BTO MZM samples with non-vertical (a) and burred (b) electrodes side walls. Top layers: Pt composite coating for TEM imaging.

Our initial several trials yield collapsed electrodes shown as Fig. R1-5a above. After rounds of optimizations, nonideal electrodes are still sometimes observed in the final BTO MZMs (Fig. R1-5b), where those nonideal electrodes side walls contribute to device optical loss. This also highly impacts the MZMs microwave performance, deteriorating it from theoretical designs (as mentioned in the first response point (3) on Page 8 of this Response Letter).

• Despite the overall high-quality of vdW-integrated BTO freestanding nanomembranes (discussed in Supplementary Note S1 and Supplementary Fig. S7, as appended below), scattered transfer imperfections may still happen as another source of additional loss, as the devices demonstrated in this work have a quite big size of 3D nanomembranes-covered region (~1 cm × 1 cm).

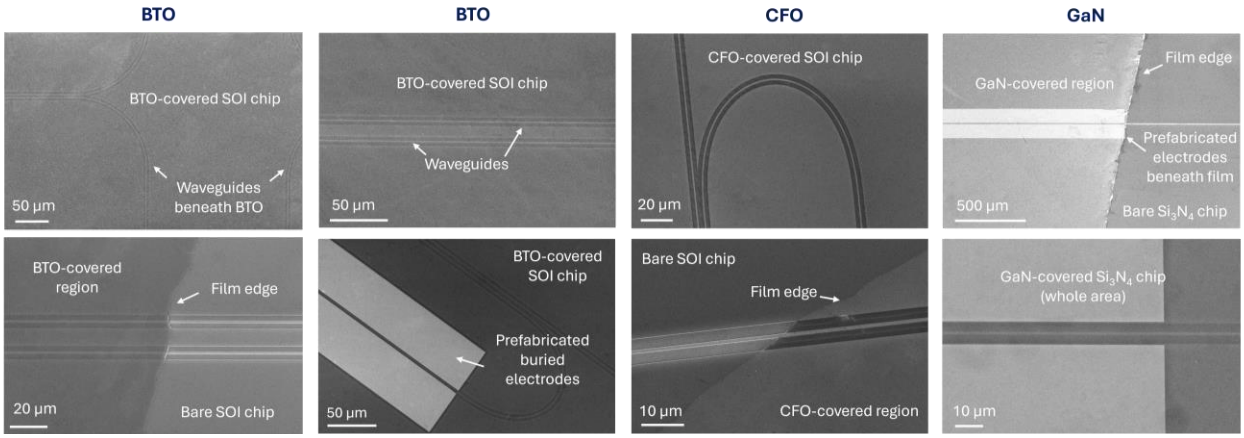

Figure S7. SEM on various vdW hetero-integrated nanomembranes on Si and SiN photonic chips showing uniform and clean surface morphology (in Supplementary Note S1).

Some process-induced defects, such as wrinkles and cracks, may still occasionally happen due to the large-sized 3D nanomembranes used (shown as Fig. R1-6 below), inducing optical losses near the local defective regions. Nevertheless, the majority of vdW-integrated film areas show high uniformity and quality for heterogeneous photonic applications (detailed in Supplementary Note S1, Fig. S6), despite the initial proof-of-principle demonstrations here. In this work, these 3D nanomembranes are handled and transferred by our human hands, which can be further improved by applying developed or automated film transfer setups (e.g. those in Ref: Nature Photonics 20, 225–231, 2026, and Refs.[17-20]).

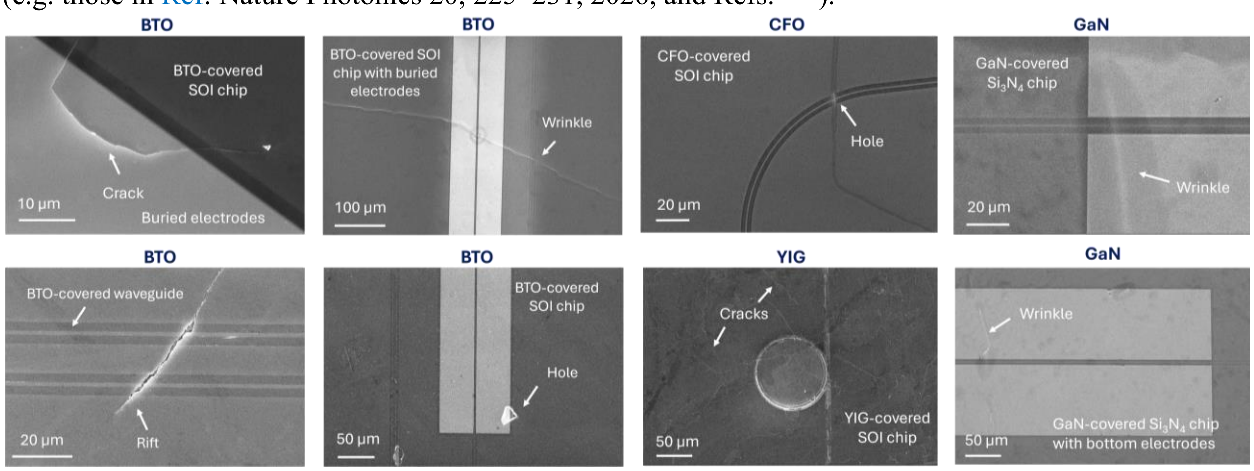

Fig. R1-6. SEM images of some occasional process-induced defects during photonic vdW integration.

(3) We have further benchmarked of the optical losses of this work against prior publications with hybrid waveguide configurations (Refs.[21-23]) as Table R1-7 below.

Heterogeneous integrated hybrid waveguides (i.e. functional layers coupled with Si or SiN waveguide core) typically have higher optical loss compared to non-hybrid structures with carefully optimized patterning and dry-etching, given that longer light evanescent tails penetrating through the hetero-interfaces to facilitate sufficient coupling to functional layers. This leads to higher sensitivity to structure surface roughness, defects, and process residues, etc., and comparatively higher propagation loss. Nevertheless, hybrid waveguide configuration can synergize the maturity and robustness of established photonic platforms, proven a vital and viable option for photonic heterogeneous integration from lab to foundry[9,15,24-26].

As manifested in Table R1-7 below, the 2.5 dB/cm extra loss (overall optical loss 3.5~5 dB/cm) is indeed higher than/on par to some LN-based hybrid photonic waveguides loss. However, we would like to justify that the experimental optical loss of the BTO MZMs in this work is lower than or comparable to many previously published BTO-based hybrid waveguides (as highlighted in blue in Table R1-7 below), with optical losses ranging from 2 dB/cm to over 10 dB/cm (Refs.[2,27-31]).

We sincerely appreciate the reviewer on this constructive comment. As BTO-based EO photonic devices are still in their early stages compared to LN, we will further work on reducing its optical loss in future works, by improving the device fabrication (as discussed above) and 3D nanomembrane transfer-integration setups and processes to unlock broader applications and impacts.

Table R1-7. Benchmarks on optical loss of various hybrid waveguides.

Hybrid WG structure	WG core material	Functional layer	Hybrid WG loss (dB/cm)	Integration method	Ref.
Si + LN	Si	LN	4.3	LN layer bonding to Si.	Scientific Reports 6, 22301 (2016)
Si + LN	Si	LN	0.98	BCB bonding of LN layer.	Nature Photonics 13, 359–364 (2019)
Si + LN	Si	LN	0.8	LN wafer bonding to Si.	Scientific Reports 12, 18611 (2022)
Si + LN	Si	LN	15	Deposited a-Si core atop LNOI.	APL Photonics 7, 126103 (2022)
Si + LN	Si	LN	1.2	LN film transfer integration.	Mater. Today Commun. 40, 109834 (2024)
SiN + LN	SiN	LN	2.03	Deposited SiN and chip bonding	Optics Express 32, 9171-9183 (2024)
SiN + LN	SiN	LN	2*	Bonded thib-film LN to SiN.	Optica 10, 5, 578-584 (2023)
BTO + Si	Si	BTO	10*	MBE grown BTO bonded to Si.	Nature Materials 18, 42–47 (2019)
BTO + Si	Si	BTO	5.8	MBE grown BTO wafer bonding.	J. Lightwave Technol. 37, 1456 (2019)
BTO + Si	Si	BTO	6*	MBE grown BTO wafer bonding.	J. Lightwave Technol. 34, 1688 (2016)
BTO + Si	Si	BTO	44	Deposited a-Si on grown BTO/Si.	Nano Lett. 14, 1419–1425 (2014)
BTO + Si	Si	BTO	6	Grown BTO on SOI.	ACS Photonics 3, 1698–1703 (2016)
BTO + Si	Si	BTO	2	Grown BTO on SOI.	J. Appl. Phys. 134, 073101 (2023)
BTO + Si	Si	BTO	11.3	Grown BTO on SOI.	Adv. Photon. Nexus 3, 066005 (2024)
BTO + SiN	SiN	BTO	5.6	Grown BTO bonded to SOI	Nature Materials 19, 1164–1168 (2020)
BTO + SiN	SiN	BTO	9.4	MBE grown BTO deposited SiN.	ACS Photonics 6, 2677–2684 (2019)
PZT + Si	Si	PZT	5.2	Grown PZT on SOI.	Optics Letters 49, 6353-6356 (2024)
PZT + Si	Si	PZT	2	Grown PZT on SOI.	Nature Communications 16, 6340 (2025)
YIG + Si	Si	Ce: YIG	40*	Bonded Ce: YIG to SOI.	Optica 4, 23-30 (2017)
YIG + Si	Si	YIG	81	Grown YIG on Si.	Opt. Mater. Exp. 14, 1579-1589 (2024)
YIG + SiN	SiN	Ce: YIG	2*	Grown Ce: YIG on SiN.	Optica 7, 1555-1562 (2020)
YIG + SiN	SiN	Ce: YIG	15*	Grown Ce: YIG on SiN.	Optica 6, 473-478 (2019)
TbIG + Si	Si	Ce: TbIG	14.7	Grown TbIG on SOI with SiN.	ACS Photonics 6, 2455–2461 (2019)

Notes: WG: waveguide. SiN: silicon nitride (Si_3N_4). LN: lithium niobate. BTO: barium titanate. PZT: lead zirconate titanate. YIG: yttrium iron garnet. TbIG: terbium iron garnet. SOI: silicon-on-insulator. LNOI: lithium niobate-on-insulator. Superscript * represents calculated or estimated values from references data.

(4) For the 0.32 dB/cm BTO device loss reported in the preprint (arXiv:2507.17150), it is based on directly patterned BTO with attentively optimized dry etching for smooth BTO waveguide side walls, in which case typically show lower optical loss than hybrid waveguide configurations (as mentioned above).

The endeavors in optimizing BTO dry etching for reduced waveguide loss are indeed very valuable. However, this Ref.[32] using directly grown BTO on SiO_2 is fundamentally limited by heteroepitaxial lattice mismatch, which only yields amorphous to poly-crystalline BTO layer with poor crystal quality. A compromised BTO effective Pockels coefficient r_{eff} of 162 pm/V (Ref: arXiv:2507.17150) is thus reported, a further improvement of which is thus extremely challenging and fundamentally blocked by material physics. This referred[32] r_{eff} of 162 pm/V is also about 6 times lower than our experimental BTO r_{eff} realized via photonic vdW integration with single-crystalline freestanding BTO films.

Actions taken:

We have added the measured BTO spectroscopic ellipsometry data with related discussions to the new Supplementary Note S14 and Fig. S27 (highlighted in yellow, on Page 28 of Supplementary Information).

Additional material characterization data confirming the good material quality of the BTO nanomembranes with minimal material defects are also appended in Supplementary Figs. S24 ~ S26.

Spectroscopic ellipsometry (J.A. Woollam alpha-SE Spectroscopic Ellipsometer) is also performed to characterize the intrinsic material loss of BTO (via an 80 nm-think BTO as-grown BTO film on STO substrate with thin interlayer). The measured BTO complex refractive indices (n, k) are shown in Fig. S27a with good model fit (Fig. S27b). The measured BTO k at 890 nm (limited by the maximum tool measurement range) is about 2×10^{-6}, corresponding to an optical loss about 1 dB/cm at 890 nm wavelength. Further variable angle spectroscopic ellipsometer (VASE) measurements via another SE tool (J.A. Woollam VASE) also confirms lower BTO intrinsic material loss[33] at the telecom wavelengths. The measured BTO k at 1550 nm wavelength is around 2×10^{-7}, corresponding to a low BTO material loss of about 0.07 dB/cm, which is enabled by the high-quality of the freestanding BTO films and this loss remains low for majority of integrated photonic applications. The source of additional optical loss mainly comes from the 3D nanomembrane transfer and subsequent nonideal device fabrication processes.

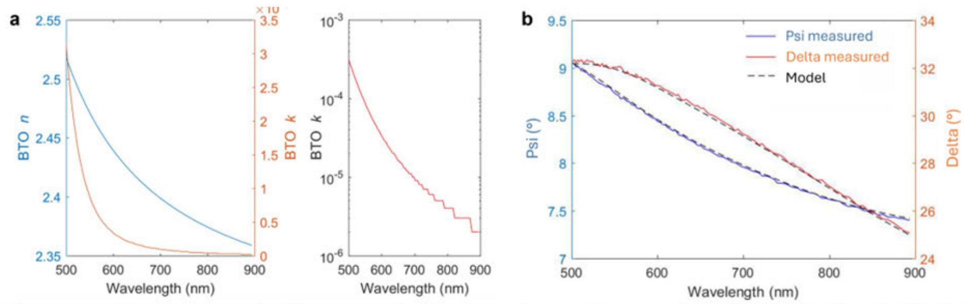

Figure S27. (a) Spectroscopic ellipsometer (SE) measured BTO film complex refractive indices (n, k) (left panel) and replotted BTO k in logarithmic y-scale (right panel). The stairs-like shape in BTO k curve is due to the limited SE tool measurement resolution in k and the logarithmic scale plot in y-axis. (b) SE model

Explanations for the impact of nonideal electrodes are added to revised Supplementary Note S15.

S15. Supplementary high-speed BTO MZMs measurement data

The experimental setup for high-speed EO MZMs is shown in Fig. S28a (and Methods), where the EO scattering parameter S_{21} (as ratio of powers) was characterized by a 67 GHz vector network analyzer (VNA, R&S ZNA67).

The microwave measurements of the high-speed BTO MZMs are shown as Figs. S28b-S28e. The discrepancy between measured and designed device performances is mainly ascribed to the imperfect travelling-wave electrodes fabrication with non-vertical side walls due to cleanroom facility constraints (Supplementary Note S9), which can induce additional losses and can be also evidenced by the partially collapsed nonideal electrode edges shown in the SEM images of Fig. 2i (in main text), Fig. S22b and Fig. S23 (left panels). Nevertheless, an over 23 GHz EO 3 dB bandwidth is still experimentally confirmed

The brief benchmarks of the device optical loss to previous works based on BTO hybrid waveguide structures are added to revised Supplementary Note S15 (on Page 29 of the Supplementary Information), mentioning further directions of improvement as well. The reference mentioned (arXiv:2507.17150) is also added to revised Supplementary Information as Ref. 79.

depending on chip dicing. Compared to wafer bonded LN and LT to Si and SiN photonics (with sophisticated and lengthy substrate grinding, polishing, and etching processes), the heterogeneous integration of BTO is still in its early stages, with comparatively higher optical loss for the BTO hybrid waveguides as reported in prior works[35,36,54,85,116]. These proof-of-concept results can be further enhanced in optical coupling by applying professional foundry-based photonic chips, with mitigated optical loss by further enhancing device fabrication and optimizing the 3D nanomembrane transfer integration setups and processes to unlock broader applications and impacts. Asymmetric optical phase modulation is also observed (Figs. S29c) due to ferroelectric material BTO, which could be further exploit to develop photonic memories[117] but beyond the scope of this paper. Detailed device EO bandwidth characterization data

Comment 5:

5. For the photodetectors, the dark currents are not explicitly quoted but looking from the figures they seem to be not particularly low. Please quote the numbers and discuss potential causes in more details.

Response 5:

We thank the reviewer for this constructive comment. We have made revisions accordingly.

The dark current values for the vdW-integrated GaAs-SiN photodetectors shown in Fig. 3f left and right panels are 16.4 nA and 19.8 nA respectively (at -2 V bias voltage). The dark current for the GaN-SiN photodetector shown in Fig. 3m is 45.6 nA (at +5 V bias voltage). The reasons for the previous dark currents appearing to be not very low are two folds: imprecise measurement setup, and the relatively big effective sizes of the initial devices shown in this work.

We have thus fabricated new batches of devices and measurements to fulfill the suggestion. Explicit photodetector dark current values, additional experiments, and related discussions are added to both the revised manuscript and Supplementary Information.

(1) In previous photodetector dark current measurements, the setup still has low ambient lab illumination (i.e. not totally dark) that was unable to fully eliminate, making the 'dark currents' shown in the original manuscript imprecise and bigger than the actual values.

• Given that the prior GaAs photodetector samples (over 8 months ago, without SiO_2 cladding) had seen oxidized GaAs layer and showed degraded light in-coupling when we tried for remeasurements, we have fabricated new batches of freestanding III-V nanomembranes vdW-integrated photodetectors for consistent dark current characterizations. The impact of air gap h is analyzed (detailed in Supplementary Note S18).

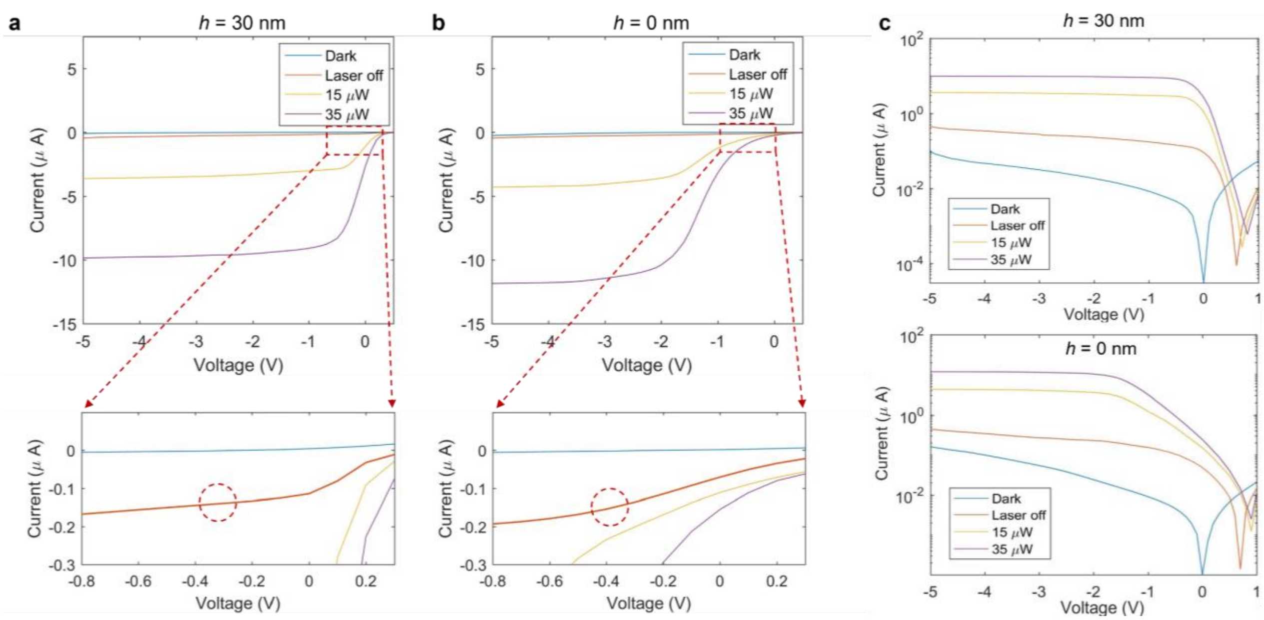

Fig. R1-7. I-V curve for the new batches of GaAs-SiN photodetectors with air gaps (a) h = 30 nm, (b) and h = 0 nm (buried electrodes structure in pre-etched SiN region for direct layer contact between SiN waveguide and the III-V nanomembranes), respectively. The dark currents are measured in a separate and fully enclosed probe station setup. Bottom panels: details zoom-in. Red dashed circles: I-V curves measured under laser-off and dim lab illumination condition, which was inaccurately quoted as 'dark currents' in the original manuscript. (c) Corresponding logscale (y-axis) plot for I-V curves.

Specifically, we applied native GaAs oxide removal (via diluted HCl) and passivation (via ammonium sulfide solution) to reduce carrier scattering and trapping[33] (Ref: ACS Applied Electronic Materials 4, 3399-3410, 2022; Ref: Nature Photonics 19, 1178-1188, 2025) for these new batches of devices to further enhance our photodetector performances.

The 'dark currents' quoted in the original manuscript were measured (via Keithley SMU, detailed in Methods) by turning off the laser in the chip end-coupling setup in lab. However, there was still some ambient ceiling illumination (unable to remove) present. As shown in Fig. R1-7 above, in the new measurements, the I-V curves are quoted as 'laser off' (as highlighted by the red dashed circles in Fig. R1-7 lower panels), which is much higher than the true dark currents. In this time, the updated dark currents are separately measured in another professional enclosed probe station setup (C-6 Probe Station, Everbeing Int'l Corp., equipped with Keysight B1500A semiconductor device parameter analyzer, Keysight Technologies Inc.) that can totally block light illumination with higher precision in dark current measurements. We greatly appreciate the reviewer's instructive comment, and apologize for the impreciseness in dark current characterizations in previous measurements.

• The explicit dark currents data for the new devices are shown as Fig. R1-8a (corresponding to device in Fig. 3f left panel) and Fig. R1-8b (corresponding to Fig. 3f right panel) below. The dark current values at -2V operation bias voltage are 16.4 nA and 19.8 nA, for the devices shown in (main text) Figs. 3f left and 3f right panels, respectively.

The dark currents for the GaAs-SiN waveguide photodetector are shown in Fig. S33f (inset), with 45.6 nA at 5 V bias voltage.

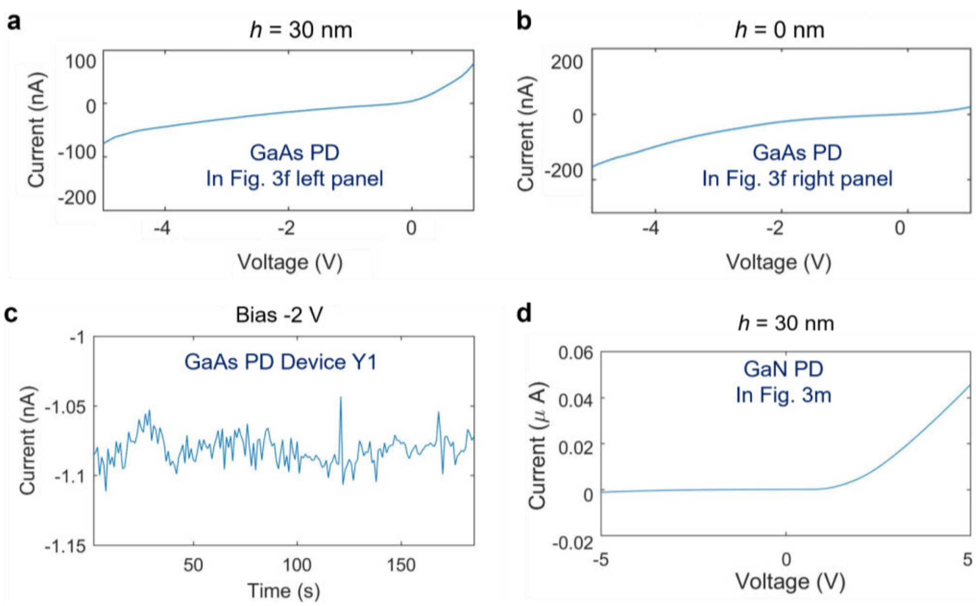

Fig. R1-8. Photodetector dark currents measured in fully enclosed probe station. (a) and (b) Device dark currents I-V curve for the photodetectors shown in main text Fig. 3f left panel (a) and right panel (b), respectively. (c) Measured photodetector dark currents as a function of time for another new photodetector device Y1 with ~35 μm × 50 μm effective device area size (shown in Fig. R1-9 below). (d) Measured dark currents for the GaN-based photodetector.

The photodetector dark current values are thus explicitly manifested in Table R1-8 below.

Table R1-8. Explicit dark currents for the vdW-integrated III-V nanomembrane photodetectors on SiN chip

Devices	GaAs PD h = 30 nm	GaAs PD h = 0 nm	GaAs PD Device Y1	GaAs PD Device Y2	GaN PD h = 30 nm
Dark current	16.4 nA	19.8 nA	1.2 nA	0.54 nA	45.6 nA
Device size	120 µm × 160 µm	120 µm × 160 µm	35 µm × 50 µm	25 µm × 30 µm	120 µm × 160 µm

Notes: PD: photodetector. h: air gap height. For GaAs-based photodetectors, the operation bias voltage is fixed at -2 V. For GaN-based photodetectors, dark current values at +5 V are listed. Device Y1 and Y2 have identical fixed air gap h = 30 nm. Measurement details are discussed in Methods.

(2) Device size is another factor largely impact photodetector dark current values. The III-V nanomembranes vdW-integrated photodetectors demonstrated in this manuscript have relatively big effective device area, leading to overall higher dark currents.

To validate this impact, additional GaAs-SiN photodetectors are fabricated with reduced effective device area (i.e. approximated by electrodes-covered III-V film size). Much lower device dark currents are observed, as shown in Table R1-8 above and Fig. R1-9 below.

Additional electron channeling contrast imaging (ECCI) further validated the high quality of our as grown ELO GaAs and 2DLT GaN nanomembranes with largely mitigated film defects, as shown in the updated Fig. S30 in Supplementary Note S16, with state-of-the-art dark current density (at the order of ~10^{-5}) for the GaAs photodetectors in this work. From this perspective, smaller device sizes are indeed more favorable for smaller dark currents. The photoresponsivity in devices Y1 (0.21 A/W) and Y2 (0.17 A/W) are only slightly reduced compared to the big-sized photodetectors shown in main text manuscript, because the length of the vdW-integrated GaAs nanomembranes is sufficient to absorb most of input optical power from the underlying SiN waveguides. Extended discussions are made in revised Supplementary Note S18.

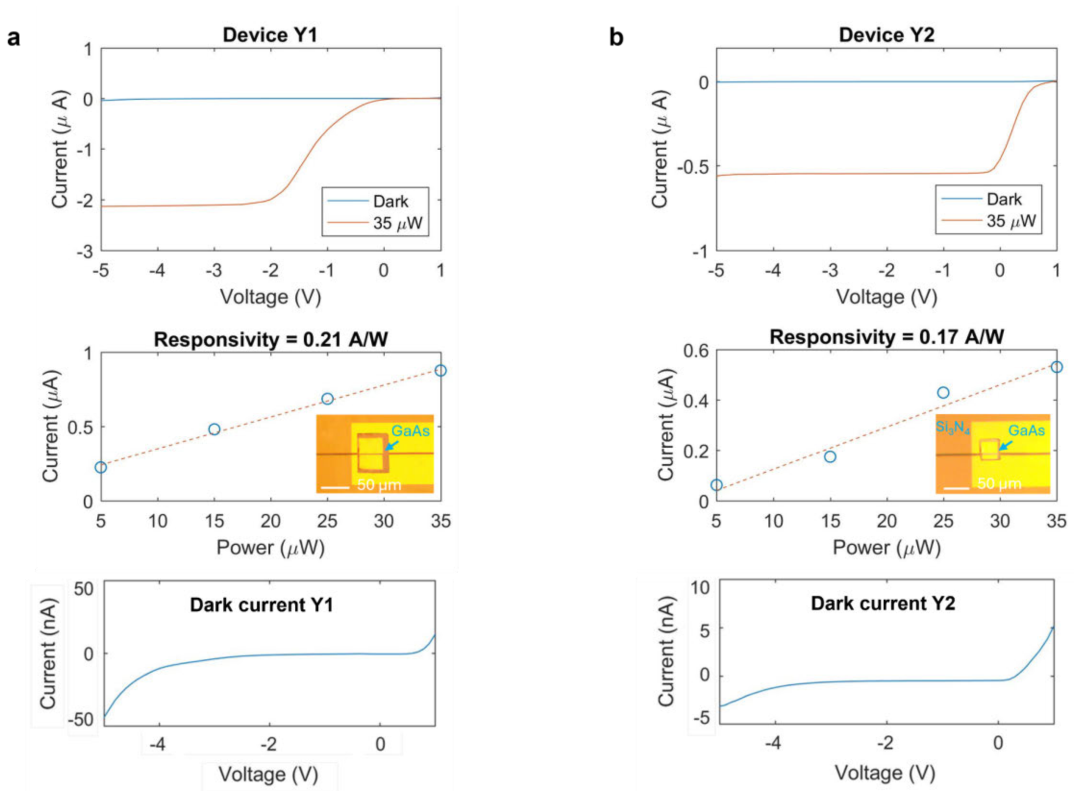

Fig. R-9. (a) and (b) GaAs-SiN waveguide photodetectors with reduced effective device size, measured at λ = 780 nm. Both the electrodes and patterned GaAs film sizes are reduced. Top panels: device I-V curves. Middle panels: photoresponsivity. Inset panels: device micrographs. Bottom panels: device dark currents.

Actions taken:

We have updated the remeasured accurate device dark currents to main text Figs. 3f, 3g, 3m, and 3n, accordingly.

The explicit photodetector dark current values are also quoted in revised Supplementary Note S18 (as highlighted in yellow, on Page 33 of the Supplementary Information). The impact of effective device area on dark currents and photoresponsivity performances is also discussed as well.

> Device dark currents are separately measured in an enclosed probe station (C-6 Probe Station, Everbeing Int'l Corp.) equipped with semiconductor device parameter analyzer (Keysight B1500A. The other *I-V* data are measured in the chip end-coupling setup fed with different laser sources (Methods, Fig. S33). The dark current for the GaN-SiN photodetector shown in main text Fig. 3m is 45.6 nA at 5V bias voltage. At -2 V bias voltage, the dark currents are 16.4 nA and 19.8 nA for the GaAs-SiN photodetectors shown in main text Fig. 3f left and 3f right panels, respectively. The photocurrent values are also largely related to the effective device sizes (under the case of sufficient light absorption from the underlying SiN waveguides). By further reducing the size of the electrode contacts and the patterned GaAs nanomembranes (Methods), much smaller dark currents are measured in smaller-sized photodetectors (with air gap h~30 nm): 1.2 nA and 0.54 nA for devices shown in Figs. S32d and S32e, respectively (at -2 V bias voltage), with slightly reduced photoresponsivity (with sufficient device length for light absorption).

The added steps to further enhance photodetector performance, including III-V film surface oxides removal and passivation, are given in revised Methods – Section 7 (as highlighted in yellow, shown below).

> μC/cm^2 dose, at 10 nA current) and PMMA resist development. GaAs at exposed areas (i.e. without top PMMA layer protection) were etched by mixed aqueous H_2SO_4 and H_2O_2 solutions. Surface native oxide removal (by diluted HCl solution) and passivation (via ammonium sulfide solution) are applied[90] to the GaAs nanomembranes before and after transfer. GaN nanomembranes were

The separate dark current measurement details are also discussed in revised Methods – Section 7 (as highlighted in yellow, shown below).

> loss of our home-made SiN chips evidently increased, calibrations were made to estimate the optical power fed into the GaN photodetectors[91] (Supplementary Note S18). The photodetector dark currents are separately measured in an enclosed probe station (C-6 Probe Station, Everbeing Int'l Corp., equipped with Keysight B1500A semiconductor device parameter analyzer, Keysight Technologies Inc.) with fully blocked ambient illumination. Fiber-coupled single-mode laser diodes (LT-405030-SM-FC, LT-450025-SM-FC, and LT-520045-SM-FC, by Laser Tree Inc.)

Comment 6:

6. The experiment of vertical stacking EO and MO nanomembranes is interesting. Could the authors provide more discussions on the potential application scenes of this?

Response 6:

We thank the reviewer for the instructive comment. The suggestion is well taken. We have added further discussions on revised manuscript and supplementary information.

(1) For current device examples shown in main text Fig. 4f-4k with vertically stacked single-crystalline CFO/BTO heterostructures, they can find favorable applications in multifunctional optical modulators, mode sorting, or non-reciprocal EO elements with eliminated back-reflections for photonic computing tasks (e.g. Ref: Nature Photonics 19, 54–62, 2025).

• The EO/MO nanomembranes-heterostructure enables electromagnetically reconfigurable micro-ring resonators with additional degrees of freedom for multifunctional modulations. Besides, by further adjusting device structure (to MZMs etc.), magnetically controlled mode-sorting, conversion, mode-division-multiplexing (MDM), and polarization rotation functions can be envisaged as well.

Current proof-of-concept device demonstrations in this work have shown EO modulation and MO isolation in a single device (as discussed for Figs. 4f-4k). Further, the non-reciprocal EO modulation enabled by the EO/MO stacking can also find its value in, e.g., on-chip laser generations (e.g. Ref: Nature 615, 411–417, 2023) and photonic in-memory computing (Ref: Nature Photonics 19, 54–62, 2025; Ref: Nature Electronics 3, 233, 2020), by applying the vdW-integration approach to modified Si and/or SiN photonics with modified device structure accordingly.

• Besides the vertical stacking of the functional 3D nanomembranes, these functional building blocks with optimal performance and crystal quality can be also laterally stitched to enable multiple disparate functional layers co-integrated on the same photonic chip for wider photonic applications, with much higher flexibility and degrees of freedom than current wafer-bonding-based approaches. For example, the laterally stitched GaAs and GaN nanomembranes atop a single SiN chip (discussed around main text Fig. 3) as a proof-of-concept instance.

(2) The value, impact, and further applications for the vdW-constructed 3D artificial heterostructures are further elaborated in revised Supplementary Notes S3 and S25, for multifunctional and high-performance 3D-integrated photonic applications (Ref: Nature 620, 78–85, 2023; Ref: Nature Electronics 7, 422–424, 2024), and versatile handy platform for studying fundamental physics and coupling between multidimensional nanomembranes beyond 2D to 3D/3D (e.g. Ref: Nature 626, 529-534, 2024. Ref: Nature Nanotechnology 20, 881-888, 2025), 3D/2D (Ref: Science 384, 312-317, 2024.Ref: Nature Communications 17, 3025, 2026) and beyond.

Actions taken:

Extended discussions are made to clarify the general potential application senses and highlight further impact for using this proposed single-crystalline freestanding 3D Lego building blocks for heterogeneous photonic integration and beyond, on Supplementary Note S3 (on Page 8).

> artificial heterostructure stacked on SiO_2 substrate (Fig. S10d), GaAs, BTO, GaN, and STO are colored as yellow, green, red, and blue in the first panel, respectively. We note that this artificial heterostructure stack of GaAs/BTO/GaN/STO is only an example to embody the capability of photonic vdW integration for constructing arbitrary desired high-quality functional optical layers on arbitrary substrate, which can find great value and broad applications in multifunctional hetero-integrated photonics[41-43] and 3D photonics integration[44,45]. A more specific demonstration of such stacked photonic system is beyond the scope of this work. A versatile platform is thus created for advancing nanomembranes technology[18,46-48], studying physical coupling[2,49,50], and prototyping exotic heterogeneous integrated photonic applications[15,25,51-53].

And in revised Supplementary Note S25 (as highlighted in yellow, on Page 38 of the Supplementary Information) for the specific application scenarios regarding the stacking of EO and MO layers.

> Nevertheless, fully integrated MO nonreciprocal devices can be envisaged in future work. The multifunctional electromagnetically reconfigurable microring demonstrated in this work can be further modified in device structure and design to enable magnetically mode conversion, polarization rotation, and non-reciprocal EO modulations for lasers[27,157], amplifiers[53], and in-memory computing[56,158] tasks. For

Comment 7:

Typo: Section 3, paragraph 3, first line, “Here we report…”

Response 7:

We are grateful for the reviewer’s considerate comment. We have corrected this typo accordingly (on Page 6 of the revised main text manuscript, as highlighted in yellow shown below).

> Here we report a viable alternative for BTO heterogeneous photonic integration[11], using freestanding single-crystalline BTO nanomembranes[37] with precisely controlled thickness and sizes from hundreds of square millimeters to 1-inch wafer scale (Supplementary Note 1). Atomic force microscopy (AFM) confirms the low root mean square (RMS) roughness below 0.2 nm for our pulsed laser deposition (PLD)-grown BTO film surface before layer lift-off (Fig. 2a). Despite

Responses to Referee 2:

Comment:

I co-reviewed this manuscript with one of the reviewers who provided the listed reports.

Response:

We sincerely thank the reviewer for the time and input with positive and constructive comments that greatly helped us to improve our manuscript. We have thus carefully revised our manuscript, accordingly, supplementing additional verification experiments and benchmarks to highlight the novelty and broad potential impact for the versatile vdW-integration platform for various photonic heterogeneous integration applications.

References for Reviewer 1 and Reviewer 2

1 Petraru, A., Schubert, J., Schmid, M., Trithaveesak, O. & Buchal, C. Integrated optical Mach Zehnder modulator based on polycrystalline BaTiO3. *Optics Letters* **28**, 2527-2529 (2003).

2 Abel, S. *et al.* Large Pockels effect in micro-and nanostructured barium titanate integrated on silicon. *Nature Materials* **18**, 42-47 (2019).

3 Alexander, K. *et al.* A manufacturable platform for photonic quantum computing. *Nature* **641**, 876-883 (2025).

4 Boyd, R. W. in *Nonlinear Optics* 511-523 (Springer, 2008).

5 Han, S. *et al.* High energy density in artificial heterostructures through relaxation time modulation. *Science* **384**, 312-317 (2024).

6 Mengxue, T. *et al.* Towards high quality transferred barium titanate ferroelectric hybrid integrated modulator on silicon. *Light: Advanced Manufacturing* **5**, 479-489 (2024).

7 Kim, H. *et al.* High-throughput manufacturing of epitaxial membranes from a single wafer by 2D materials-based layer transfer process. *Nature Nanotechnology* **18**, 464-470 (2023).

8 Bae, S.-H. *et al.* Graphene-assisted spontaneous relaxation towards dislocation-free heteroepitaxy. *Nature Nanotechnology* **15**, 272-276 (2020).

9 Cai, J. *et al.* Heterogeneously integrated lithium tantalate-on-silicon nitride modulators for high-speed communications. *Nature Communications* **17**, 3314 (2026).

10 Niels, M. *et al.* A high-speed heterogeneous lithium tantalate silicon photonics platform. *Nature Photonics* **20**, 225-231 (2026).

11 Sato, K., Okano, M. & Shoji, Y. Ultra-compact microring optical isolator using an aluminum-substituted cobalt ferrite thin film. *Optica* **11**, 889-895 (2024).

12 Serrano-Núñez, M. A., Shoji, Y. & Mizumoto, T. Small magnetless integrated optical isolator using a magnetized cobalt ferrite film. *IEICE Electronics Express* **19**, 20210500-20210500 (2022).

13 Xiang, C. *et al.* 3D integration enables ultralow-noise isolator-free lasers in silicon photonics. *Nature* **620**, 78-85 (2023).

14 Daudlin, S. *et al.* Three-dimensional photonic integration for ultra-low-energy, high-bandwidth interchip data links. *Nature Photonics* **19**, 502-509 (2025).

15 Wan, Y. *et al.* Integrating silicon photonics with complementary metal–oxide–semiconductor technologies. *Nature Reviews Electrical Engineering* **3**, 15-31 (2026).

16 Chelladurai, D. *et al.* Barium titanate and lithium niobate permittivity and Pockels coefficients from megahertz to sub-terahertz frequencies. *Nature Materials* **24**, 868-875 (2025).
17 Masubuchi, S. *et al.* Autonomous robotic searching and assembly of two-dimensional crystals to build van der Waals superlattices. *Nature Communications* **9**, 1413 (2018).
18 Chen, L. *et al.* Fully automatic transfer and measurement system for structural superlubric materials. *Nature Communications* **14**, 6323 (2023).
19 Nakatani, M. *et al.* Ready-to-transfer two-dimensional materials using tunable adhesive force tapes. *Nature Electronics* **7**, 119-130 (2024).
20 Zhao, Y. *et al.* Large-area transfer of two-dimensional materials free of cracks, contamination and wrinkles via controllable conformal contact. *Nature Communications* **13**, 4409 (2022).
21 Wen, Y., Chen, H., Wu, Z., Li, W. & Zhang, Y. Fabrication and photonic applications of Si-integrated LiNbO3 and BaTiO3 ferroelectric thin films. *APL Materials* **12**, 020601 (2024).
22 Zhu, D. *et al.* Integrated photonics on thin-film lithium niobate. *Advances in Optics and Photonics* **13**, 242-352 (2021).
23 Hu, Y. *et al.* Integrated electro-optics on thin-film lithium niobate. *Nature Reviews Physics* **7**, 237-254 (2025).
24 Baets, R. & Rahim, A. Heterogeneous integration in silicon photonics: opportunities and challenges: opinion. *Optical Materials Express* **13**, 3439-3444 (2023).
25 Kaur, P. *et al.* Hybrid and heterogeneous photonic integration. *APL Photonics* **6**, 061102 (2021).
26 Ramirez, J. M. *et al.* III-V-on-Silicon Integration: From Hybrid Devices to Heterogeneous Photonic Integrated Circuits. *IEEE Journal of Selected Topics in Quantum Electronics* **26**, 1-13 (2020).
27 Ortmann, J. E. *et al.* Ultra-Low-Power Tuning in Hybrid Barium Titanate–Silicon Nitride Electro-optic Devices on Silicon. *ACS Photonics* **6**, 2677-2684 (2019).
28 Eltes, F. *et al.* A BaTiO3-Based Electro-Optic Pockels Modulator Monolithically Integrated on an Advanced Silicon Photonics Platform. *J. Lightwave Technol.* **37**, 1456-1462 (2019).
29 Eltes, F. *et al.* Low-loss BaTiO3–Si waveguides for nonlinear integrated photonics. *ACS Photonics* **3**, 1698-1703 (2016).
30 Xiong, C. *et al.* Active silicon integrated nanophotonics: ferroelectric BaTiO3 devices. *Nano Letters* **14**, 1419-1425 (2014).
31 Eltes, F. *et al.* An integrated optical modulator operating at cryogenic temperatures. *Nature Materials* **19**, 1164-1168 (2020).
32 Kim, G. I., Yim, J. & Bahl, G. J. a. p. a. Low loss monolithic barium titanate on insulator integrated photonics with intrinsic quality factor> 1 million. (2025).
33 Jacob, B. *et al.* Surface Passivation of III–V GaAs Nanopillars by Low-Frequency Plasma Deposition of Silicon Nitride for Active Nanophotonic Devices. *ACS Applied Electronic Materials* **4**, 3399-3410 (2022).
34 Karvounis, A., Timpu, F., Vogler-Neuling, V. V., Savo, R. & Grange, R. BaTiO3: Barium Titanate Nanostructures and Thin Films for Photonics *Advanced Optical Materials* **8**, 2070094 (2020).

Responses to Referee 3:

Comment:

The paper presents a scheme to heterogeneously integrate multiple crystalline membranes onto silicon and silicon nitride photonics for a variety of applications which include high-speed modulation, non-reciprocal magneto-optic isolators, and photodetection. This comprises of variety of different epitaxially grown crystalline materials on different substrates: thin-film barium titanate (BTO), cobalt ferrite (CFO) and yttrium iron garnet (YIG), gallium nitride (GaN) and gallium arsenide (GaAs). While all these materials have previously been heterogeneously integrated onto Si and SiN photonic circuits, the real advance here is the nature of remote epitaxy demonstrated where each crystalline thin-film can be easily separated from its host substrate with relative ease using techniques of epitaxial lift-off (ELO) and 2D-materials-assisted layer transfer (2D-LT). In many cases, the substrate removal process after hetero-integration via bonding (i.e. van der Waals) is a real challenge and detrimental to the core bond itself. There is no real substitute to crystalline thin-film quality from growth on native substrate. Direct growth on photonic platforms results in poor amorphous or at best poly-crystalline films with low yield and performance compared to their crystalline counterparts.

While this work focused on remote-epitaxial transfer of thin-films for photonic applications is of note, the manuscript can benefit from the below feedback.

Response:

We sincerely thank the reviewer for the careful assessment of our manuscript with overall positive comments and very constructive suggestions.

The heterogeneous integration of thin-film functional materials to photonic platforms with optimal single-crystallinity and the effective native bulk parent substrates removal is indeed vital for photonics and optoelectronics communities to enable advanced and multifunctional integrated applications. We have carefully revised our manuscript accordingly, supplementing additional experiments validating the high-quality of the freestanding 3D nanomembranes and detailed photodetector dark current analysis. Comprehensive benchmarks are also added to further highlight the novelty and technical advancements of this work. The detailed revisions and responses are as follows.

Comment 1:

1. One of the main claims of this paper is the reduction of defect density in this approach of remote epitaxy transfer compared to other methods. It would be useful to characterize both local and global defect density of all these thin-film materials with sacrificial layers compared to growth on native substrates without the sacrificial layers. In other words, what is the compromise here in terms of defect density and other material properties?

Response 1:

We thank the reviewer for the instructive comment. We have performed additional experiments and material characterizations accordingly, to illustrate superiority on the defect reduction and single-crystal quality control of the proposed photonic van der Waals (vdW) approach for 2DLT and ELO freestanding 3D nanomembranes against other hetero-integration methods.

(1) Comparative high-resolution scanning transmission electron microscopy (HR STEM) measurements are added accordingly to characterize the local defects of (i) BTO grown with $Sr_3Al_2O_6$ (SAO) sacrificial layer (i.e. as-grown BTO/SAO/STO), (ii) BTO directly grown on parent $SrTiO_3$ (STO) substrate (i.e. as-grown BTO/STO), and (iii) transferred single-crystalline BTO film on target SiO_2 substrate (i.e. vdW-integrated BTO/SiO_2/Si).

(1.1) The defect density of BTO films grown on sacrificial layer atop STO parent substrate (i.e. as-grown BTO/SAO/STO).

• For local defects of grown BTO/SAO/STO, high BTO crystallinity with minimal local crystallization defects are confirmed by STEM, as shown in Fig. R3-1 below (added to Fig. S25 in Supplementary Note S14).

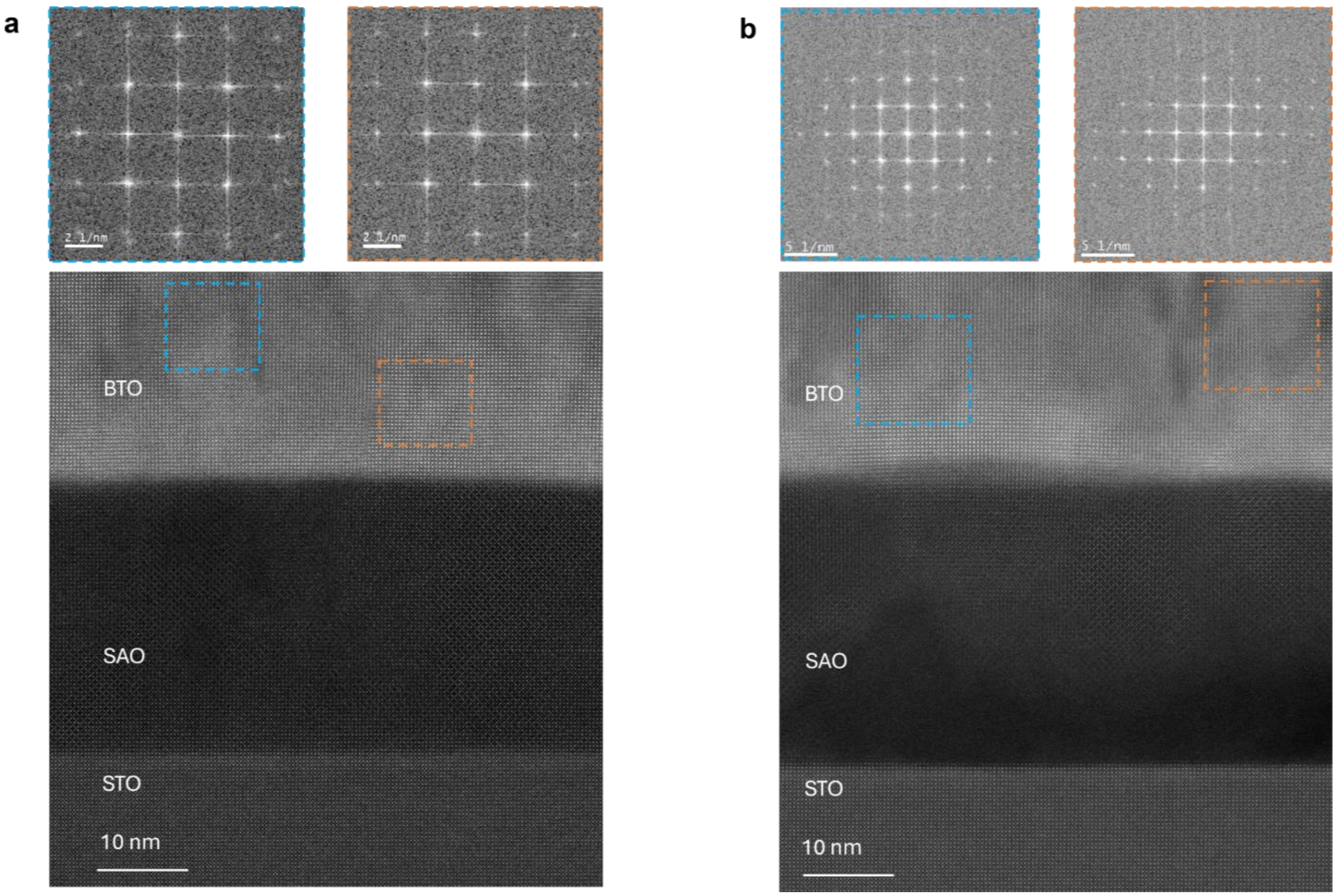

Fig. R3-1. High-resolution scanning transmission electron microscopy (HR-STEM) of two as grown BTO/SAO/STO samples. The SAO sacrificial layer was already degraded due to electron beam and exposure to ambient oxygen and humidity during TEM sample transfer and storage. Ununiform brightness contrast is due to nonideal FIB thinning process for TEM sample preparations.

During imaging, we found that (as expected) the SAO sacrificial layer is very sensitive to both ambient humidity and oxygen. Specifically, the focused electron-beams from very high-magnification STEM imaging also irreversibly damage the SAO layer, making the SAO lattice fringes disappearing rapidly during zoomed-in scanning. This leads to the dark regions in Fig. R3-1 SAO area, despite our multiple trails on quick focusing and imaging. Nevertheless, high crystal quality and low local defects can still be confirmed (Fig. R3-1a), where the ununiform brightness contrast is due to the nonideal FIB thinning process in TEM sample preparation.

Specifically, we confirmed the *a*-axis-domain BTO (i.e. crystallographic *c*-axis parallel to film plane), with ferroelectric domain rotations occasionally taking place over long regions (Fig. R3-1a), as two equivalent possible *a*-axis-domain orientations can co-exist (illustrated in the inset panel of Fig. S15a in Supplementary Note S8), which is universal for the desired *c*-axis-in-plane BTO essential for integrated EO applications (Ref: Nature Materials 24, 868–875 (2025). Ref: Nature Materials 18, 42-47, 2019). The low BTO defect density can be also evidenced by Fig. R3-3 (shown later) and Supplementary Fig. S38c in Supplementary Note S26.

• For the global defects of as-grown BTO/SAO/STO, besides the detailed XRD (Figs. 1f, 2b), RSM (Fig. 2c, and Supplementary Figs. S8a, S11), and EBSD characterizations (Fig. 1g, Fig. S11) elaborated in manuscript main text and Supplementary Information, electron channeling contrast imaging (ECCI) is further performed to evaluate the global defect (threading dislocation density) of BTO.

As shown in Fig. R3-2 above, ECCI measurements were performed at multiple BTO film locations, where the threading dislocation defects are marked out in blue dashed circles in Fig. R3-2a. An average threading dislocation density around 1.35 $\times 10^7 \sim 4 \times 10^7$ is confirmed for the as-grown BTO film (Fig. R3-2, added as Fig. S26 in Supplementary Note S14), validating low global defect density of our high-quality BTO nanomembranes.

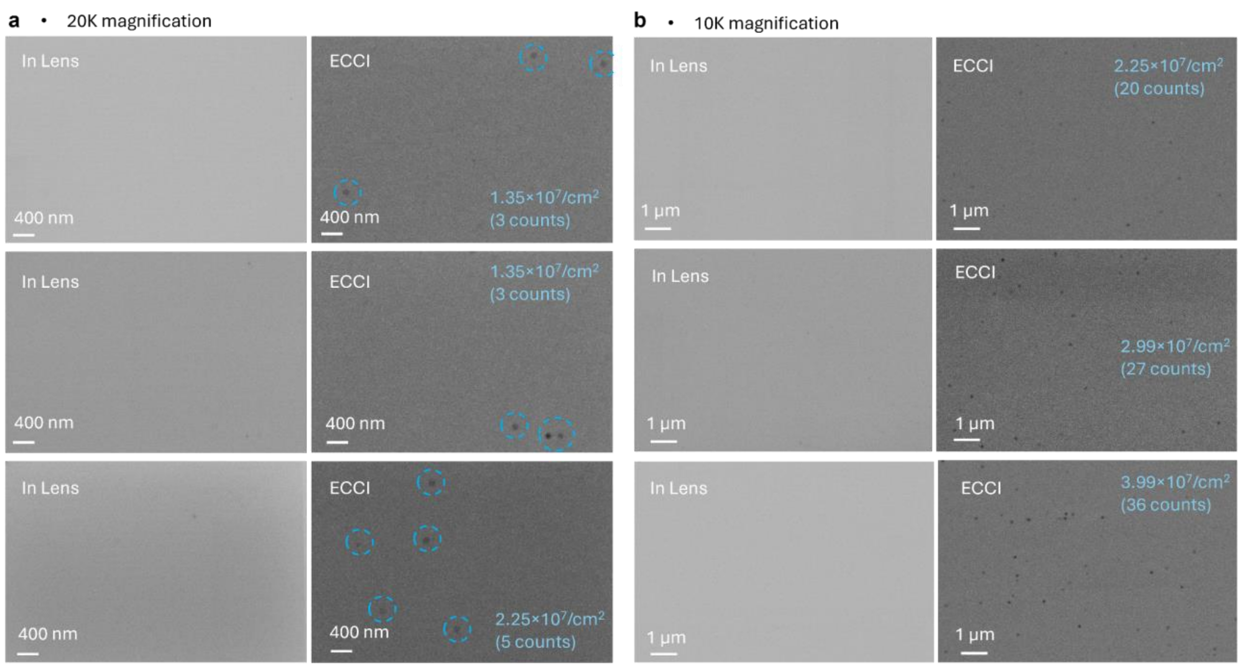

Fig. R3-2. Electron channeling contrast imaging (ECCI) for as grown BTO/SAO/STO sample with (a) 20 k and (b) 10 k magnification, respectively, showing low BTO film threading dislocation density.

(1.2) For the local defect density of BTO/STO (i.e. BTO directly grown on STO substrate without SAO sacrificial layer), additional HR-STEM is also performed to compare its local defects with BTO grown with the sacrificial layer (i.e. BTO/SAO/STO) to fulfill revision.

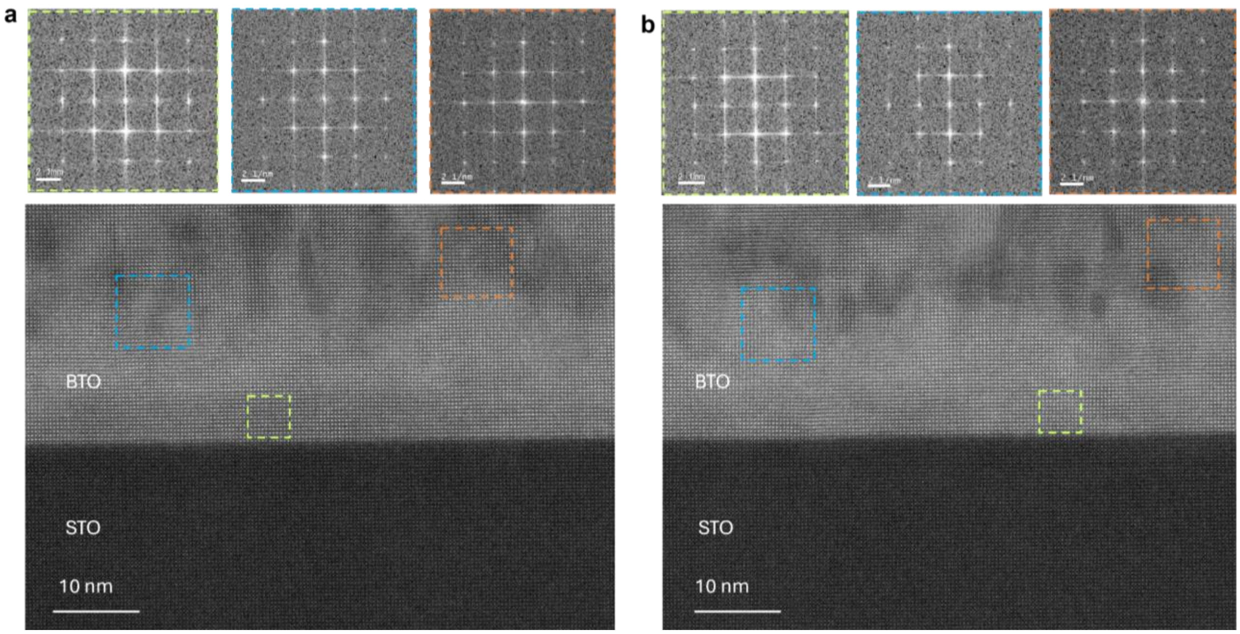

Fig. R3-3. (a) and (b) HR-STEM images of BTO/STO samples, where the ununiform brightness contrast is due to nonideal FIB sample polishing. Top panels: TEM fast Fourier transform (FFT) diagrams at corresponding regions (marked with colored dashed rectangles).

High-quality crystalline BTO is also confirmed for the BTO/STO sample. However, local TEM fast Fourier transform (FFT) diagrams indicate *c*-axis-domain BTO (i.e. crystal c-axis perpendicular to film plane) thin layers were formed atop STO during initial growths, which agrees with some of prior reports (Ref: Nature Materials 18, 42-47, 2019). In contrast, BTO grown with SAO sacrificial layer with engineered initial tensile strain promotes pure *a*-axis-domain BTO (required for chip-integrate EO applications) growth. A deeper study of the growth and ferroelectric domain forming at different substrates can be an interesting and fundamental open question, but will pass beyond the scope of this work.

Further global defect density check was not conducted, because this BTO/STO comparison sample already shows different crystal orientations than the required *a*-axis-domain BTO realized in BTO/SAO/STO sample, and our previous recipes were optimized based on BTO grown with SAO sacrificial layer instead of directly on STO. Specifically, the BTO directly grown on parent substrate is comparatively less valuable, because so far, this BTO/STO is unable to be used in any integrated photonic applications due to the almost same optical refractive index between BTO and STO, and the difficulty in removing the bulk STO substrate from BTO layer.

(1.3) For the local defects of BTO nanomembrane (after transfer), HR-STEM is performed for an instance sample with vdW-integrated BTO film atop SiO_2/Si substrate, as shown in Fig. R3-4 below (added as Fig. S24 in revised Supplementary Note S14). Ultrahigh BTO crystal quality with minimal local defects is confirmed (Fig. R3-4), which is inaccessible via direct BTO heteroepitaxy due to the radically mismatched lattice parameters as heavily discussed in previous references[16,34-38].

In summary, HR-STEM confirmed the low local defect density for transferred BTO and as-grown BTO/SAO/STO samples. ECCI characterizations also confirmed the low global defect density for as-grown BTO/SAO/STO samples, with average threading dislocation density around $1.35 \times 10^7 \sim 4 \times 10^7$. The SAO sacrificial layer and engineered interfacial tensile strain (Methods) enable the *a*-axis-domain BTO epilayer critical for integrated photonic applications (detailed in Response 8 on Page 69 of this Response Letter), if comparing BTO/SAO/STO to BTO/STO. More importantly, the SAO sacrificial layer enables the delamination of freestanding BTO nanomembranes for vdW integration on arbitrary photonic substrates with optimal BTO crystal quality.

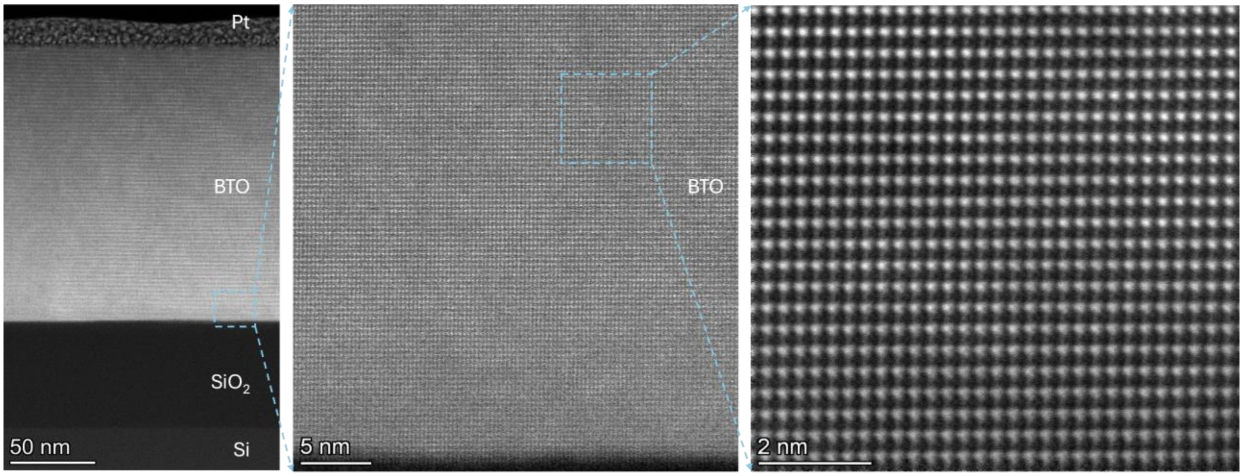

Fig. R3-4. High-resolution scanning transmission electron microscopy (HR-STEM) for the cross-section of the single-crystalline freestanding BTO film vdW-integrated to SiO_2/Si substrate. This figure is added to revised Supplementary Note S14 as Fig. S24.

(2) For the defect densities of GaN and GaAs films, the effectiveness of defects reduction is validated by additional benchmark experiments and electron channeling contrast imaging (ECCI) characterizations.

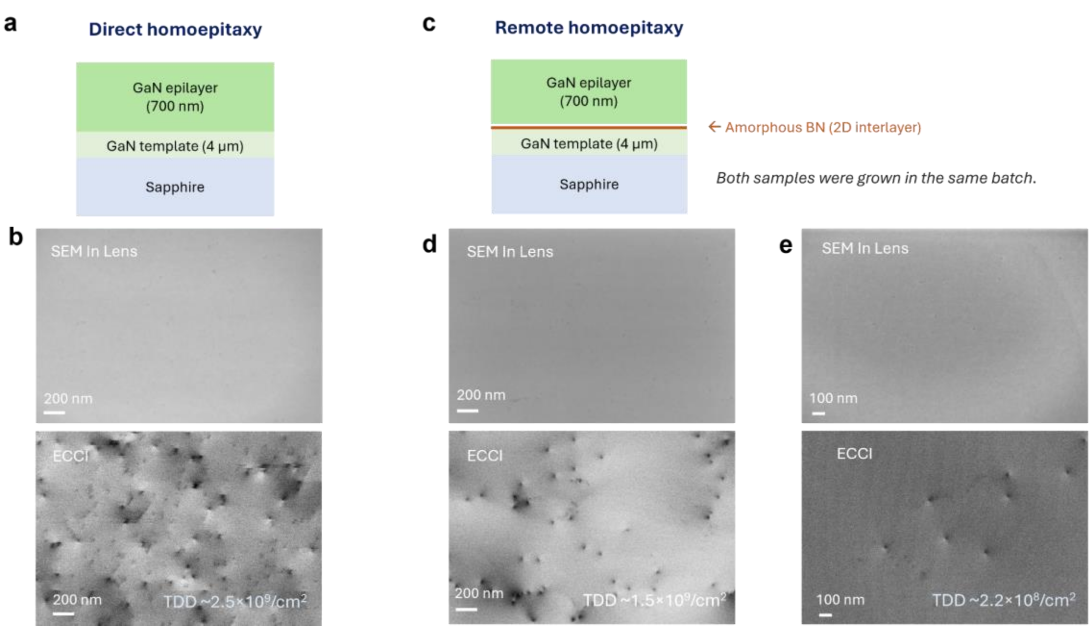

Fig. R3-5. Benchmark for remote epitaxial GaN films on defects reduction. (a) Direct GaN epitaxy. (b) SEM (top) and electron channeling contrast imaging (ECCI, bottom panel) showing threading dislocation density (TDD). (c) GaN remote epitaxy with 2D interlayer. (d) SEM and ECCI of the remote epitaxial GaN grown together with the sample in (b) with reduced TDD. (e) SEM and ECCI of another optimized remote epitaxial GaN film.

(2.1) For the defect reduction and defect density of remote epitaxial GaN films compared to conventional direct epitaxy, ECCI measurements were conducted for two samples quickly grown together in sample batch via MBE: direct GaN homoepitaxy (Fig. R3-5a), and GaN remote epitaxy on boron nitride (BN)-covered template (shown in Fig. R3-5c above).

As threading dislocations (TD) are most commonly seen and dominant defects in epitaxial nitride films (such as GaN), ECCI will be a suitable tool for evaluating the threading dislocation density (TDD). As shown in Figs. R3-5b and Fig. R3-5d, remote epitaxial GaN shows largely reduced TDD[8] compared to conventional epitaxial GaN, thanks to the spontaneous relaxation on 2D-covered interfaces (Ref: Nature Nanotechnology 15, 272–276, 2020). The average TDD can be further suppressed to the order of $\sim 10^8/cm^2$ for carefully optimized 2DLT GaN films (shown as Fig. R3-5e above).

For other defect characterizations, such as XRD and STEM for the III-V nanomembranes, they are discussed in Supplementary Notes S2, S16, and S17.

(2.2) For the global defect density of GaAs nanomembranes, additional ECCI measurements are performed for the as-grown GaAs films (Fig. R3-6), in which negligible threading dislocation density (TDD) is confirmed, validating the high-quality of our GaAs films.

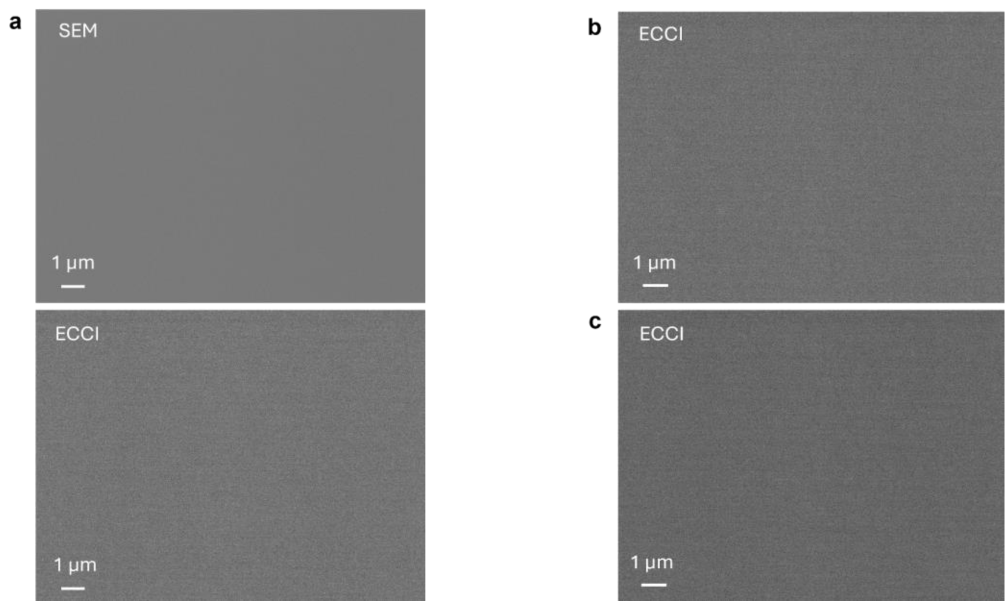

Fig. R3-6. (a) Top panel: second electron SEM of as grown GaAs film (sample structure illustrated as Fig. S3a in Supplementary Note S1). Bottom panel: Corresponding ECCI showing negligible threading dislocation defects. (b) and (c) ECCI of as-grown GaAs films at different sample locations.

(3) For the comparison of the defects and crystal quality of CFO films to conventional methods, a benchmark figure is summarized as Fig. R3-7 below.

Due to the disparate lattice mismatch between CFO and Si, previous methods relying on direct CFO heteroepitaxy show poor crystal quality (amorphous to polycrystalline) with large optical loss from film defects scattering (Figs. R3-7a, R3-7b). In contrast, our vdW-integrated CFO nanomembranes show significantly improved crystal quality (Figs. 1f, 1g, and Supplementary Fig. S8b) with much lower defects and scattering loss (Fig. R3-7c).

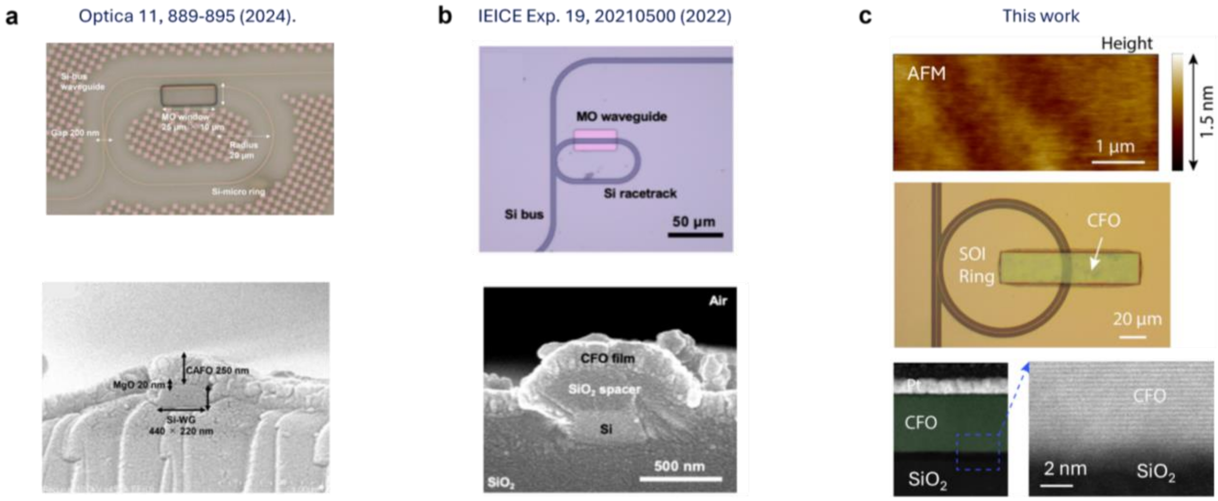

Fig. R3-7. Comparison of CFO quality to previous work. (a) and (b) Sputtered CAFO (Ref: Optica 11, 889-895, 2024) and CFO (Ref: IEICE Exp. 19, 20210500, 2022) respectively, with poor crystal quality and strong scattering loss from CFO film defects. (c) vdW-integrated single-crystalline CFO film in this work with high-quality and uniform smooth film morphology. Top panels: device optical micrographs. Bottom panels: cross-sectional SEM or TEM.

(4) Besides the innovation points of high-quality nanomembranes growth and transfer, additional novelty points regarding device implementations, performance advancements, and further impacts are summarized in revised Supplementary Note S27 and the later Response 8 on Page 63 of this response letter.

Actions taken:

HR-STEM results on the transferred BTO film are added to revised Supplementary Note S14 (on Page 26 of Supplementary Information), validating the high-quality and low defects of vdW-integrated BTO films. HR-TEM on the as-grown BTO/SAO/STO samples, BTO ECCI defect characterizations with extended discussions are also added to revised Supplementary Note S14.

High-resolution scanning transmission electron microscopy (HR TEM) is performed to validate the single-crystallinity of the vdW-integrated BTO nanomembranes with minimal crystallization defects (Fig. S24, Methods). The introduction of SAO sacrificial layer enables the delamination of freestanding BTO nanomembranes for boundless heterogeneous photonic integration on arbitrary substrates, which can achieve previously inaccessible crystal quality with well-controlled BTO crystallographic orientations via conventional heteroepitaxial approaches[31,35,36,54,80,91].

HR TEM also confirmed the high crystal quality of the as-grown BTO/SAO/STO samples before transfer with desired a-axis-domains vital for integrated EO applications (Fig. S25). The rapid degradation of SAO layer (sensitive to humidity and oxygen) under zoomed-in electron beams during TEM was observed, followed by partially vanished SAO layer lattice fringes after repeated focus adjustment and imaging. We also further characterized the threading dislocation density (TDD) of the as grown BTO film (i.e. BTO/SAO/STO sample) via electron channeling contrast imaging (ECCI), confirming low TDD around $1.35 \times 10^7 \sim 4 \times 10^7$ (Fig. S26, where the threading dislocation defects are marked out in blue dashed circles for Fig. S26a only) indicating high-quality BTO nanomembranes.

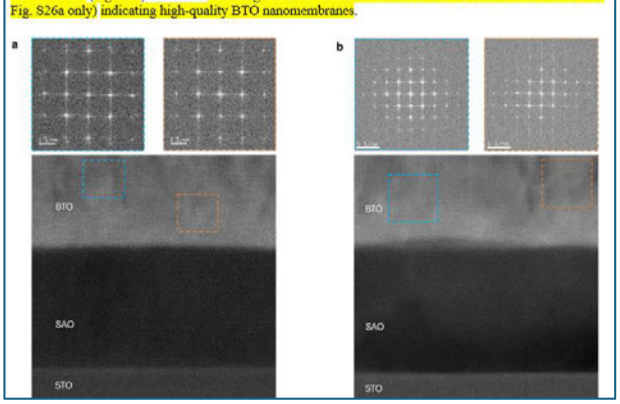

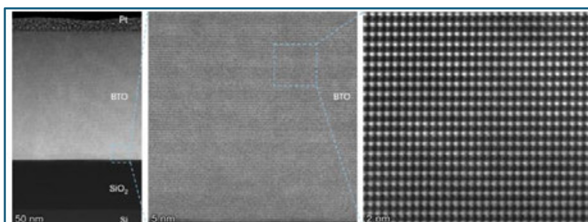

Figure S24. High-resolution scanning transmission electron microscopy (HR-STEM) for the cross-section of the single-crystalline freestanding BTO film vdW-integrated to SiO_2/Si substrate.

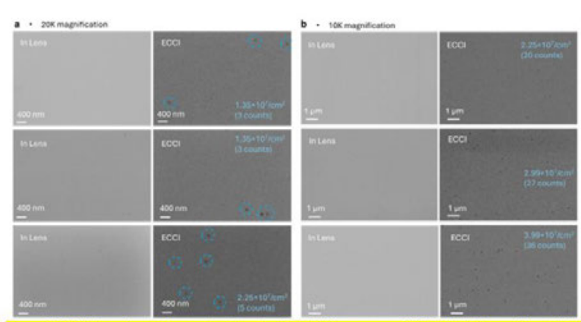

Figure S26. Electron channeling contrast imaging (ECCI) for as grown BTO/SAO/STO samples with (a)

Discussions on benchmark experiments for remote epitaxial GaN with defect reduction are added to revised Supplementary S16 (and Fig. S30), as shown below.

The impact of defects reduction through remote epitaxial GaN (Figs. S30a, S30b) is further compared to conventional direct epitaxial GaN (Figs. S30c, S30d), showing reduced threading dislocation density (TDD) via electron channeling contrast imaging (ECCI) characterizations thanks to the spontaneous relaxation on 2D-covered interfaces[13]. The two samples (Figs. S30b, S30d) are grown together in same batch via MBE (Methods) for a quick benchmark, where the TDD can be further suppressed for carefully optimized 2DLT GaN nanomembranes (Figs. S30e)[3,11].

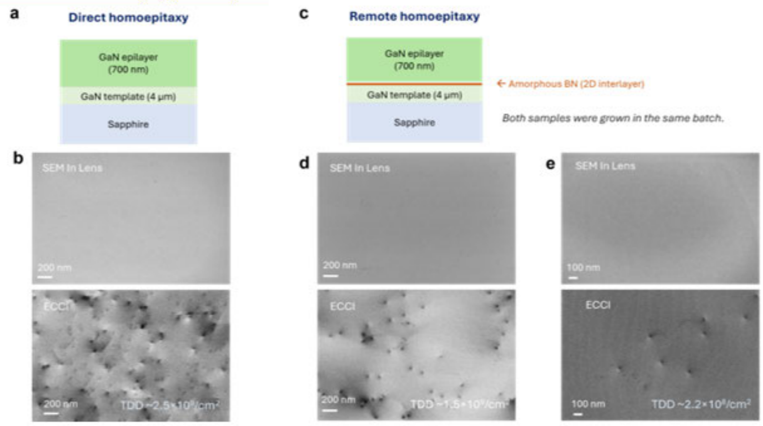

Figure S30. Comparison of direct- and remote epitaxial-GaN films defects density. (a) Direct GaN epitaxy. (b) SEM (top) and electron channeling contrast imaging (ECCI, bottom panel) showing threading dislocation density (TDD). (c) GaN remote epitaxy with 2D interlayer. (d) SEM and ECCI of the remote epitaxial GaN with reduced TDD. (e) SEM and ECCI of another optimized remote epitaxial GaN film.

Discussions regarding the enhanced crystal quality of CFO via vdW integration with reduced defects and scattering loss are also added to revised Supplementary Note S24 (on Page 37 of the Supplementary Information).

as well in Table S3. Thanks to the giant CFO Faraday rotation coefficient, a big NRPS can be realized in an ultracompact length L_{MO} of about 26 μm. The optimal single-crystalline nanomembrane quality also enhances magnetic response and reduces optical losses from defects scattering and imperfect CFO crystal quality found in previous works[21,137,139], circumventing the prior obstacles of lattice mismatching for defective heteroepitaxial CFO layer by applying photonic vdW integration[25].

Comment 2:

2. For the integrated GaAs and GaN detectors, these thin-films were bonded to SiN for demonstration purposes only, whereas they were placed/compressed on top of a metallic film (i.e. Au) for the actual devices where this metal served as the back contact. This invalidates the 'van der Waals integration' claim for the photodetectors. As I understand, top-side contacts are feasible for these HI devices without the air-gap. Would the lack of an air-gap improve the coupling performance or overall responsivity of these detectors?

Response 2:

We thank the reviewer for raising this comment. We have performed supplementary simulations to illustrate the impact of air gap h on the optical coupling and absorption between the III-V nanomembranes and SiN waveguides. New benchmark samples (with air gap $h = 30$ nm, and without air gap) were also measured to validate its overall impact on photodetector responsivity.

(1) For the case III-V nanomembranes transferred directly atop metal (i.e. Au back electrodes), it is still a valid van der Waals (vdW) integration, as the interaction between the transferred III-V film and underlying metal (and SiN substrate) is still governed by vdW interactions (Ref: Nature 567, 323–333, 2019).

As shown in main text Fig. 3j, the air gap h only exists between the III-V nanomembranes and the SiN waveguide (with a width ~ 1 μm). The GaAs and GaN films are still in valid and solid contact with the Au back electrodes without any gap, enabling robust vdW integration to the photonic chip for photodetectors. Previous research also validates effective vdW integration between semiconductor and metal layers[39-41] (e.g. Ref: Nature Nanotechnology 18, 471–478, 2023. Ref: Nature Communications 14, 1014, 2023). The big contact area between the GaAs or GaN nanomembranes to the Au back electrodes (suspended atop SiN waveguides with air gap h) and the remaining SiN chip substrate facilitates robust film bonding and light coupling for the heterogeneous integrated photodetectors.

(2) We have further studied the impact of air gap h on the optical coupling via FDTD numerical simulations.

We initially applied a 30 nm air gap h to reduce the optical reflection (at the abrupt index-changed region along the III-V film edges), and simultaneously enable sufficient light harvesting from the underneath SiN waveguide for photodetection. This 30 nm gap exists primarily because the height difference between the Au back electrodes (~30 nm in thickness) and the SiN waveguides.

As the III-V nanomembranes (GaAs or GaN) used here have higher optical refractive index than the underlying SiN waveguide, evanescent optical coupling can still take place with the presence of small air gap h. The value of h will impact the coupling length between the III-V films and SiN waveguide to realize a given light absorption rate (e.g. 99%). The simulation results are summarized as Table R3-1 below.

Table R3-1. Impact of air gap h on the optical coupling between III-V layers and SiN waveguide.

GaAs-SiN • Wavelength λ = 780 nm, GaAs propagation length: 20 μm

Gap	h = 0 nm	h = 20 nm	h = 40 nm	h = 60 nm	h = 80 nm	h = 100 nm
Optical field |E|						
T	3.8×10^{-5}	1.9×10^{-5}	1.5×10^{-5}	1.4×10^{-4}	3.6×10^{-3}	0.028

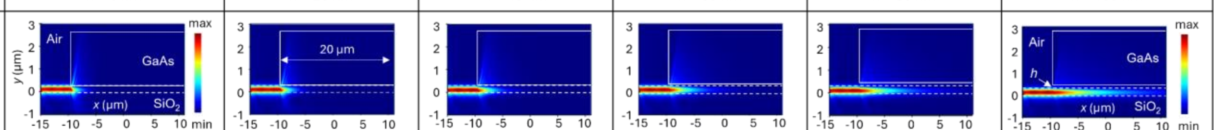

GaN-SiN • Wavelength λ = 350 nm, GaN propagation length: 20 μm

Gap	h = 0 nm	h = 20 nm	h = 40 nm	h = 60 nm	h = 80 nm	h = 100 nm
Optical field |E|						
T	1.1×10^{-7}	1.0×10^{-3}	0.092	0.51	0.81	0.93

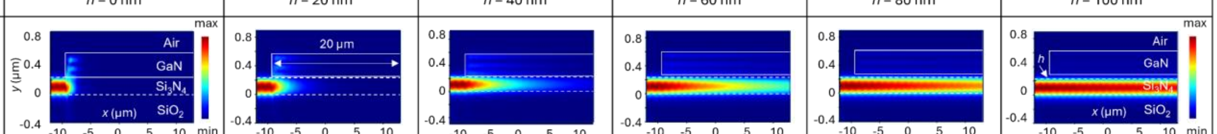

Notes: λ: light wavelength. SiN: silicon nitride (Si_3N_4). T: optical transmission rate of the III-V/SiN hybrid waveguide after a 20 μm propagation length. Literature GaAs and GaN complex refractive index values are used in the FDTD simulations. The III-V nanomembranes are vdW integrated to Au back electrodes and get suspended atop the SiN waveguides (shown in main text Fig. 3j). Smaller T denotes higher absorption rate of the injected optical power by the III-V photodetection layer.

As illustrated in Table R3-1, by increasing air gap h from 0 nm to 100 nm, the optical transmission rates (injecting fundamental TE_{00} mode) of the GaAs-covered SiN waveguides increase from 3.8×10^{-5} to 2.8% (with a 20 μm propagation length), validating that majority of the injected light power are effectively coupled to and absorbed by the GaAs nanomembranes for photodetection.

In the case of h = 30 nm in the initial batch of devices, the theoretical light absorption rate is greater than 99.9% for a 20 μm propagation length. The impact of h on the coupling between GaN film and SiN waveguides are shown in Table R3-1 lower panels, similarly. For h = 30 nm, after a 20 μm propagation in the GaN-SiN hybrid waveguide, over 99% optical power is absorbed by the GaN layer despite the presence of air gap h.

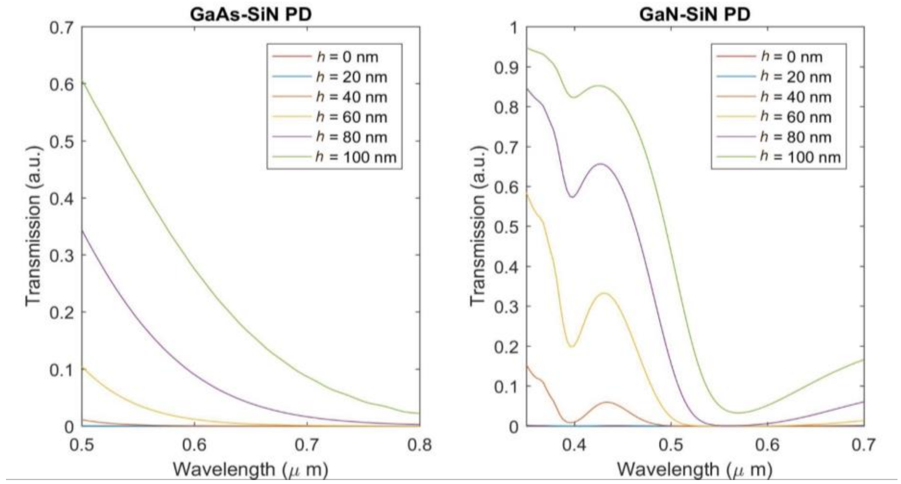

Fig. R3-8. Simulated optical transmission rate of the GaAs-SiN (left panel) and GaN-SiN hybrid waveguide (right panel) after a 20 μm propagation length under different air gap values h.

The simulated optical transmission rates of the III-V/SiN hybrid waveguides (via Lumerical FDTD solutions) under different air gap values h are summarized as Fig. R3-8 above. In our original manuscript, these proof-of-principle photodetectors have device length over 100 μm, thus guaranteeing sufficient light harvesting from the SiN waveguides.

(3) Benchmark experiments are further performed: comparing the GaAs vdW-integrated photodetectors with air gap ($h = 30$ nm) and without air gap ($h = 0$ nm).

In initial sample batches, the 30 nm-height Au electrodes deposited on the SiN chip suspended the freestanding GaAs and GaN nanomembranes atop the SiN waveguide (cross-sectional structure shown as Fig. R3-9a below). To realize $h = 0$ nm with direct contact between III-V layer and SiN waveguide, the electrode regions were pre-etched together with the waveguides, followed by the deposition and lift-off of a 220 nm-height thick Au electrodes (same height as the SiN device layer), as shown in Figs R3-9b (structure schematics) and Fig.R3-9c (optical images of fabricated chips).

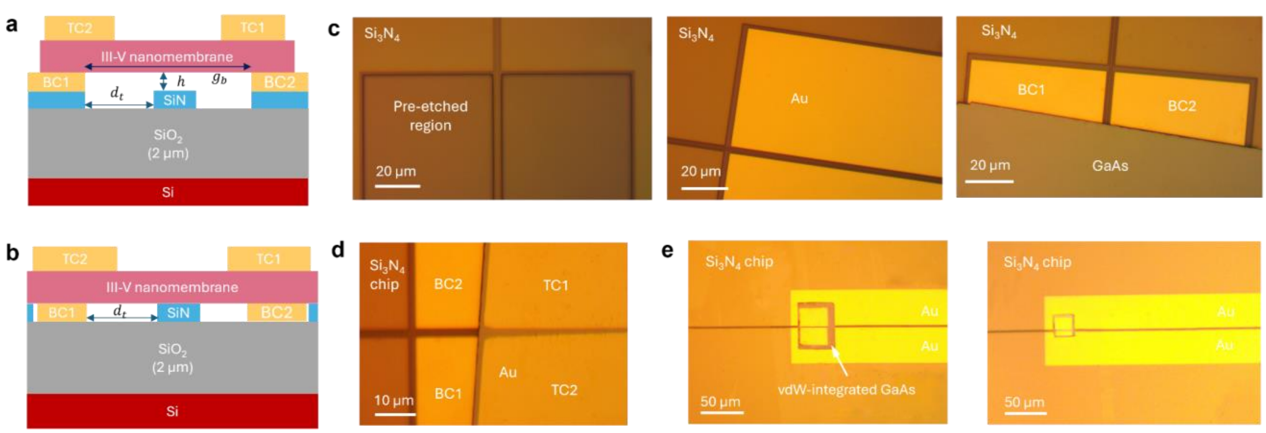

Fig. R3-9 (a) vdW-integrated III-V nanomembranes on SiN chip with air gap h between GaAs (over 2 μm thickness) and GaN (~ 300 nm thickness) film and SiN waveguide (with 1 μm waveguide width, and $d_t =$ 3 μm etching trenches). (b) Modified device structure with buried electrodes to realize direct contact between III-V nanomembranes and underlying SiN chips (i.e. $h = 0$ nm). (c) Optical micrographs of newly fabricated SiN chips with device structures shown as panel (b), from electrodes patterning (after EBL and PMMA develop, left panel), Au lift-off (middle panel), and GaAs transfer (right panel). (d) Optical micrograph for the new GaAs-SiN photodetector eliminating air gap ($h = 0$ nm). (e) Newly fabricated GaAs-SiN photodetector devices with reduced device sizes ($h = 30$ nm), as discussed later.

The device I-V curves and photoresponsivity are compared: with air gap $h = 30$ nm (Fig. R3-10a) and without gap ($h = 0$ nm, Figs. R3-10b, R3-10d), where both devices have similar device size (i.e. the area of GaAs film covered with top electrodes) of around ~120 µm × 160 µm. Similar levels of photocurrents and I-V curves are observed, where the differences in current level between Figs. R3-10a and R3-10b are mainly impacted by nanomembrane transfer, device fabrication and electrical contacts, as the 160 µm device length would be sufficient for light absorption of GaAs layer from the underlying SiN waveguide (as Table R3-1 discussed above).

We have further adopted native oxide removal (via diluted HCl) and surface passivation (via ammonium sulfide solution, Ref: ACS Applied Electronic Materials 4, 3399-3410, 2022; Ref: Nature Photonics 19, 1178-1188, 2025) to further enhance the performance of these new batches of GaAs-vdW-integrated photodetectors. The photoresponsivity (at 780 nm wavelength) values are found to be almost identical (R3-10c): 0.29 A/W for device with air gap $h = 30$ nm, and 0.3 A/W for device without gap $h = 0$ nm, give this case of sufficient device length for light absorption.

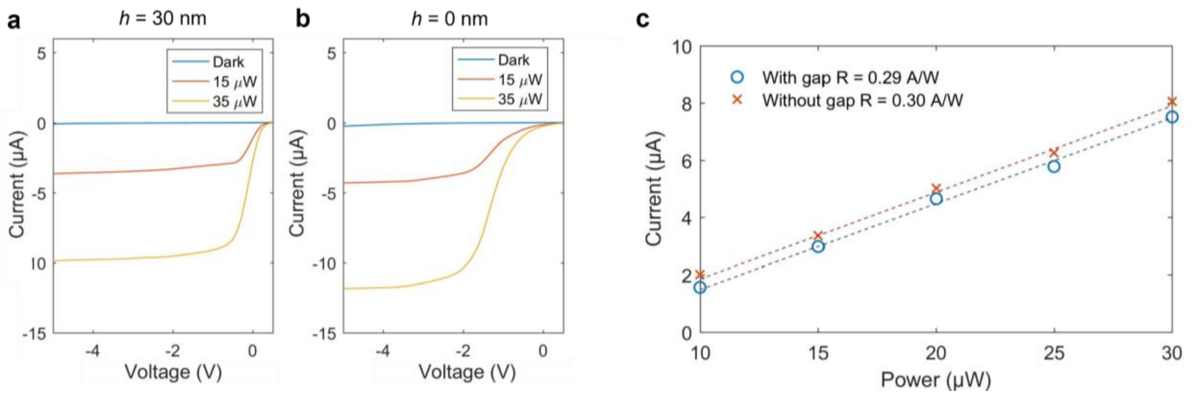

Fig. R3-10 (a) and (b) Photodetector I-V curves for devices with air gap values (a) $h = 30$ nm and (b) $h = 0$ nm, respectively, measured under 780 nm light wavelength. (c) Corresponding devices photoresponsivity.

Actions taken:

We have updated the new devices I-V curves and photoresponsivity, with related discussions on air gap h to revised main text Figs. 3f and 3g (highlighted by red dashed rectangle below) in Section 4.

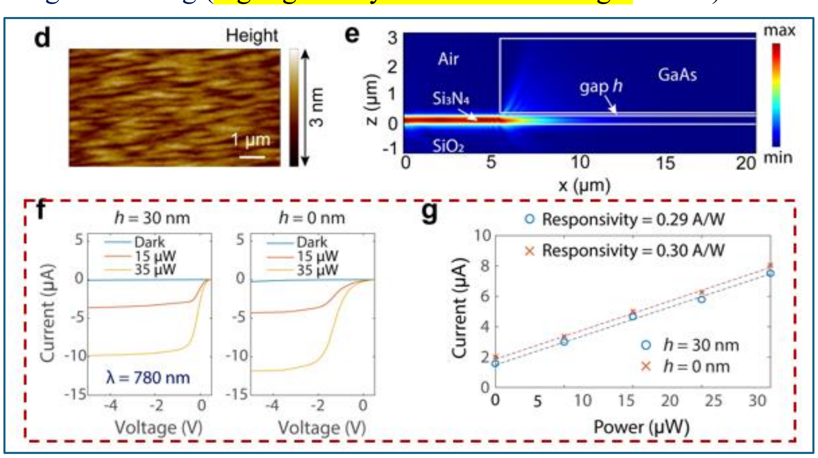

To pursue a clear and concise manuscript main text length, detailed discussions on the impact of air gap h on the light coupling and device performances are made in Supplementary Note S18 (as shown below).

> can further enhance performance of the vdW integrated III-V-SiN photodetectors. The presence of air gap h primarily affects the coupling length between the III-V nanomembrane and the SiN waveguide underneath. Numerical simulations indicate that over 99.9% of the input light power can be absorbed by the III-V layer after a 40 μm propagation length with air gap h = 30 nm (Fig. S32a). Similar photoresponsivity is observed for GaAs-SiN photodetectors with similar device size but different air gap heights (as main text Fig. 3f). Buried electrodes are applied to eliminate air gap to h = 0 nm (Figs. S32b,

Comment 3:

3. Regarding the IV of the detectors, especially the GaAs, the dark is quite high at ~1uA. While the zoomed-in TEMs look impeccable, this leaves the reader wondering if there are quite a few crystal defects outside of the zoomed-in TEM. Is the high dark current the result of higher defect density? Moreover, the responsivities of both detectors are lower than expected for these materials especially the 16.6mA/W at 405 nm. Is there an explanation for this?

Response 3:

We sincerely appreciate the reviewer for raising this constructive comment. The suggestion is well taken. We have revisited the photodetector dark current measurement with a more precise experimental setup fully blocking ambient illumination, and supplemented explicit dark current data to these vdW-integrated photodetectors with extended discussions.

(1) Reasons for the appearing big dark current in the initial photodetectors are due to imprecise dark current measurement setup, and the relatively big device sizes discussed later, not because of crystal defects outside the zoom-in TEM.

- The 'dark currents' quoted in the original manuscript were measured (via Keithley SMU, detailed in Methods) by turning off the laser in the photonic chip end-coupling setup. However, there was still lab ambient ceiling illumination (unable to remove) present, as this setup is primarily designed for testing photonic chip transmission. This dim ambient illumination has little impact on the I-V curves when laser power was injected to waveguide. However, it turns out to have a big impact on accurate current measurements, making the 'dark currents' shown in the original manuscript bigger than the actual values.

We have thus measured dark currents in another collaborator's different professional equipment, and fabricated new batch of GaAs vdW-integrated photodetectors to validate this claim. One reason is to further enhance the photodetector performances via surface oxide removal and passivation (detailed in revised Methods – Section 7). The other reason is that the prior GaAs photodetector samples (over 8 months ago, without SiO_2 cladding) had shown oxidized GaAs layer and degraded light in-coupling, when we tried for dark current remeasurements. New batches of freestanding III-V nanomembranes vdW-integrated photodetectors are thus fabricated for consistent dark current characterizations, also studying the impact of air gap h (detailed in Supplementary Note S18) for enhanced photoresponsivity.

As shown in Fig. R3-11 below, in the new measurements, these I-V curves are quoted as 'laser off' (as highlighted by the red dashed circles in Fig. R1-7 lower panels), which were inaccurately quoted as 'dark currents' in the original manuscript, and they are clearly higher than the true dark currents. For accurate dark current characterizations, we separately measured the devices in another fully enclosed probe station (C-6 Probe Station, Everbeing Int'l Corp., equipped with Keysight B1500A semiconductor device parameter analyzer, Keysight Technologies Inc., discussed in revised Methods – Section 7). We greatly appreciate this constructive comment from the reviewer, and sincerely apologize for the previously inaccurately measured photodetector dark currents, which were bigger than actual values.

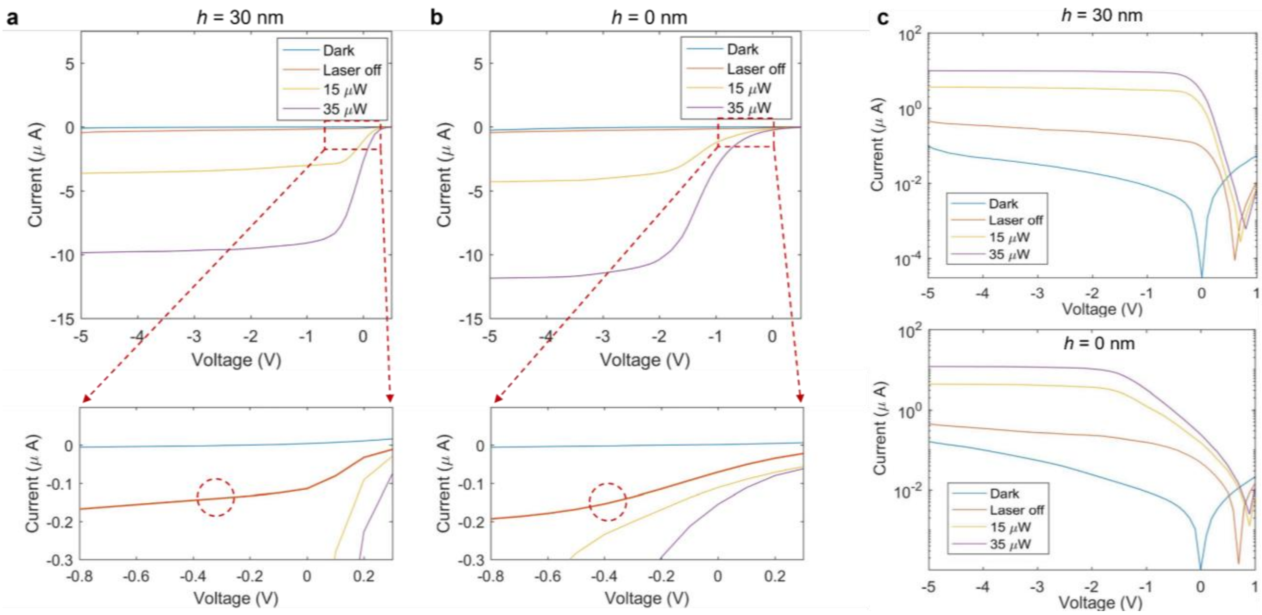

Fig. R3-11. I-V curve for the new GaAs-SiN photodetectors with air gaps (a) h = 30 nm, (b) and h = 0 nm (with buried electrodes structure), respectively. The dark currents are measured in a separate and fully enclosed probe station setup. Bottom panels: details zoom-in. Red dashed circles: I-V curves measured under laser-off and dim lab illumination condition, which was inaccurately quoted as 'dark currents' in the original manuscript. (c) Corresponding I-V logscale plots for y-axis.

(2) Another factor impacting device dark current values is device size.

To validate this claim, additional GaAs-SiN photodetectors are fabricated with reduced effective device area (i.e. approximated by electrodes-covered III-V film size). Much lower device dark currents are thus observed, as shown in Figs. R3-12a and R3-12b below.

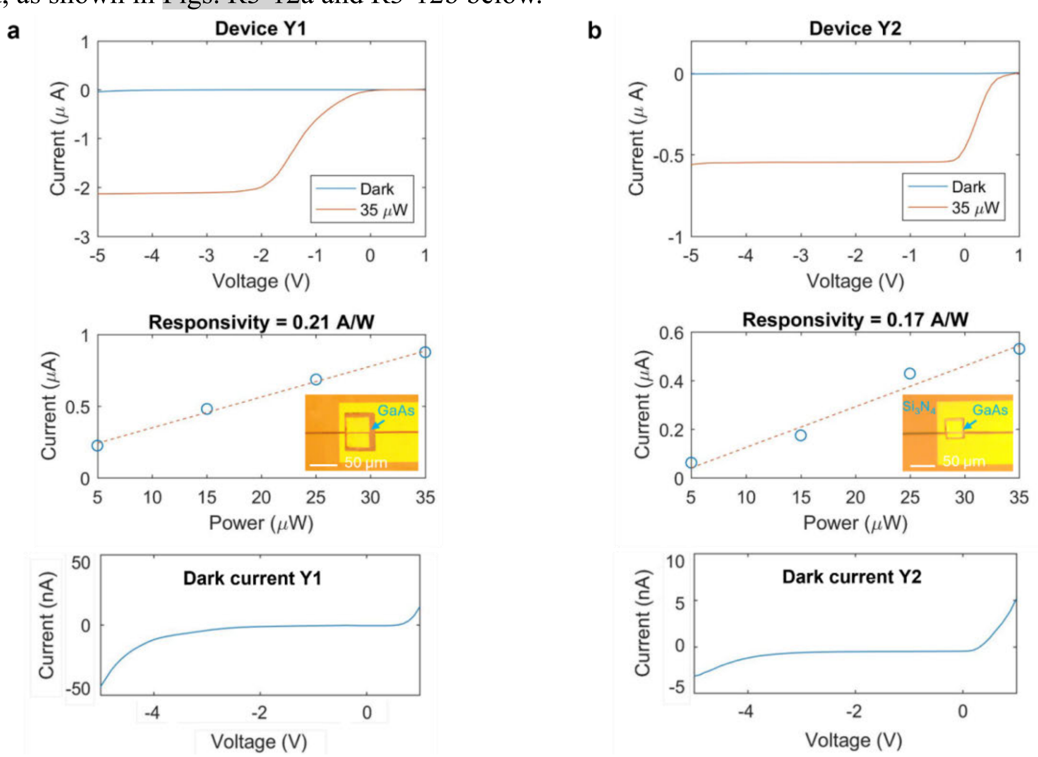

Fig. R3-12. (a) and (b) GaAs-SiN waveguide photodetectors with reduced effective device size, measured at $\lambda = 780$ nm, with air gap $h = 30$ nm. Both the electrodes and patterned GaAs film sizes are reduced. Top panels: device I-V curves. Middle panels: photoresponsivity. Inset panels: device micrographs. Bottom panels: device dark currents.

The photodetectors are made with conventional structure (shown as Fig. R3-9a above, i.e. an $h = 30$ nm gap exists) for comparatively simpler device fabrication process and much reduced sample EBL writing time, which is sufficient for testing the impact of effective device size on photodetector performances. The dark currents for device Y1 (with device area around 35 µm × 50 µm, shown in Fig. R3-12a inset) and device Y2 (with device area around 25 µm × 30 µm, shown in Fig. R3-12b inset) at -2 V bias voltage are largely recued to 1.2 nA and 0.54 nA, respectively (measured at 780 nm wavelength).

(3) We have re-measured the dark currents for all the photodetector devices discussed above (via another professional probe station-based setup).

The explicit photodetector dark currents are summarized as Fig. R3-13 below. The dark current values at -2V operation bias voltage are 16.4 nA (Fig. R3-13a) and 19.8 nA (Fig. R3-13b), corresponding to the devices shown in main text Fig. 3f left and 3f right panels, respectively, which remains a competitive value given the relatively large device area[26,42] (~120 µm × 160 µm, further benchmarked in revised Supplementary Notes S18 and S19). Further device dark current value details are also clearly quoted in revised Supplementary Note S18.

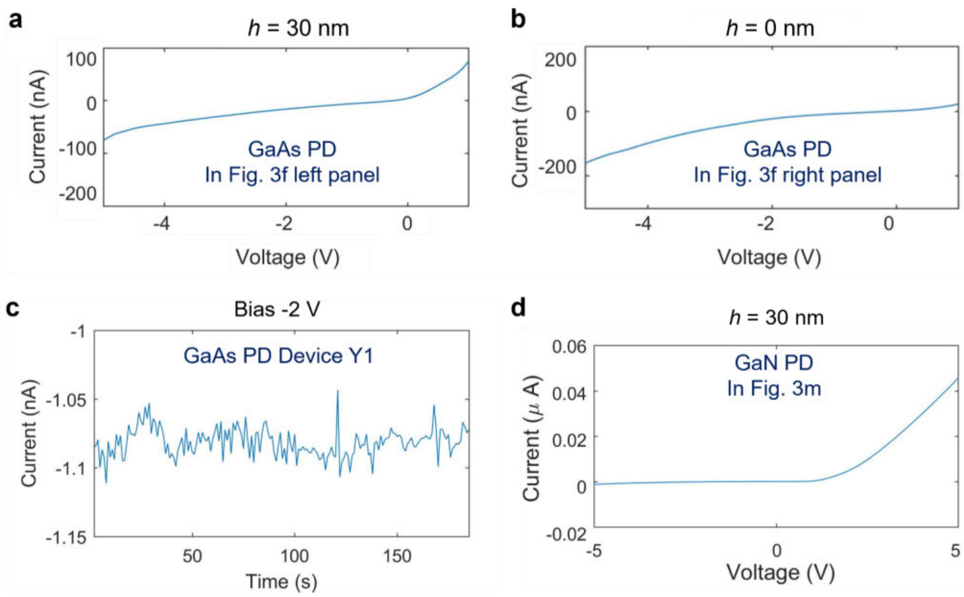

Fig. R3-13. Photodetector dark currents measured in fully enclosed probe station. (a) and (b) Device dark currents I-V curve for the photodetectors shown in main text Fig. 3f left panel (a) and right panel (b), respectively. (c) Measured photodetector dark currents as a function of time for another new photodetector device Y1 with ~35 µm × 50 µm effective device area size (devices shown in Fig. R3-9e above). (d) Measured dark currents for the proof-of-concept GaN-based photodetector (corresponding to Fig. 3m).

(4) Reason for the lower responsivity for GaN-SiN PD at ultraviolet (UV) wavelengths (405 nm) is the largely increased optical waveguide loss for our home-made SiN chips.

As the Rayleigh scattering from waveguide side wall roughness drastically increased at shorter wavelengths ($\sim\frac{1}{\lambda^4}$), the optimization and fabrication of ideal low-loss SiN (Si_3N_4) chips for short UV wavelengths is still a challenge[43,44], requiring both high-quality SiN device layers and heavily optimized SiN etching (e.g. Ref: ACS Photonics 5, 2145-2150, 2018. Ref: Optics Letters 51, 2332-2335, 2026). Besides, the optical loss of the UV fibers (coupled to laser diodes) and the fiber lenses for optical coupling are also 2 orders of magnitudes higher than the ones we used for visible and NIR optical measurements (Methods).

By measuring our bare SiN chips without vdW-integration, we obtained a high optical loss about 25 ~ 30 dB/cm for our home-made SiN waveguides (at 405 nm wavelength), a further optimization of which takes considerable lengthy efforts and is limited by our current facilities. The lossy SiN chips, blocking efficient optical power delivery through the waveguides, are the major source of the comparatively lower photoresponsivity of the proof-of-concept GaN nanomembranes-based photodetectors discussed in this work. Adopting advanced SiN chips can address it in future work.

Another contributing factor is the GaN films are unintentionally doped (UID), limited by current MBE remote epitaxial chamber. Applying carefully designed p-i-n doping structures for GaN films (or heterostructures such as GaN/Ga_2O_3) can further enhance its responsivity in future work. Extended discussions are made in revised Supplementary Note S18 (on Page 32 of the Supplementary Information).

(5) The freestanding GaAs and GaN nanomembranes explored in this work remain high crystal quality with low defects, as validated by the HR STEM images (in main text Fig. 3) for local defects, and the XRD (Fig. 1f), EBSD (Fig. 1g), and ECCI (discussed as Fig. R3-5 above in prior Response 1) characterizations, confirming low global defects.

Further details regarding the high quality of the GaAs and GaN nanomembranes are discussed in updated Supplementary Note S17 (on Page 31 of the Supplementary Information).

Actions taken:

New photodetectors (applied surface oxide removal and passivation for enhanced performance, detailed in Methods) are updated to revised Fig. 3 with accurately measured dark currents, and comparisons on the impact of air gap h on photodetection performance (revised Figs. 3f and 3g).

> Device dark currents are separately measured in an enclosed probe station (C-6 Probe Station, Everbeing Int'l Corp.) equipped with semiconductor device parameter analyzer (Keysight B1500A. The other *I-V* data are measured in the chip end-coupling setup fed with different laser sources (Methods, Fig. S33). The dark current for the GaN-SiN photodetector shown in main text Fig. 3m is 45.6 nA at 5V bias voltage. At -2 V bias voltage, the dark currents are 16.4 nA and 19.8 nA for the GaAs-SiN photodetectors shown in main text Fig. 3f left and 3f right panels, respectively. The photocurrent values are also largely related to the effective device sizes (under the case of sufficient light absorption from the underlying SiN waveguides). By further reducing the size of the electrode contacts and the patterned GaAs nanomembranes (Methods), much smaller dark currents are measured in smaller-sized photodetectors (with air gap h~30 nm): 1.2 nA and 0.54 nA for devices shown in Figs. S32d and S32e, respectively (at -2 V bias voltage), with slightly reduced photoresponsivity (with sufficient device length for light absorption).

To maintain a clear and concise main text manuscript length, detailed discussions regarding the impact of device size on photocurrents and the explicit dark currents data are made in revised Supplementary Note S18 and Supplementary Figs. S32, S33 (as highlighted in yellow shown above, on Page 33 of the Supplementary Information)

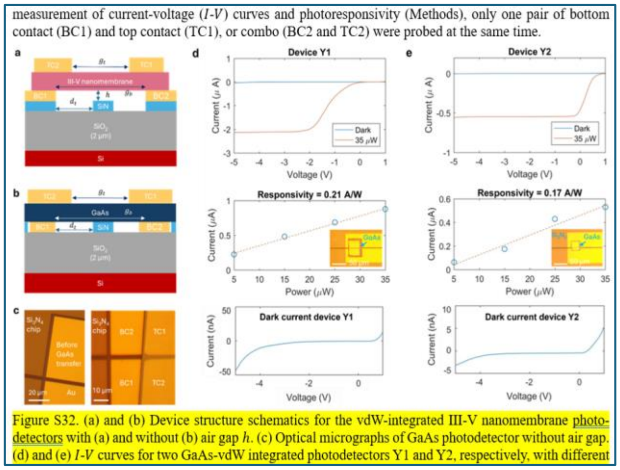

measurement of current-voltage (*I-V*) curves and photoresponsivity (Methods), only one pair of bottom contact (BC1) and top contact (TC1), or combo (BC2 and TC2) were probed at the same time.

Figure S32. (a) and (b) Device structure schematics for the vdW-integrated III-V nanomembrane photo-detectors with (a) and without (b) air gap *h*. (c) Optical micrographs of GaAs photodetector without air gap. (d) and (e) *I-V* curves for two GaAs-vdW integrated photodetectors Y1 and Y2, respectively, with different

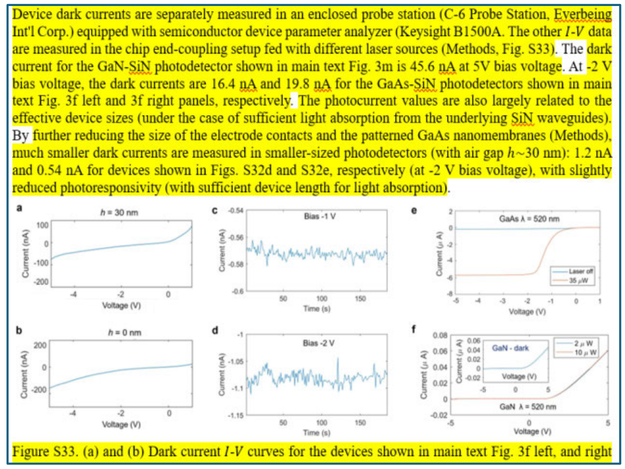

Device dark currents are separately measured in an enclosed probe station (C-6 Probe Station, Everbeing Int'l Corp.) equipped with semiconductor device parameter analyzer (Keysight B1500A. The other *I-V* data are measured in the chip end-coupling setup fed with different laser sources (Methods, Fig. S33). The dark current for the GaN-SiN photodetector shown in main text Fig. 3m is 45.6 nA at 5V bias voltage. At -2 V bias voltage, the dark currents are 16.4 nA and 19.8 nA for the GaAs-SiN photodetectors shown in main text Fig. 3f left and 3f right panels, respectively. The photocurrent values are also largely related to the effective device sizes (under the case of sufficient light absorption from the underlying SiN waveguides). By further reducing the size of the electrode contacts and the patterned GaAs nanomembranes (Methods), much smaller dark currents are measured in smaller-sized photodetectors (with air gap h~30 nm): 1.2 nA and 0.54 nA for devices shown in Figs. S32d and S32e, respectively (at -2 V bias voltage), with slightly reduced photoresponsivity (with sufficient device length for light absorption).

Figure S33. (a) and (b) Dark current *I-V* curves for the devices shown in main text Fig. 3f left, and right

Comment 4:

4. There is a demonstration of MO CFO optical isolator. Was there also an MO isolator using YIG as it is mentioned including the growth of thin-film YIG?

Response 4:

We thank the reviewer for this considerate comment.

For YIG, we studied its thin film material growth, single-crystallinity quality characterizations, freestanding YIG films lift-off, and its layer transfer to photonic substrates. Device implementation of YIG-based MO isolator was not conducted in this work due to not fully developed dry etching of YIG films and comparatively higher novelty of demonstrating CFO-based on-chip non-reciprocal devices.

(1) In this work, the epitaxial growth, lift-off, and transfer of single-crystalline freestanding YIG films via two exemplary approaches of 2DLT and ELO are explored.

Single-crystalline remote epitaxial YIG films for 2DLT are discussed in main text Fig. 1 and Methods Section 1. Given the stringent requirements on epitaxial substrate preparations (where the quality of the 2D layers coated on GGG substrates highly impacts the crystal quality and layer lift-off yield) and growth process optimizations for 2DLT (Ref: Nature Reviews Methods Primers 2, 40, 2022), ELO YIG films are also studied and compared with 2DLT YIG films. The pros and cons of the two approaches towards freestanding 3D MO nanomembranes YIG are discussed in revised Supplementary Note S5, and Fig. S12 (on Page 11 of the Supplementary Information). The results are briefly summarized as Fig. R3-14 below.

(2) To realize YIG-based non-reciprocal isolators, current device designs with external permanent magnets require the patterning of the MO nanomembranes (discussed in revised Supplementary Note S25), such as the CFO-based SOI micro-ring isolator shown in main text Figs. 4c, 4g). Otherwise, nonreciprocal phase shift (NRPS) for clockwise and counterclockwise light will be cancelled in round-trip propagation (without ring electromagnet), disabling optical isolation realization (detailed in Methods, Supplementary Note S22).

• For CFO nanomembranes, we have successfully patterned them via combined EBL and wet etching processes (via mixed HCl, H_3PO_4, and H_2O_2 solutions, detailed in Methods – Section 8). However, for vdW-integrated YIG nanomembranes, no ideal wet etchant was found so far that have good selectivity to YIG and the underlying SOI chip. The dry etching methods such ICP-RIE we have explored so far also showed nonideal etching selectivity (limited by our cleanroom facilities), and the etching also needs to be precisely stopped before the waveguide layer to avoid damaging to the underlying photonic structures.

• Another reason for not implementing MO isolators using YIG films is that we have already demonstrated CFO-based MO isolators, which attracts comparatively fewer attentions than YIG before, but possesses much higher Faraday rotation coefficient θ_F (about 100 times higher than YIG and 10 times higher than Ce: YIG[45-47]) essential for on-chip non-reciprocal applications.

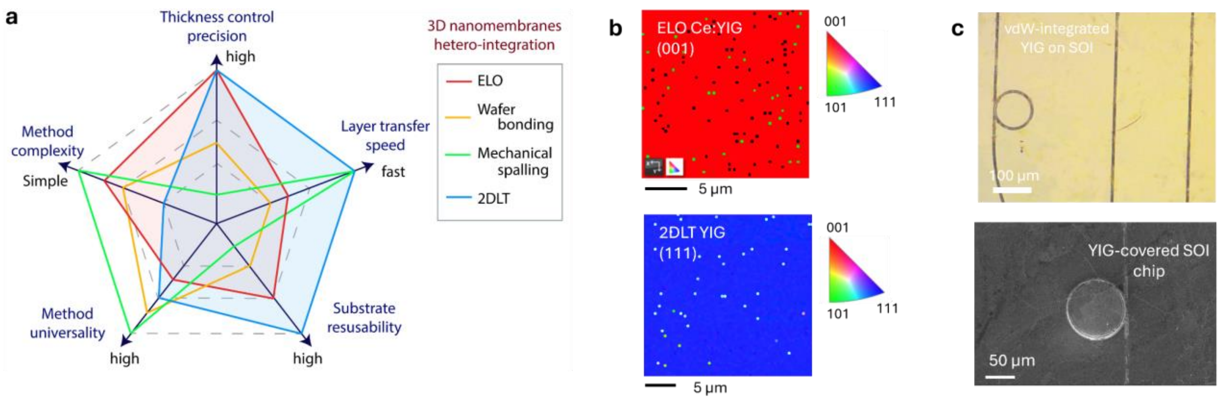

Fig. R3-14. (a) Comparisons of different heterogeneous photonic integration approaches. The ELO and 2DLT methods used in this work are shaded in red and blue colors, respectively. (b) Electron backscatter diffraction (EBSD) maps for ELO YIG (top panel) and 2DLT YIG (bottom panel). (c) Optical micrograph (top panel) and SEM images (bottom panel) of YIG-transferred SOI micro-ring.

Actions taken:

We have further clarified our study on freestanding YIG films in this work and the reasons for not implementing YIG-based MO isolators in revised Supplementary Note S25 (as highlighted in yellow, shown below, on Page 38 of the Supplementary Information).

> exclude the current-induced thermal tuning effect on the microring resonators. Current external magnet fully confirmed the feasibility of CFO-based MO applications excluding any thermal-related tuning effects. Nevertheless, fully integrated MO nonreciprocal devices can be envisaged in future work. The multifunctional electromagnetically reconfigurable microring demonstrated in this work can be further modified in device structure and design to enable magnetically mode conversion, polarization rotation, and non-reciprocal EO modulations for lasers[27,157], amplifiers[53], and in-memory computing[56,158] tasks. For freestanding YIG films, only its film growth, crystal quality characterizations, layer lift-off, and transfer are studied in this work (detailed in Supplementary Note S5). Device implementation of freestanding YIG nanomembranes is not carried out here due to not fully optimized YIG film patterning.

Comment 5:

5. CFO is mentioned as being magnetizable with a few hour demonstration. How does this approach compare with using harder thin-film magnets such as FeCoB in conjunction with softer magnetic materials such as YIG or Ce:YIG? In principle, the latter approach can hold state for much longer durations (years or decades).

Response 5:

We sincerely appreciate the reviewer for raising this insightful comment. The suggestion is well taken.

CFO theoretically functions identically as the combination of magnets and soft MO materials (such as the combo of FeCoB and Ce: YIG). CFO actually has significantly higher coercive field H_c than FeCoB, indicating potentially stronger remanent magnetization. The appearing shorter magnetizable time for the CFO vdW-integrated SOI ring in original manuscript, is due to insufficient CFO film magnetization process limited by experimental setup, as explained as follows.

(1) CFO directly functions as the MO material to simultaneously enable on-chip non-reciprocity and hard magnets for providing magnetic field, which is theoretically equivalent to the combo of FeCoB (magnet) and YIG or Ce: YIG (MO material).

As soft ferrimagnetic materials such as YIG or Ce: YIG with low coercivity H_c cannot retain its magnetization after the retrieval of external magnets, external magnetic field is indispensable to realize non-reciprocal applications using YIG or Ce: YIG. The external magnetic fields are typically realized by the ring-shaped electromagnets integrated on chip (e.g. in Ref: Nature Photonics 19, 54–62, 2025, and Ref: Nature Electronics 5, 604-610, 2022), or by external bulk permanent magnets with patterned MO materials on structure (e.g. in Ref: Nature Photonics 5, 758–762, 2011).

In contrast, the high coercive field H_c (300 ~ 400 kA/m, as benchmarked later in Table R3-2, shown later below) for hard ferromagnetic material CFO can retain appreciable remanent magnetization. CFO thus remains a versatile MO material that can replace the combo of FeCoB and Ce: YIG for on-chip non-reciprocal applications without necessitating other external magnets[48-51] (Ref: J. Mater. Chem. C, 13, 12628-12649, 2025. Ref: Advanced Functional Materials 26, 1954-1963, 2016).

(1.1) The key reason for the appearing shorter magnetization time for the CFO vdW hetero-integrated SOI ring in original manuscript is due to the insufficient magnetization process limited by our current experiment setup.

In initial demonstration, the devices (with CFO/SOI micro-rings) are magnetized in room temperature with a neodymium magnet. Actually, to pursue thorough magnetization, material heating above its Curie temperature (which is over ~450 °C for CFO) is typically applied to remove existing domain alignment, followed by a slow cooling within a strong external magnetic field persisted. This locks the domains in the desired direction as the material transitions back to a ferrimagnetic state to fully bring out its highest available magnetization.

However, our lab lacked such professional setup that precludes applying strong enough magnetic fields with controlled heating and cooling during sample magnetization. This is the major reason leading to the appearing diminishing non-reciprocal transmission of the devices after hours of removal from external magnets.

(1.2) Another contributing reason is the thin CFO film thickness applied for devices in this work.

For very stable and long hard magnets duration from months to years for FeCoB, bulk magnets are typically applied (Ref: AIP Advances 11, 075028, 2021), where the demagnetization process is impacted by the thickness and size of the magnetic materials. For example, in Ref: Nature Photonics 19, 54–62, 2025, a 500 nm- ~ 1 µm-thick FeCoB and Ce: YIG combo was applied.

In contrast, we applied thin CFO nanomembranes (~ 80 nm-thick for the device in main text Fig. 4c, and ~40 nm-thick for device in Fig. 4g) in this work, which has comparatively lower net magnetization.

(2) To validate this claim, we have made new batch of samples for a quick demonstration with thicker CFO film and modified magnetization process.

We transferred a 120 nm-thick CFO nanomembrane to a set of SOI micro-rings with ~ 60 µm radius and different coupling gaps. Another ~120 nm-thick SiO_2 cladding was deposited on the SOI chip by PECVD before CFO transfer, to protect the photonic structures from the CFO patterning and etching (Methods) into to a ~20 µm-wide strip atop the SOI micro-ring. We have also customized new aluminum racks that can securely hold a pair of magnets to enable the closer placement of stronger neodymium magnet pairs without the risks of crashing the samples in between (which was a limiting concern in our prior experiments). We tried a ~2-days magnetization with a heating temperature of 250 °C (further temperature increment over the Curie temperature of CFO was not conducted due to lab setup limitations), followed by a slow overnight cooling down with the presence of two neodymium magnets kept.

Representative results are shown as Fig. R3-15 below, evidencing a largely enhanced remanent magnetization for enabling the non-reciprocal split in the transmission of clockwise (CW) and counterclockwise (CCW) lights. Non-reciprocal transmission still persisted over 40 hours of removing the external magnets.

Although the transmission dips in Fig. R3-15 are, indeed, apparently nonideal for ultimate photonic devices, this brief test can still serve as a validation to our claims on the impact of film thickness and magnetization process discussed above. As we aim for brief and rapid validation, further fine tuning of the device structure to enable neat critical coupling of the CFO/SOI micro-ring will take considerably longer optimization time, and beyond the scope of this work targeting proof-of-concept validations for the proposed vdW integration platform. The direction of applying CFO for more robust magnet-less optical isolation and applications like non-volatile in-memory photonic computing can be explored in future works.

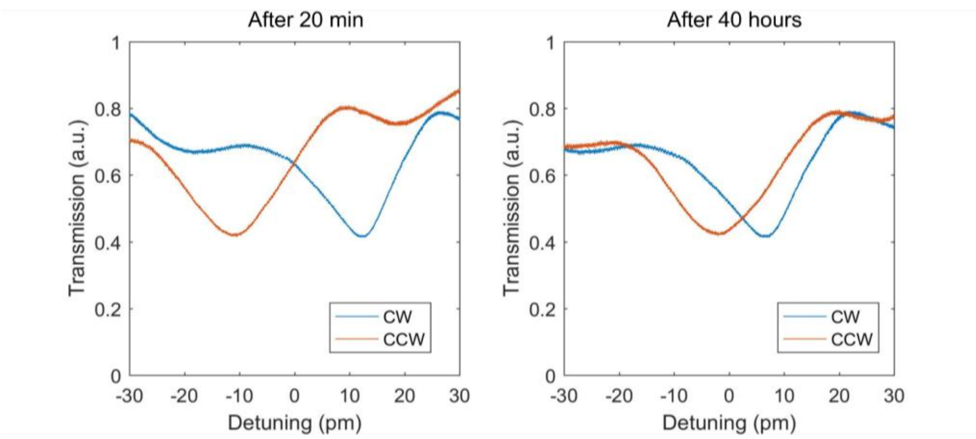

Fig. R3-15. CFO-SOI ring nonreciprocal transmission over time after removing external magnets.

(3) In summary, CFO is regarded as harder magnet than FeCoB (as reported by Refs: J. Mater. Chem. C, 13, 12628-12649, 2025, and benchmarked in Table R3-2 below), but with much lower optical loss than FeCoB for integrated photonic applications (Ref: IEEE Transactions on Magnetics 52, 2000204, 2015, Supplementary Note S24). CFO as a single hard ferromagnetic material can function identically as the combo of hard magnets (FeCoB) plus soft MO material (YIG or Ce: YIG) for compact and versatile on-chip nonreciprocal applications. Thicker CFO films with modified magnetization process can further fulfill the capacity of using CFO nanomembranes in vdW integration for integrated non-reciprocal applications without necessitating external magnets.

Table R3-2. Benchmarks of hard magnetic materials

Materials	**Coercive field H_c**	**H_c (kA/m)**	**Notes**	**Ref.**
CFO	2~5 kOe	100 ~ 400	CFO films and bulk layers.	ACS Omega 7, 43813 (2022) Adv. Funct. Mater. 26, 1954 (2016)
CoFeB	0.5 ~ 1 kOe	50 ~ 150	Opaque metal; Very high optical loss, not applicable in integrated photonics.	IEEE Transactions on Magnetics 47, 3104-3107 (2011)

NdFeB	10 ~ 30 kOe	800 ~ 2400	Opaque metal; Very high optical loss, not applicable in integrated photonics.	Sci. Technol. Adv. Mater. 4, 386-403 (2021)
$BaFe_{12}O_{19}$	4 ~ 7 kOe	300 ~ 600	Higher optical loss than CFO.	J. Magnetism and Magnetic Mater. 341, 79–85 (2013)

Notes: CFO: cobalt ferrite ($CoFe_2O_4$). H_c: Coercive field. Most hard magnetic materials are opaque metal composites, such as the NdFeB (neodymium magnets), with very high loss not applicable to integrated photonic applications.

Actions taken:

We have further clarified the functionality and benefits of using CFO, with extended discussions on further steps to further enhance the magnetization of the proposed devices added to revised Supplementary Note S21 on Page 35 (highlighted in yellow) of the Supplementary Information.

> integrated CFO nanomembranes permits optical isolation without external magnets after CFO magnetization, functioning identically as the combo of hard magnets (e.g. CoFeB) and soft MO materials (e.g. Ce:YIG)[56].
>
> Figure S34a shows the normalized optical transmission of the CFO-integrated SOI microring after removing the permanent magnet for 30 minutes. The single-crystallinity film quality enables stronger magnetic responses than those based on poly-crystal CFO films[137,139,140], persisting after magnets retrieval (Fig. S34b, can be enhanced in time juration). The fabricated devices were magnetized at room temperature by a neodymium magnet overnight with ~300 mT magnetic field intensity limited by experimental setup. Current setup limits the sufficient magnetization of the CFO nanomembranes vdW-integrated to the SOI chips (Fig. S34), which can be further enhanced by applying stronger magnets and engineered sample heating and cooling procedures during magnetization[86,136,141] for compact optical isolators.

Comment 6:

6. Why is the co-integration of EO BTO material and MO CFO materials into a single ring-resonator device relevant or important? The authors make it clear that the EO modulation device is functioning only for the TE mode while the MO isolation device is working for only the TM mode. While intriguing, one would need to have both TE and TM modes in this device whereas most applications typically have one or the other. Does this introduce un-necessary material losses especially from evanescent mode coupling to CFO thin-film atop the BTO film? The losses for CFO are listed in Figure 5c.

Response 6:

We sincerely thank the reviewer for this constructive comment. We have further clarified the application scenarios and highlighted the value and impact of integrating multiple single-crystalline functional optical layers for advanced multifunctional photonic systems.

(1) The co-integration of EO material BTO and MO material CFO is primarily a proof-of-concept example to embody the competence of creating arbitrary heterogeneous photonic integration layouts by vertically stacking freestanding 3D nanomembranes via photonic vdW integration.

Beyond this CFO/BTO example, the capability to heterogeneously integrate multiple high-quality functional optical layers is of vital importance to unlock various multifunctional and ultracompact photonic systems, such as wide-spectrum light sources[43] (Ref: Nature 610, 54–60, 2022), full-color LEDs[52] (Ref: Nature 614, 81-87, 2023), and diverse nonlinear and quantum applications (Ref: Nature Reviews Materials 9, 321–346, 2024), which are made possible by co-integrating multiple different optoelectronic materials.

Therefore, the main motivation of the SOI micro-ring integrated with CFO/BTO artificial 3D heterostructures is to validate the unique advantage of photonic vdW integration in coalescing different functional materials with radically distinct crystal structures but with optimal single-crystallinity, which can find values in different concrete application scenarios and the promise for photonic 3D integration (discussed later). Besides the vertical stacking (CFO/BTO heterostructures as a brief example, in main text Fig. 4), the lateral stitching of GaAs and GaN nanomembranes on a single SiN chip (Fig. 3) is also demonstrated as another example to illustrate the handiness and high degrees of freedom for the proposed photonic vdW integration strategy towards heterogeneous photonic integration.

(2) For the specific case of CFO and BTO co-integrated micro-ring resonator, we appreciate the reviewer for this considerate suggestion. Indeed, this current multifunctional micro-ring demonstrated in this work deploys TE modes in EO modulation, and TM modes operating in optical isolation. Nevertheless, this device can be applied in, for example, mode-division-multiplexing (MDM) systems for multifunctional EO and MO reconfigurations (e.g. Ref: Nature Communications 17, 28, 2026; Ref: Nature Communications 17, 1162, 2026).

• By adopting carefully designed asymmetric hybrid waveguide structures[53] (Ref: Scientific Reports 15, 20381, 2025; Ref: Optics Express 30 (6), 9934-9943, 2022), the EO modulation and MO isolation can also be realized in a single fundamental optical mode. Nevertheless, this requires intensive optimization as the design would be very sensitive to the nanofabrication of complex device structures (Ref: Optics Express 29 (15), 22838-22846, 2021) and/or the precise patterning of MO materials[48,54] (Ref: Optics Letters 46 (10), 2396-2399, 2021), for realizing appreciable critical coupling and optical isolation performance, which will go beyond the scope of this paper demonstrating the framework, strengths, and key features for the versatile photonic vdW integration platform.

• For optical losses, the evanescent coupling between the waveguide and the EO and MO layers indeed will introduce additional loss. Nevertheless, this coupling is indispensable for realizing multifunctional photonic devices and systems and remains universal in heterogeneous photonic interactions. This can be acceptable and understandable, given that adding more layers and more structures will inevitably introduce additional losses, trading for expanded system functionalities and performance in other metrics. Compared to conventional heteroepitaxial-based approaches with poor crystal quality and high material defects, the vdW integration of the single-crystalline nanomembranes with low defects and uniform morphology explored in this work (as discussed in Figs. S6, S7, and the revised Supplementary Notes S14, S16, S17) shows competitive or comparable optical loss compared to previous works with hybrid waveguide structures: 2.5 dB/cm extra loss (overall loss 3~5 dB) for the BTO/Si hybrid EO waveguide and 9~10 dB/cm for the CFO/Si (with SiO_2 spacer layer) hybrid MO waveguides, as benchmarked in Table R3-3 below.

Table R3-3. Benchmarks of hard magnetic materials

Hybrid WG structure	**WG core material**	**Functional layer**	**Hybrid WG loss (dB/cm)**	**Integration method**	**Ref.**
Si + LN	Si	LN	4.3	LN layer bonding to Si.	Scientific Reports 6, 22301 (2016)
Si + LN	Si	LN	0.98	BCB bonding of LN layer.	Nature Photonics 13, 359–364 (2019)
Si + LN	Si	LN	0.8	LN wafer bonding to Si.	Scientific Reports 12, 18611 (2022)
Si + LN	Si	LN	15	Deposited a-Si core atop LNOI.	APL Photonics 7, 126103 (2022)
Si + LN	Si	LN	1.2	LN film transfer integration.	Mater. Today Commun. 40, 109834 (2024)
SiN + LN	SiN	LN	2.03	Deposited SiN and chip bonding	Optics Express 32, 9171-9183 (2024)
SiN + LN	SiN	LN	2*	Bonded thib-film LN to SiN.	Optica 10, 5, 578-584 (2023)
BTO + Si	Si	BTO	10*	MBE grown BTO bonded to Si.	Nature Materials 18, 42–47 (2019)
BTO + Si	Si	BTO	5.8	MBE grown BTO wafer bonding.	J. Lightwave Technol. 37, 1456 (2019)
BTO + Si	Si	BTO	6*	MBE grown BTO wafer bonding.	J. Lightwave Technol. 34, 1688 (2016)
BTO + Si	Si	BTO	44	Deposited a-Si on grown BTO/Si.	Nano Lett. 14, 1419–1425 (2014)
BTO + Si	Si	BTO	6	Grown BTO on SOI.	ACS Photonics 3, 1698–1703 (2016)
BTO + Si	Si	BTO	2	Grown BTO on SOI.	J. Appl. Phys. 134, 073101 (2023)
BTO + Si	Si	BTO	11.3	Grown BTO on SOI.	Adv. Photon. Nexus 3, 066005 (2024)
BTO + SiN	SiN	BTO	5.6	Grown BTO bonded to SOI	Nature Materials 19, 1164–1168 (2020)
BTO + SiN	SiN	BTO	9.4	MBE grown BTO deposited SiN.	ACS Photonics 6, 2677–2684 (2019)
PZT + Si	Si	PZT	5.2	Grown PZT on SOI.	Optics Letters 49, 6353-6356 (2024)

PZT + Si	Si	PZT	2	Grown PZT on SOI.	Nature Communications 16, 6340 (2025)
YIG + Si	Si	Ce: YIG	40*	Bonded Ce: YIG to SOI.	Optica 4, 23-30 (2017)
YIG + Si	Si	YIG	81	Grown YIG on Si.	Opt. Mater. Exp. 14, 1579-1589 (2024)
YIG + SiN	SiN	Ce: YIG	15*	Grown Ce: YIG on SiN.	Optica 6, 473-478 (2019)
TbIG + Si	Si	Ce: TbIG	14.7	Grown TbIG on SOI with SiN.	ACS Photonics 6, 2455–2461 (2019)

Notes: WG: waveguide. SiN: silicon nitride (Si_3N_4). LN: lithium niobate. BTO: barium titanate. PZT: lead zirconate titanate. YIG: yttrium iron garnet. TbIG: terbium iron garnet. SOI: silicon-on-insulator. LNOI: lithium niobate-on-insulator. Superscript * represents calculated or estimated values from references data.

(3) Beyond this example of CFO/BTO stacked micro-ring resonator, this work can find extended value in realizing 3D photonics integration[13,55] and serve as an intriguing playground for studying fundamental physics and advancing nanomembrane technologies.

The vertical stacking of different functional optical layers can be very useful in various 3D hetero-integrated photonic applications (Ref: Nature 620, 78–85, 2023; Ref: Nature Electronics 7, 422–424, 2024), which requires the stacking and coupling of different functional layers to realize multifunctional and high-performance photonic systems, such as on-chip laser generations (e.g. Ref: Nature 615, 411–417, 2023) and photonic computing tasks (Ref: Nature Electronics 5, 386-393, 2022), by applying the vdW-integration approach to modified Si and/or SiN photonics with altered device structure accordingly.

In Supplementary Fig. S10, for a primitive example, we have demonstrated an exemplary 3D artificial heterostructure, including optical gain and photodetection material (GaAs and GaN), EO material (BTO), MO material (CFO), and high-*k* dielectrics (STO) atop SiO_2 substrate (as shown below), where all stacked layers are single-crystalline with desperately distinct crystal structure inaccessible via conventional heteroepitaxy. These functional layers, as 3D vdW Lego building blocks, can be further combined and engineered with real optical structures for developing different 3D-integrated photonic systems, covering light generation, processing, and detection capabilities for future exploration.

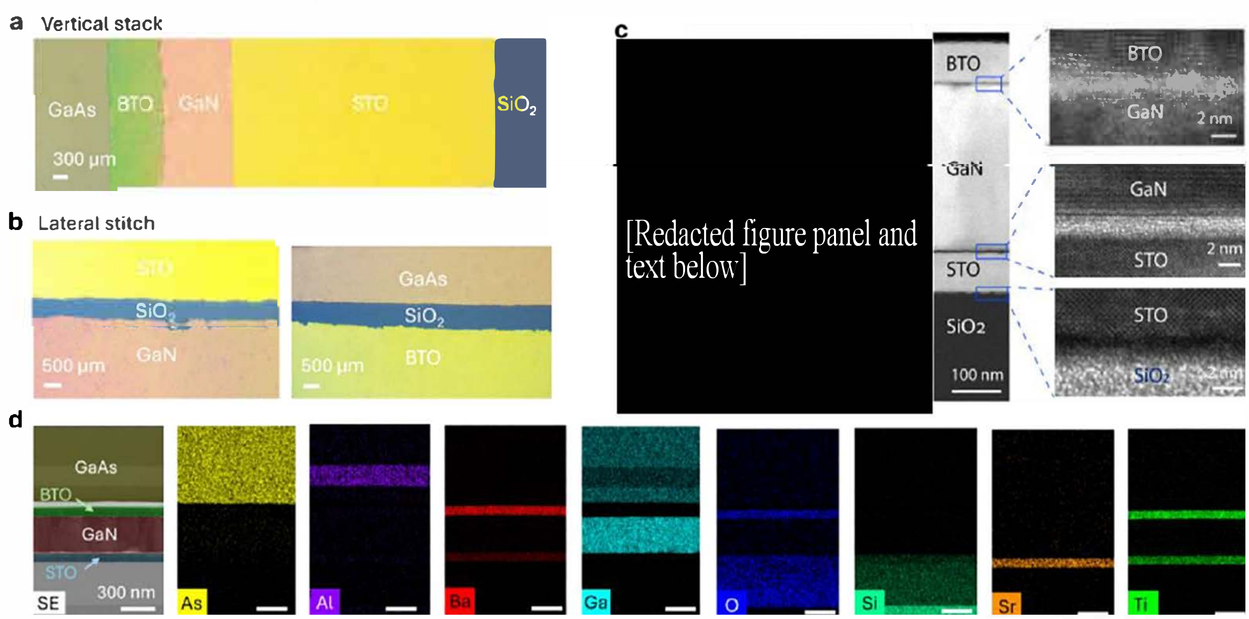

Figure S10. vdW integration of distinct single-crystalline freestanding nanomembranes. (a) and (b) vdW integration modes: Optical microscope photos of vertical stacking (a) and lateral stitching (b) of 3D nanomembranes. [redacted] (d) EDS data of a GaAs/BTO/GaN/STO heterostructure atop SiO_2 substrate. SE: second electron.

A versatile and handy platform also unfolds for studying fundamental physics and coupling between multidimensional nanomembranes beyond 2D to 3D/3D (e.g. Ref: Nature 626, 529-534, 2024. Ref: Nature Nanotechnology 20, 881-888, 2025), 3D/2D (Ref: Science 384, 312-317, 2024. Ref: Nature Communications 17, 3025, 2026) and beyond.

Actions taken:

We have clarified the application scenarios for the CFO/BTO co-integrated micro-ring resonator, along with its extended value beyond this currently demonstrated example in revised Supplementary Note S25 (as highlighted in yellow, on Page 38 of the Supplementary Information).

> Nevertheless, fully integrated MO nonreciprocal devices can be envisaged in future work. The multifunctional electromagnetically reconfigurable microring demonstrated in this work can be further modified in device structure and design to enable magnetically mode conversion, polarization rotation, and non-reciprocal EO modulations for lasers[27,157], amplifiers[53], and in-memory computing[56,158] tasks. For

Further potential applications and impact for using this proposed single-crystalline freestanding 3D Lego building blocks for heterogeneous photonic integration are also discussed on revised Supplementary Note S3 (as shown below).

> artificial heterostructure stacked on SiO_2 substrate (Fig. S10d), GaAs, BTO, GaN, and STO are colored as yellow, green, red, and blue in the first panel, respectively. We note that this artificial heterostructure stack of GaAs/BTO/GaN/STO is only an example to embody the capability of photonic vdW integration for constructing arbitrary desired high-quality functional optical layers on arbitrary substrate, which can find great value and broad applications in multifunctional hetero-integrated photonics[41-43] and 3D photonics integration[44,45]. A more specific demonstration of such stacked photonic system is beyond the scope of this work. A versatile platform is thus created for advancing nanomembranes technology[18,46-48], studying physical coupling[2,49,50], and prototyping exotic heterogeneous integrated photonic applications[15,25,51-53].

Comment 7.1:

Minor comments:

1. Please define acronyms in the main manuscript, not just in figure captions (i.e. PDMS, TRT, etc).

Response 7.1:

We thank the reviewer for the considerate comment. We have defined the acronyms, including PDMS, TRT, PPC, etc., in main manuscript accordingly.

In main text Section 2, paragraph 2 (on Page 4, highlighted in yellow):

> epitaxial layer and substrate[12], the epilayer can be mechanically exfoliated from substrate with atomically smooth interfaces[9] with thermal release tape (TRT) handler in a fast[57], cost-saving[18], wafer-scale, and high-throughput manner[14,16].

In main text Section 3, paragraph 3:

> verified well-defined crystallographic orientation of the delaminated a-axis BTO single-crystal resting on polydimethylsiloxane (PDMS) by 2θ-ω-scanning XRD (Fig. 2b), with ultranarrow BTO (200) Bragg peak (Supplementary Note S2). Detailed reciprocal space mapping (RSM) reveals

In revised Figure 1 caption:

Figure 1. Single-crystalline functional nanomembranes for photonic vdW integration.
(a) Infusing desired optical functionalities to Si and SiN photonics via vdW integration[11], such as EO modulation, MO isolation, and wide-spectrum photodetection. (b) Top panel: remote epitaxy[12,56] through 2D materials facilitates the release of single-crystalline epilayers. Bottom panel: 2DLT of freestanding 3D nanomembranes[10,17]. (c) Top panel: epitaxial lift-off[8,36] for thin film materials. Bottom panel: Wet transfer of 3D nanomembranes. (d) Photonic vdW integration modes: vertical stacking with optional rotation angle[19] (top), or lateral stitching (bottom). (e) Photographs of delaminated functional 3D nanomembranes resting on supportive polydimethylsiloxane (PDMS, for BTO, CFO, and YIG) or thermal release tape (TRT, for GaN and GaAs) handlers. (f) and (g) Asymmetric XRD ϕ-scan (h) and the corresponding EBSD map (i), respectively, of the ELO BTO, ELO CFO, 2DLT YIG, 2DLT GaN, and ELO GaAs nanomembranes (Supplementary Note S1).

In Methods, section 2.

were tested, including polypropylene carbonate (PPC), polymethylmethacrylate (PMMA), ethylene-vinyl acetate (EVA), polydimethylsiloxane (PDMS), with different Young's modulus (see Ref.[82]), and thermal release tape (TRT). Overall, PPC was found effective for most ELO film

Comment 7.2:

2. Placement of figure 1f is a bit confusing (perhaps have this also read horizontally like the other sub figures)

Response 7.2:

We thank the reviewer for the detailed comment. We have modified the panel arrangement and their labels (panels b ~ d) in revised Fig. 1 (as attached below), accordingly.

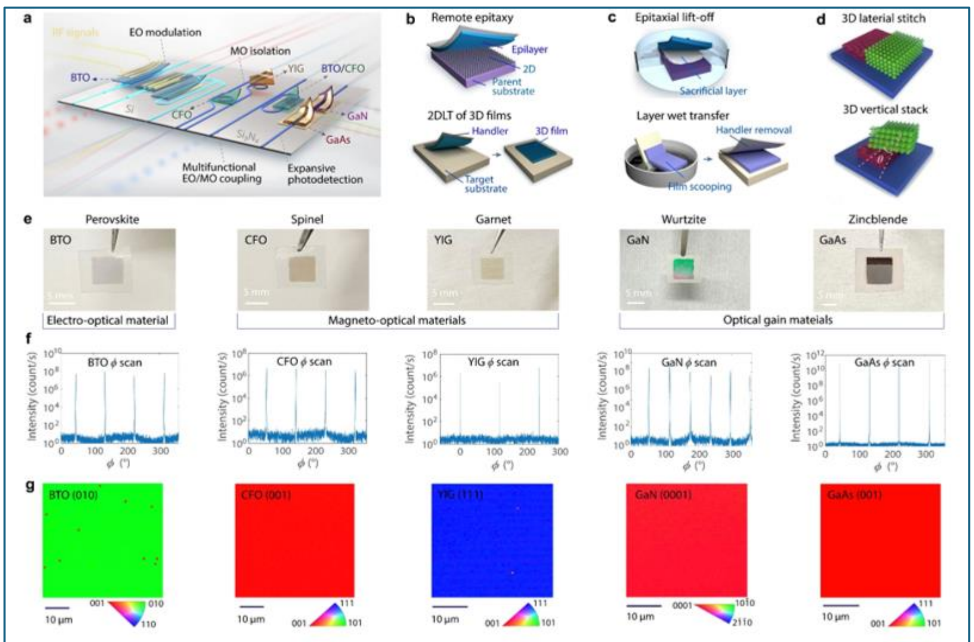

Figure 1. Single-crystalline functional nanomembranes for photonic vdW integration.
(a) Infusing desired optical functionalities to Si and SiN photonics via vdW integration[11], such as EO modulation, MO isolation, and wide-spectrum photodetection. (b) Top panel: remote epitaxy[12,56] through 2D materials facilitates the release of single-crystalline epilayers. Bottom panel: 2DLT of freestanding 3D nanomembranes[10,17]. (c) Top panel: epitaxial lift-off[8,36] for thin film materials. Bottom panel: Wet transfer of 3D nanomembranes. (d) Photonic vdW integration modes: vertical stacking with optional rotation angle[19] (top), or lateral stitching (bottom). (e)

Comment 7.3:

3. For Figure 3 caption for photodetectors, please state the wavelength of operation and responsivity values in the caption text (easily missed in the figure insets).

Response 7.3:

We appreciate the reviewer's kind reminder. The operation wavelength and responsivity values are added to the caption of Fig. 3 accordingly (as appended below, highlighted in yellow).

photodetector cross-section, revealing efficient light absorption with air gap h~30 nm. (f) Current-voltage (I-V) curve of the vdW-GaAs/SiN photodetector at different pump light intensities for h = 30 nm (left panel) and h = 0 nm (right panel) at λ = 780 nm wavelength. (g) Fitted device photoresponsivity of 0.29 A/W and 0.3 A/W for h = 30 nm and 0 nm, respectively. (h) HR-TEM image of the GaN/SiN interface. (i) Optical micrograph of the vdW-integrated GaN/SiN photodetectors. (j) Top panel: Cross-sectional structure for the GaAs and GaN co-integrated photodetector. Bottom panel: Optical micrograph of the fabricated device. (k) AFM of the GaN film surface. (l) Simulated $|\mathbf{E}_{\text{opt}}|$ distribution along the GaN/SiN photodetector longitudinal cross-section. (m) and (n) Representative I-V curves (m) and the corresponding photoresponsivity fit of 17 mA/W (n) of the photodetector at λ = 405 nm, respectively.

Comment 7.4:

4. Figure 5a is not referenced in the manuscript. Also Figure 4g-k are mis-labeled in the text on page 10 as Figures 5g-k.

Response 7.4:

We sincerely thank the reviewer for the considerate reminder. We apologize for the typo, and we have added reference of Fig. 5a in revised Section 6, paragraph 2 (marked in yellow, as appended below).

crystallographic quality and orientation of the functional materials[52,66] such as BTO[42,43,45]. We demonstrate highly efficient BTO MZMs with ultralow $V_\pi L$ ≈0.29 V·cm, corresponding to a giant effective Pockels coefficient r_{eff} ≈ 950 pm/V (Fig. 5a), equivalent to r_{42} >1290 pm/V surpassing previous works[24,43,45-47,67] (Fig. 5b, Supplementary Note S12). High-speed EO modulation[24] is realized as well with a 3 dB EO bandwidth over 23 GHz. We also report efficacious MO non-reciprocal optical isolation by vdW-integration, showcasing a large Faraday rotation coefficient[48-

The labels for Figs. 4g-4k are also updated accordingly in the last paragraph of revised main text Section 5.

devices for simultaneous EO and MO modulations are shown as Fig. 4g. The simulated static electric field and magnetic field distributions for fundamental TE-mode (EO modulation) and TM-mode (MO isolation), respectively, are illustrated as Fig. 4h. Exemplary EO modulation (Fig. 4i) and resonant frequency tuning of this CFO/BTO hetero-integrated microring under different bias voltages (Fig. 4j) are experimentally observed. By adjusting the input laser polarization (Methods) and switching external magnetic field direction, MO modulation is confirmed with a nonreciprocal wavelength shift λ_{MO} ≈ 5 pm and an ER over 13 dB (Fig. 4k). EO modulation and MO isolation under same optical mode are also feasible by judicious device design. Fully integrated devices can be envisaged as well by replacing external magnets to ring-shaped electromagnets atop CFO[38,40] (Supplementary Note S25), for expansive optoelectronic applications in data storage and spintronics[64].

Comment 7.5

5. At the end of section 4, please specify which material (GaAs or GaN) was used for each wavelength. The assumption is GaN at 520nm wavelength and the IV data is not shown for this.

Response 7.5:

We thank the reviewer for the instructive comment. The suggestion is taken fully. Explicit info on photodetection materials and their operation wavelengths is added accordingly, in revised Section 4, last paragraph (as highlighted in yellow, shown below).

> (Fig. 3m). Photoresponsivity is measured over broad discrete wavelengths of 0.3 A/W (based on GaAs) at light wavelength $\lambda = 780$ nm, 0.16 A/W (based on GaAs) at $\lambda = 520$ nm, and 17 mA/W (based on GaN) at $\lambda = 405$ nm (Fig. 3n) for this GaAs and GaN co-integrated chip (Supplementary Note S18). Despite proof-of-concept demonstration, this prototypical photodetector performance

The vdW-integrated GaN-SiN photodetector primarily operates for ultraviolet (UV) wavelengths (shorter UV wavelengths measurements below 405 nm were not conducted due to largely increased SiN chip loss). The I-V curves for the GaN-SiN photodetector are shown as Supplementary Fig. S33f (appended below as Fig. R3-16a below), where the photon energy (520 nm) significantly below the bandgap of GaN cannot induce any appreciable photodetection. The I-V curves for the GaAs-SiN photodetector (with air gap h = 30 nm) are also appended below as Fig. R3-16b (added details to revised Supplementary Note S18).

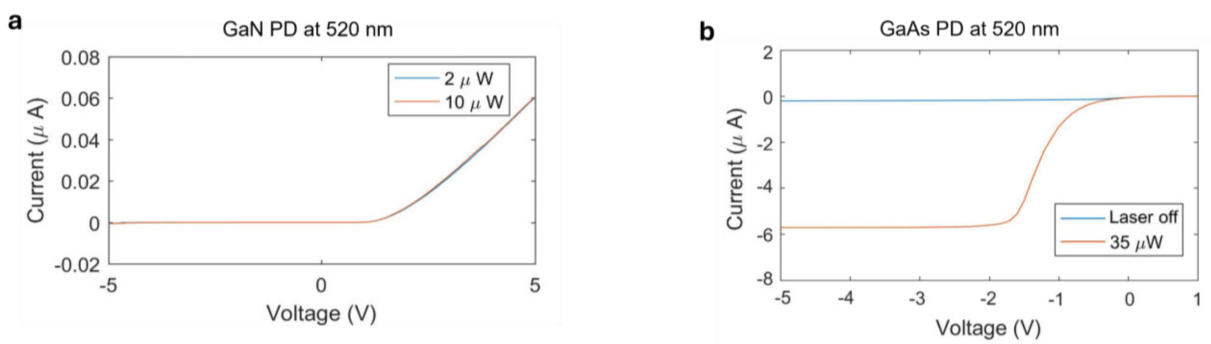

Fig. R3-16. (a) I-V curves for the GaN-SiN photodetector (PD) at 520 nm wavelength. (b) I-V curves for the GaAs-SiN PD at 520 nm.

Comment 8:

Overall, this paper is an amalgamation of different thin-film materials being integrated onto Si and SiN photonic circuits. All of these materials have been integrated onto Si and SiN in other works with far better performance on the individual devices than reported here in this paper. The true novelty is perhaps in the material science aspect of remote epitaxy. The sheer volume of work reported here is impressive and perhaps too much for a single journal paper and could be split into 4 or 5 individual papers. With all that said, this paper is not a good fit for Nature. Perhaps it is a better fit for Nature Materials.

Response 8:

We sincerely thank the reviewer for the assessment of our manuscript. We apologize for not sufficiently highlighting the novelty and impact of this work in the previous version, and we have thus carefully revised our manuscript accordingly for clarification.

Nevertheless, we would like to further justify the advancement and competitiveness of the device performances reported in this work, and the solid novelty with broad impact of this manuscript competence for publication on Nature as follows.

(1) The performances of the vdW hetero-integrated photonic devices in this work are comparable with or better than state-of-the-art previously published works, with several record-setting device performance parameters despite proof-of-concept application demonstrations.

(1.1) For BTO-integrated Si EO Mach-Zehnder modulators (MZMs) in this work, its core device performance parameters: half-wave voltage-length product ($V_\pi \cdot L$), EO bandwidth, and effective Pockels coefficient (r_{eff}), are either comparable to published references or remain record-high among prior works with similar device configurations as benchmarked below.

• The *in-plane* Pockels coefficient r_{eff} of the BTO MZMs in this work are record-high for integrated photonic applications to the best of our knowledge.

The effective Pockels coefficient r_{eff} is central parameter to evaluate the overall linear electro-optical (EO) process that has proven profound impact in integrated photonic devices over the past decade[4,23,56-60]. This r_{eff} is highly dependent on EO material crystal quality and especially its crystallographic orientations (which were not properly addressed in some previous references) as discussed later.

Thanks to the single-crystalline freestanding BTO films with ultrahigh material quality and attentively engineered crystal orientations, which is a fundamentally distinct hetero-integration strategy to previous heteroepitaxy-based approaches (grow BTO on Si or SiO_2 with engineered thin buffer layer such as STO) fundamentally limited by lattice mismatch, we experimentally demonstrated record-high BTO effective *in-plane* Pockels coefficient r_{eff} to the best of our knowledge, as benchmarked in Table R3-4 below.

Table R3-4. Brief benchmarks of the BTO r_{eff} in this work with prior references using BTO or other EO materials

EO Material	**Hybrid waveguide?**	$r_{\mathrm{eff}}^{\parallel}$ **(pm/V)**	**Largest r_{ij} (pm/V)**	**Notes on material preparations**	**Reference**
BTO	Yes (Si–BTO)	680*	923	MBE BTO on Si with STO buffer. Wafer bonding & substrate grinding applied.	Nature Materials 18, 42–47 (2019)
BTO	Yes (Si–BTO)	213	—	MBE BTO on SOI with engineered STO buffer layer. Top Si hybrid slab WG.	Nano Lett. 14 (3), 1419–1425 (2014).
		—	—		
BTO	Yes (Si–BTO)	48	—	Transferred freestanding *c*-axis-domain BTO.	Light: Adv. Manufact. 5, 31 (2024)
BTO	Yes (Si–BTO & SiN-BTO)	200	—	MBE BTO on Si with engineered STO buffer.	Nature Materials 19, 1164-1168 (2020)
BTO	Yes (SiN–BTO)	624*	> 1000	BTO growth with engineered STO buffer.	Nature 641, 876-883 (2025)
BTO	N/A	388*	<500*	RF sputtered BTO on SiO_2 with buffer.	Nature Materials 24, 868-875 (2025).
BTO	N/A	121	—	BTO epitaxy on STO with $BaSnO_3$ buffer.	Phys. Rev. Mater. 5, 035201 (2021).
BTO	N/A	—	358	PLD BTO on $LaAlO_3$-Sr_2TaAlO_6 substrates.	Light: Sci. & Applications 15, 21 (2026)
BTO	No (BTO WG)	22	—	Poly-crystal BTO grown on glass.	Optics Lett. 28 (24), 2527-2529 (2003)
BTO	No (BTO WG)	162	—	RF sputtered BTO with STO buffer layer.	arXiv:2507.17150 (2025)
BTO	No (BTO WG)	300*	—	MBE BTO on Si with engineered STO buffer.	J. Lightwave Technol. 34, 1688 (2016).
BTO	No (BTO WG)	89	—	RF sputter BTO on SOI.	ACS Photonics 10, 4367-4376 (2023).
BTO	Yes (Si–BTO)	950*	1290	vdW integration of freestanding single-crystalline *a*-axis-domain BTO thin-film.	This work
		880*	1190		
LN	Yes (SiN–LN)	—	30.9	Wafer bonding LNOI with SiNOI.	Nature Communications 14, 3499 (2023)
LN	Yes (SiN–LN)	—	30.9	Wafer bonding LNOI with SiNOI.	Optica 10 (5), 578-584 (2023)
LT	Yes (SiN–LT)	—	30*	Wafer bonding LTOI with SiNOI.	Nature 629, 784–790 (2024)
LT	Yes (SiN–LT)	—	30*	Wafer bonding LTOI with SiNOI.	Nature Communications 17, 3314 (2026)

Notes: WG: waveguide. Only in-plane (film-parallel) effective Pockels coefficients $r_{\text{eff}}^{\parallel}$ are marked. Pockels tensor components that are perpendicular to film plane and ineffective to on-chip EO applications are marked out with ⊥ superscript. Detailed explanations are made in Table S1 of the Supplementary Information.

We note that some higher *our-of-plane* Pockels coefficients $r_{\text{eff}}^{\perp}$ were reported before, such as Ref: Nano Letters, 25, 11089-11096 2025, and Ref: Nature, 641, 876-883, 2025, where free-space light was injected perpendicular to the BTO films in measurements. However, these reported $r_{\text{eff}}^{\perp}$, contributed by *c*-axis-domain (i.e. (001) crystal plane orientation) BTO, are ineffective/ largely not useful in integrated photonics, because the light signals are all propagating along the waveguides parallel to the photonic chip plane, leaving $r_{\text{eff}}^{\perp}$ making no effective contribution to the desired on-chip EO modulation. Therefore, only the *in-plane* effective Pockels coefficient is critical for most integrated EO applications.

As benchmarked in Table R3-4 above, the in-plane r_{eff} of our freestanding BTO nanomembranes vdW-integrated EO MZMs is about 1.4 ~ 42 times higher than previous works based on heteroepitaxial or bonded BTO with inevitably compromised crystal quality (Ref: Nature Materials 24, 868-875, 2025; Ref: ACS Photonics 10, 4367-4376, 2023; Ref: Nature 641, 876-883, 2025; Ref: Optics Letters 28, 2527-2529, 2003). The experimental BTO r_{42} in this work is also over 40 times higher than current mainstream EO materials LN[22,23] and LT[9,10,61,62]. Despite that previous endeavors were indeed made to integrate BTO on Si, this drastic performance improvement for BTO in-plane Pockels coefficient r_{eff}, via our novel freestanding nanomembranes-based photonic vdW integration method, will still serve as an important contribution for research in BTO-based integrated EO devices.

• The half-wave voltage-device length product ($V_\pi \cdot L$) is another key performance parameter for EO MZMs. Our devices $V_\pi \cdot L$ remain competitive compared to prior published papers (especially with further enhanced EO bandwidth if compared with similar MZI-structured modulators, as elaborated later), as benchmarked in Table R3-5 below.

Table R3-5. Brief benchmarks the BTO-based EO device performances of this work against prior publications

EO Material	Hybrid waveguide	Structure	$r_{\text{eff}}^{\parallel}$ (pm/V)	$V_\pi \cdot L$ (V·cm)	EO 3dB BW (GHz)	Ref
BTO	Yes (Si–BTO)	Microring	680*	—	30	Nature Materials 18, 42-47 (2019)
BTO	Yes (Si–BTO)	MZI	213	1.5	0.8	Nano Letters 14, 1419-1425 (2014)
		Microring	—	—	4.9	
BTO	Yes (Si–BTO)	Microring	380	—	12*	J. Lightw. Technol. 37, 1456-1462 (2019)
BTO	Yes (Si–BTO)	MZI	48	1.67	—	Light: Adv. Manufact. 5, 479-489 (2025)
BTO	Yes (Si–BTO & SiN-BTO)	Microring MZI	200	— (Ring) 5 (MZI)	~30* (ring) ~20* (MZI)	Nature Materials 19, 1164-1168 (2020)
BTO	Yes (SiN–BTO)	Microring	343	0.3	DC/NA	ACS Photonics 6, 2677-2684 (2019)
BTO	Yes (SiN–BTO)	MZI	360	0.5	DC/NA	J. Opt. Soc. Am. B 22, 240-253 (2005)
BTO	Yes (SiN–BTO)	MZI	38	4.5	DC/NA	IEEE PTL. 16, 1837-1839 (2004)
BTO	Yes (SiN–BTO)	MZI	624*	0.62	6.9	Nature 641, 876-883 (2025)
BTO	No (BTO WG)	MZI	22	5.7	—	Opt. Lett. 28, 2527-2529 (2003)
BTO	No (BTO WG)	MZI	162	0.54	—	arXiv:2507.17150 (2025)
BTO	No (BTO WG)	MZI	150	1.248	3.7	Opt. Express 12, 5962-5967 (2004)
BTO	No (BTO WG)	MZI	89	2.32	~ 5.9*	ACS Photonics 10, 4367-4376 (2023)
	Yes (Si–BTO)	MZI	950*	0.29	DC/NA	This work

BTO This work			880*	1.4	> 23	
LN	Yes (SiN–LN)	MZI	~30*	8.2~8.8	—	Nature Communications 14, 4856 (2023)
LN	No (LN WG)	MZI	~30*	3.67	22	Optics Express 29, 17710–17717 (2021).
LT	Yes (SiN–LT)	MZI	~30*	4.08	> 70*	Nature Communications 17, 3314 (2026)
LT	Yes (SiN–LT)	MZI	~30*	3.5	70*	Nature Photonics 20, 225–231 (2026)

Notes: Superscript * denotes calibration or calculated estimations applied. Entry — represents not reported or studied in the reference. DC/NA denotes only DC or low-frequency characterizations were reported. WG: waveguide. BW: bandwidth. LN: lithium niobate. LT: lithium tantalate. MZI: Mach-Zehnder interferometer. MZM: Mach-Zehnder modulators. Detailed explanations are made in Table S1 of Supplementary Note S12.

(i) As shown in Table R3-5, the experimental $V_\pi \cdot L$ of 0.29 V·cm (measured at 1 kHz frequency, corresponding to device in main text Fig. 2h, with device structure shown as Fig. R3-17a) is among the lowest in previous publications with $V_\pi \cdot L$ ranging from 0.3 ~ 1.67 V·cm, if comparing with other similar hybrid EO waveguides (i.e. EO materials coupled with Si or SiN waveguides).

(ii) For high-speed EO modulators (corresponding to main text Figs. 2i~2k, device structure illustrated as Fig. R3-17b below), the experimentally measured device $V_\pi \cdot L$ and EO 3 dB bandwidth for our BTO MZM are 1.4 V·cm and 23 GHz respectively. Even though we have deliberately sacrificed the device $V_\pi \cdot L$ to trade for higher MZM EO bandwidth (detailed in Supplementary Note S10 and will be elaborated later on Page 67 of this Response Letter), this 1.4 V·cm of our BTO MZM $V_\pi \cdot L$ is still comparable to or better than many previous publications based on BTO (Table R3-5).

For example, in Ref: Nature Materials 19, 1164-1168 (2020), the reported $V_\pi \cdot L$ is over 5 V·cm for the BTO MZM (with a big driving voltage ~ 50 V), which is much higher than our work; in Ref: ACS Photonics 10, 4367-4376 (2023), the experimental $V_\pi \cdot L$ is 2.32 V·cm with a low EO 3 dB bandwidth around 5.9 GHz (ours is over 23 GHz).

Specifically, our device $V_\pi \cdot L$ exhibits clearer advantages when compared to prior works using lithium niobate (LN)- or lithium tantalate (LT)-based *hybrid-waveguide* MZMs (Table R3-5). For example, for previous LN hetero-integrated SiN MZMs, the reported $V_\pi \cdot L$ over 8.2 V·cm (Ref: Nature Communications 14, 4856, 2023), is about 6 times higher than our work (1.4 V·cm). For the very recent papers utilizing transferred LT films, the reported $V_\pi \cdot L$ values are 4.08 V·cm for Ref[9]: Nature Communications 17, 3314 (2026), and 3.5 V·cm for Ref[10]: Nature Photonics 20, 225–231 (2026) (micro-transfer of LN films etched and lifted off from LNOI wafers).

(iii) $V_\pi \cdot L$ is also highly dependent on device structure and configurations, with varying pros and cons for different device configurations: Specifically, the portion of the optical power inside the EO material (i.e. the optical field overlap factor Γ) to facilitate EO modulation, and distance between the electrodes g has big impact.

In this work, we selected hybrid waveguide configurations (i.e. functional materials coupled to Si or SiN waveguides core), because we aim to demonstrate the concept of infusing arbitrary desired optical functionalities to established photonic platforms by selecting the single-crystalline freestanding 3D vdW building blocks, to realize unbounded photonic heterogeneous integration on arbitrary substrates with highest available material quality. People may comment that the $V_\pi \cdot L$ for devices with non-hybrid waveguide structures (i.e. patterned EO material directly as waveguide core) can be comparatively lower. This indeed makes sense as non-hybrid EO waveguide configurations (e.g. LNOI, LTOI, and lithographic BTO waveguides) have intrinsically higher optical field overlap factor Γ than hybrid waveguides. However, for direct BTO waveguide case, there is still no satisfactory solution so far, due to the outstanding heteroepitaxy barriers limiting BTO layer quality[28,34], exhibiting largely compromised BTO effective

Pockels coefficients r_{eff} (only 20 ~ 300 pm/V, as discussed in Table R3-4 above, which is about 3~48 times lower than this work). Furthermore, the vdW integration approach of BTO studied in this work circumvents the lengthy optimization of BTO dry etching, which has similar redeposition issues like LT and LT necessitating stringent etched waveguide side-wall roughness requirements. More importantly, these hybrid waveguide structures selected in this work can leverage the maturity and high robustness of established Si and silicon nitride (SiN) photonics platforms. For example, despite the availability of LNOI and LTOI platforms already, bonded LN and LT to Si and SiN photonics are still a preferable option in both academia and industry with competitive performances and broad impact (e.g. bonded LN to SiN Ref: Nature Commun. 14, 4856, 2023) and LT (by wafer LT wafer bonding, Ref: Nature Communications 17, 3314, 2026; or micro-transfer of BOE lifted-off LT films from LTOI wafers, Ref: Nature Photonics 20, 225–231, 2026).

If only perusing lower driven voltage, we have performed supplementary simulations showing that the $V_{\pi} \cdot L$ of our current BTO MZM devices can be further reduced to 0.13 V·cm (Fig. R3-17d) and 0.97 V·cm (Fig. R3-17c) for MZM device structures of Design B and Design A respectively, by altering the electrodes gap distance g to 2 μm and 3 μm respectively, at the cost of drastically reduced 3 dB EO bandwidth and increased optical loss (detailed in Supplementary Note S10, and revised Fig. S19).

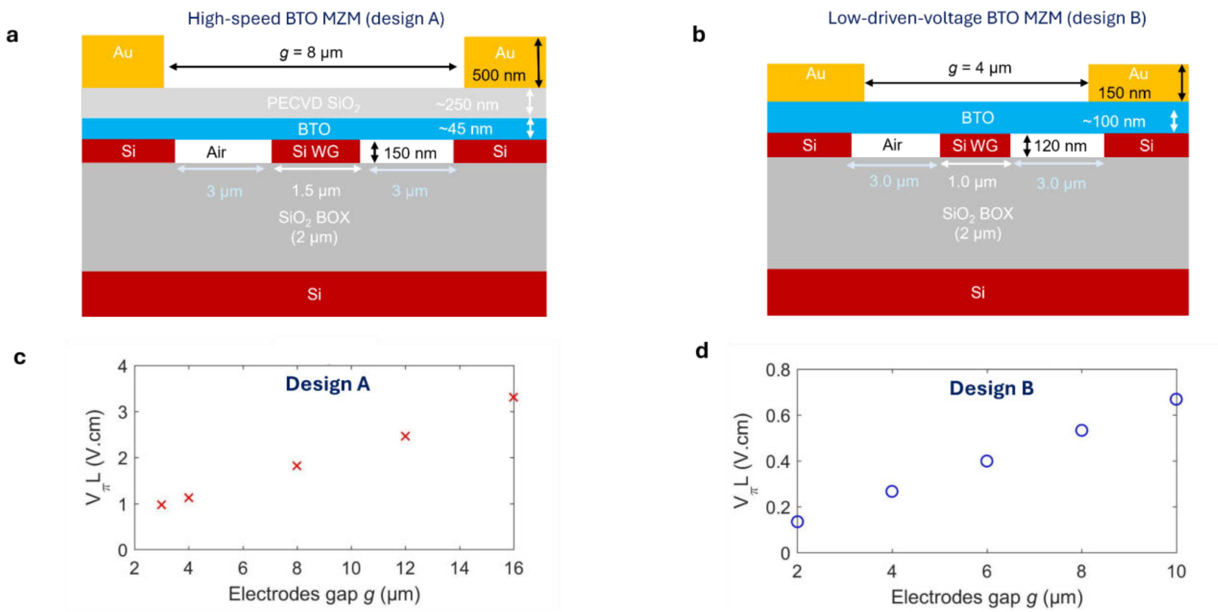

Fig. R3-17. (a) Device structure schematics (namely design A) corresponding to the high-speed BTO MZM shown in Fig. 2k in manuscript main text. (b) Device structure schematics (namely design B) for the low-voltage BTO MZM shown in main text Fig. 2h. (c) and (d) Device half-wave voltage-length product $V_{\pi} \cdot L$ as a function of electrodes gap distance g of different device structures shown in (a) and (b), respectively.

• The 23 GHz EO 3 dB bandwidth of the BTO MZMs realized in this work is among the highest, if compared to previous similar works based on Mach-Zehnder interferometer (MZI) structures.

We note that though some higher EO bandwidths were reported (as Table R3-5 above), they are based on micro-ring resonator structures, which has significantly narrower optical operation spectrum and high sensitivity to ambient temperature due to its resonance tuning nature for operation. So far, the mainstream EO modulation solutions are still based on MZI structures, with much wider applications than micro-rings.

The majority of previous papers on BTO-based MZMs show quite low EO bandwidth (Table R3-5), due to the mismatched Z_0 and group velocities in EO modulation, given the high BTO microwave permittivity in RF frequencies (discussed in Supplementary Note S10). For instance, in Ref: Nature 641, 876-883 (2025), and Ref: Ref: ACS Photonics 10, 4367-4376 (2023), the reported BTO MZM 3 dB EO bandwidths are only 6.9 GHz and 5.9 GHz respectively. Our experimental 23 GHz 3 dB EO bandwidth remains an evident improvement than those prior similar works, despite still limited by non-ideal device traveling wave electrodes fabrication towards further improvement (Supplementary Notes S15). This is achieved by trading device $V_{\pi}\cdot L$ for higher EO bandwidth for our BTO MZMs in this work: by using a thinner BTO film and introducing a thick SiO_2 buffer layer between the electrodes and BTO layer (Fig. R3-17a, in order to reduce device microwave impedance Z_0 and for better velocity matching of travelling wave electrodes).

• In summary, the *in-plane* effective Pockels coefficient r_{eff}, which is crucial for integrated photonic applications, of the BTO MZMs demonstrated in this work (Table R3-4) remains record-setting to the best of our knowledge. The 0.29 V·cm $V_{\pi}\cdot L$ of the low-speed BTO MZM is also among the lowest against major prior published works (Table R3-5). For high-speed BTO MZMs, we selected a balanced $V_{\pi}\cdot L$ of 1.4 V·cm to trade for a 23 GHz EO 3 dB bandwidth, which is also among the highest (BTO MZM EO bandwidth) compared to previous BTO MZMs with similar device configurations.

Actions taken:

We have further carefully discussed the design trade-offs, and the comprehensive benchmarks of the BTO MZMs device performances in this work in revised Supplementary Notes S10 and S12 (on Page 18 and Page 23 of the Supplementary Information), respectively.

(1.2) For CFO-integrated MO isolators, the performances of the devices in this work are benchmarked as Table R3-6 below, including core device performance metrics of non-reciprocal phase shift (NRPS), effective MO waveguide length L_{MO}, optical losses, and Faraday rotation coefficient θ_F.

Table R3-6. Brief performance benchmarks of non-reciprocal CFO devices in this work against prior publications

MO Material	θ_F (°/cm)	α_m (dB/cm)	α_{wg} (dB/cm)	NRPS (mm^{-1})	L_{MO} (mm)	Notes on material preparations	Ref
Ce:YIG	-1500	—	—	1.9*	0.85*	Sputtered Ce: YIG on Si with YIG buffer.	Optica 6, 473-478 (2019)
Ce:YIG	-3000	—	31.9	0.55*	5.6*	Wafer bonding of Ce:YIG to SOI ring.	Opt. Exp. 19, 11740-11745 (2011)
Ce:YIG	-3200	60*	6.3*	0.79*	2*	Wafer bonding of Ce:YIG film to SOI.	Appl. Phys. Lett. 92, 071117 (2008)
Ce:YIG	−5900	137*	31.7	1.57*	1*	PLD Ce:YIG on SiN with YIG buffer layer.	Optica 7, 1555-1562 (2020)
Ce:YIG	-4000	—	14.5	0.98*	0.92*	Wafer bonding of Ce: YIG dies.	Opt. Exp. 20, 1839-1848 (2012)
Ce:YIG	−1263	—	—	0.63*	0.2*	PLD poly-crystal Ce: YIG on Si.	Nature Photon. 5, 758-762 (2011)
Ce:YIG	-3500	—	13	0.5*	0.22*	Wafer bonding of Ce:YIG/GGG to Si chip.	Nature Electron. 5, 604-610 (2022)
YIG	120	60*	—	—	—	RF sputtered poly-crystal YIG.	Journal of Materials Chemistry C 13, 12628-12649 (2025)
Bi:YIG	−1200	200*	50*	—	—	RF sputtered poly-crystal Bi: YIG on Si.	
Ce:TbIG	−3200	—	15*	—	—	Sputtered Ce:TbIG on Si.	ACS Photon. 6, 2455–2461 (2019)
CAFO	12000	8300	—	—	—	RF sputtered CAFO with buffer layers.	Optica 11, 889-895 (2024)
CFO	25600	34000	—	—	—	Sputtered poly-CFO on Si.	Appl. Phys. Exp. 13, 062002 (2020)
CFO	15500	—	210*	3.6*	0.04*	Sputtered poly-CFO on Si.	IEICE Exp. 19, 20210500 (2022)
γ-Fe_2O_3	25000	350000*	—	—	—	—	Materials 6, 5094-5117 (2013)
This work (CFO)	33800	5400*	9*	4.7*	0.026	vdW integration of single-crystalline CFO.	This work

Notes: MO: Magneto-optical. θ_F: Faraday rotation coefficient. α_m: material absorption loss. α_{wg}: the estimated device propagation loss for the MO waveguide. Data are shown around the telecom (1550 nm) wavelengths. NRPS: non-reciprocal phase shift (based on calculation estimation), unit: rad/mm (i.e. mm^{-1}). L_{MO}: length of the MO material on waveguide. YIG: yttrium iron garnet ($Y_3Fe_5O_{12}$), TbIG: terbium iron garnet ($Tb_3Fe_5O_{12}$), CFO: cobalt ferrite ($CoFe_2O_4$), CAFO: aluminum-substituted cobalt ferrite ($CoAl_xFe_{2-x}O_4$), GGG: gadolinium gallium garnet ($Gd_3Ga_5O_{12}$), STO strontium titanate ($SrTiO_3$). Estimated Faraday rotation values are marked with * superscript. Not reported values are marked by — symbol. Detailed explanations are made in Supplementary Note S24 in Supplementary Information.

• As shown in Table R3-6 above, we have realized a big NRPS in an ultrashort MO waveguide length L_{MO} of only 26 μm (corresponding to device in main text Fig. 4c), which remains competitive compared to previous publications based on CFO (direct heteroepitaxy on Si) and garnets like YIG or Ce: YIG (using heteroepitaxy or wafer bonding).

• This is made possible thanks to the giant Faraday rotation coefficient θ_F (~33,800 °/cm) preserved from the single-crystalline freestanding CFO nanomembranes for vdW integration, which is also record-high compared to previous works to the best of our knowledge. We note that some opaque metal-based magnetic materials (such as NdFeB and CoFeB as benchmarked in Table R3-2 in prior response) may indeed have larger θ_F, but their losses are too high to realize any integrated photonic applications.

• Besides, eliminating the lattice mismatching constraints, our CFO oxide films also show much improved optical loss compared to previous CFO-based works (all relying on heteroepitaxy/sputtered CFO on Si), thanks to the high crystal quality and smooth film morphology in this work to mitigate the prominent optical scattering loss from the high film defects in previous references (as compared in Fig. R3-18 below).

For other device performance parameters, such as extinction ratio (>18 dB), it also remains competitive and sufficient for integrated photonic applications. Detailed discussions are made in updated Supplementary Note S24.

[Redacted figure and text below]

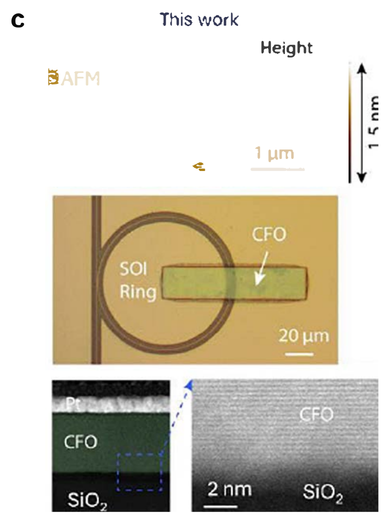

Fig. R3-18. Comparison of CFO quality to previous work.

(c) vdW-integrated single-crystalline CFO film in this work with high-quality and uniform smooth film morphology. Top panels: device optical micrographs. Bottom panels: cross-sectional SEM or TEM.

(1.3) For III-V nanomembranes-integrated SiN photodetectors, their device performance merits are comparable to state-of-the art integrated photodetectors based on waveguide-coupled structures. Specifically, by vdW co-integrating freestanding GaAs and GaN single-crystalline nanomembranes on the single SiN photonic chip, extended wide spectrum photodetection from 405 nm (UV) to 780 nm (NIR) is experimentally demonstrated, which surpasses previous similar works. Detailed benchmarks are discussed in updated Supplementary Note S19 on Page 33 of the Supplementary Information.

(1.4) In summary, despite that the heterogeneous integration of BTO, CFO, and III-V materials on Si and SiN photonics were explored in previous works, the distinctive photonic vdW integration method proposed in this work have realized competitive hetero-integrated photonic devices that, despite proof-of-concept demonstrations, have comparable or competitive device performances (some device parameters are proven record-high to the best of our knowledge) to previous publications with similar device structure configurations.

(2) Clarifications on the novelty: Besides competitive device performances, the key novelty of this work is summarized as below in three folds.

(2.1) In freestanding single-crystalline nanomembranes preparation, the innovation includes both fundamental thin-film growth engineering and layer exfoliation for van der Waals (vdW) integration.

• For example, in thin-films growth, the ability to simultaneously and precisely control the crystallinity quality and crystallographic orientations is crucial for various functional materials, such as the Pockels response of EO material barium titanate (BTO), leading to significant distinctions on material and device performance. In previous research, dramatic variations exist in the reported effective Pockels coefficient r_{eff} of BTO, ranging from merely 22 pm/V (Ref.[1]) to approaching over 600 pm/V (Refs.[2,3]), as briefly benchmarked in Table R3-4 above (also detailed in Supplementary Note S12).

The core reason for these drastic variations of BTO r_{eff} in previous works lies in the BTO crystal quality and its crystallographic orientation.

Firstly, for BTO grown with poor crystal quality (such sputtered BTO in various lattice-mismatched substrates), its EO response is largely deteriorated compared to bulk crystal. For poor polycrystalline BTO, its effective Pockels coefficient can be even lower than lithium niobate (LN) or even negligible for amorphous BTO (Ref: Nature Communications 4, 1671, 2013).

Secondly, even for single-crystalline BTO, its crystallographic orientation still plays a crucial role in affecting the overall EO performance. As the EO Pockels effect is highly dependent on the construction of the 3-order Pockels tensor $\mathbf{r}_{\text{BTO}}$ and the vectorial orientations of the light polarization, radio frequency (RF) electric field $\mathbf{E}_{\text{RF}} = [E_x^{\text{RF}}, E_y^{\text{RF}}, E_z^{\text{RF}}]^T$, and the crystallographic orientation of the BTO c-axis[4],

$$\Delta\boldsymbol{\eta}_{\text{BTO}} = \begin{bmatrix} \Delta(1/n^2)_1 \\ \Delta(1/n^2)_2 \\ \Delta(1/n^2)_3 \\ \Delta(1/n^2)_4 \\ \Delta(1/n^2)_5 \\ \Delta(1/n^2)_6 \end{bmatrix} = \mathbf{r}_{\text{EO}} \cdot \mathbf{E}_{\text{RF}} = \begin{bmatrix} 0 & 0 & r_{13} \\ 0 & 0 & r_{13} \\ 0 & 0 & r_{33} \\ 0 & r_{42} & 0 \\ r_{42} & 0 & 0 \\ 0 & 0 & 0 \end{bmatrix} \begin{bmatrix} E_x^{\text{RF}} \\ E_y^{\text{RF}} \\ E_z^{\text{RF}} \end{bmatrix}$$

where $\Delta\boldsymbol{\eta}_{\text{BTO}}$ is the impermeability tensor describes the refractive index change of BTO under the EO modulation of applied electric field $\mathbf{E}_{\text{RF}}$, and the specific expression of $\mathbf{r}_{\text{BTO}}$ relies on device design and the judicious arrangement of BTO crystal c-axis (Supplementary Note S7, and Fig. S14). For BTO bulk crystal, its Pockels tensor components have very big distinctions in numerical values: r_{13}~20 pm/V, r_{33}~100 pm/V, r_{42}~1600 pm/V (Ref: R. W. Boyd, Nonlinear Optics, 511-523 Springer, 2008. Ref: Nature Materials 19, 1164-1168, 2020). Consequently, if the crystallographic orientation of BTO is not judiciously controlled, other Pockels components are probed instead of the biggest tensor component r_{42}, which will lead to dramatically decreased EO response — almost 100 times variation can exist in the measured effective Pockels coefficient r_{eff}.

Thus, in this work we have thoroughly addressed this vital hurdle via a distinctive strategy of vdW integration, by creating freestanding single-crystalline BTO nanomembranes with carefully-engineered crystal orientations in optimal lattice-matched parent substrates and then get transferred to photonic templates for heterogeneous photonic integration, instead of direct heteroepitaxy used most prior references (fundamentally limited by epitaxial lattice-matching requirements). As a result, we have experimentally demonstrated record-setting BTO *in-plane* effective Pockels coefficient r_{eff} about 950 pm/V, corresponding to a giant EO Pockels tensor component r_{42} of 1290 pm/V, which are the highest values reported so far in integrated photonics to the best of our knowledge.

Thirdly, we applied a distinct heterogeneous integration method of BTO than previous works. Taking the example of currently reported BTO hetero-integrations (layer bonding used): crystalline BTO is first deposited on attentively engineered thin STO buffer layer grown and annealed by molecular beam epitaxy (MBE) on Si, followed by oxides (e.g. Al_2O_3) mediated BTO layer bonding and complex substrate grinding, etching, and polishing processes (Ref: Nature Materials 18, 42–47, 2019; Ref: Nature Materials 19, 1164-1168, 2020) before a device can be made.

In contrast, in this work our freestanding nanomembranes-based vdW integration strategy is a universal method applicable to arbitrary desired functional optical materials and arbitrary optical substrates, in a fast, cost-saving (detailed in Supplementary Note S27), convenient-to-implement, and with approaching atomic-level precision on the resultant integrated optical layer thickness. It does not require the complex ion implantation slicing or the time-consuming substrate grinding and polishing procedures indispensable in the abovementioned approaches to get the functional optical layer transferred. Our proposed freestanding nanomembrane-based vdW integration method thus exhibits great versatility and ultrahigh degrees of freedom in unlocking novel photonic heterogeneous integration structures and new multifunctional applications. Specifically, we realized well-controlled a-axis-domain BTO vital for integrated EO photonics.

• Systematic studies are also made on ultraefficient magneto-optical (MO) material cobalt ferrite (CFO), which attracts comparatively less attention before than garnets.

This work remains the first demonstration of single-crystalline CFO thin-film based non-reciprocal integrated photonic devices via layer transfer to the best of our knowledge, with giant Faraday rotation coefficient θ_F over 33,800 °/cm, which is about 100 times higher than current mainstream MO material YIG, and 8~10 times higher than Ce: YIG (e.g., Ref: Nature Electronics 5, 604–610, 2022; Ref: Nature Photonics 5, 758-762, 2011), setting a positive reference for developing future ultracompact and high-efficiency non-reciprocal optical applications.

Besides, compared with previous approaches relying on direct heteroepitaxy of CFO on Si, we have vastly promoted the crystal quality of the functional CFO films with largely enhanced material quality and suppressed scattering loss from film defects (Supplementary Note S24). Specifically, the large coercive field of CFO (as a hard ferromagnet) enables on-chip non-reciprocal transmission without external magnets after proper magnetization, which is not possible by using garnets (soft magnetic materials)-based photonic devices.

• The synthesis of other high-quality nanomembranes such as group III-V semiconductors GaAs and GaN with significantly reduced film defects for heterogeneous integrated photonic applications.

(2.2) For functional optical layer transfer, this work will establish a comprehensive framework for freestanding 3D nanomembranes-based photonic heterogeneous integration strategy with verified experimental feasibility and unique strengths.

In this work, we explicitly demonstrated the critical benefits of single-crystalline freestanding nanomembranes. Both the single-crystalline film quality and its freestanding form with artificially laminated vdW interfaces are the two keys for enabling boundless and high-performance photonic heterogeneous integrations reported in this work.

By contrast, in current mainstream photonic heterogeneous integration approaches, such as heteroepitaxy or wafer bonding, the formation and integration of freestanding 3D nanomembranes were not virtually existing or were not clearly elucidated with careful attention for its unique advantages in realizing high-quality functional optical layers with high device performance. This vdW integration concept so far is still largely restricted to 2D materials research communities, as the creation and handling of 3D freestanding nanomembranes with high crystallinity and well-preserved optical functionality to their bulk counterparts is still in its early stages of study.

This work thus establishes a comprehensive baseline for the vdW integration of 3D freestanding films, covering freestanding nanomembranes synthesis, lift-off, integration, and device design and implementation, to embody a very promising alternative pathway towards novel and versatile photonic heterogeneous integration.

(2.3) For device implementations, this work remains the first systematic demonstration on the vdW integration of multiple functional freestanding 3D single-crystal films for hetero-integrated photonics, to the best of our knowledge, with experimentally verified superior, or comparable performance to state-of-the-art devices with similar configurations showing unique advantages (as discussed above).

(3) Justifications on the fit for Nature and its further impact: In summary, the different functional material systems, their freestanding nanomembranes, and corresponding hetero-integrated devices all together, are indispensable components underpinning the unified core concept of the versatile photonic vdW integration platform demonstrated in this work with unique advantages inaccessible via conventional approaches.

• Besides the novelty and technical advancements on single-crystalline freestanding 3D nanomembranes preparation and advantageous device implementations already discussed above, this manuscript can serve as the first comprehensive framework on the vdW integration of diverse freestanding 3D nanomembranes for heterogeneous integrated photonics, to the best of our knowledge. Fundamental optical functionalities, including EO modulation (via freestanding BTO films), MO isolation (via CFO and YIG films), photodetection (via GaAs and GaN films, potential for also light emissions), are systematically demonstrated this work for integrated photonics.

• We also highlighted the crucial role of freestanding single-crystal 3D nanomembranes: both the freestanding form of these 3D films with artificially delaminated vdW interfaces and the single-crystal thin-film quality are key to enabling future advanced hetero-integrated photonic applications. Armed with these single-crystalline '3D Lego bricks', we can harvest the most favorable functionalities from multiple dissimilar material platforms on arbitrary optical substrates with low-cost and unprecedented freedom[25,39] for advancing heterogeneous integrated photonics. Desired optical functionality can be infused to established photonic platforms such as Si and SiN photonics by selecting these desired '3D Lego bricks' with record-setting optimal material quality.

• This work also validates the feasibility of creating artificial 3D heterostructures (such as the GaAs/BTO/GaN/STO stack in Supplementary Fig. S10 with various functional materials) with all single-crystalline quality but drastically distinct crystal structures, which can be hardly made possible via conventional heteroepitaxial approaches. This capability can find value especially in 3D photonic integration[13,14,52,55] (Ref: Nature 620, 78-85, 2023; Ref: Nature 614, 81-87, 2023) towards ultracompact and unparalleled multifunctional integrated photonic systems and circuities. Proof-of-concept multifunctional EO and MO modulators (for vertically stacked CFO and BTO films on SOI chip), and expanded wide-spectrum photodetectors (for laterally stitched GaAs and GaN films on SiN chip) are also demonstrated to embody this concept. Broad opportunities still exist on using the proposed photonic vdW integration to prototype exotic heterogeneous photonic layouts with various specific devices or systems functions, yet it has passed beyond the scope of this work targeting the photonic vdW integration platform demonstration.

• Lastly, these 3D freestanding nanomembrane building blocks demonstrated in this work can further extend the concept of van der Waals (vdW) heterostructures beyond 2D materials, and advance nanomembrane technologies (Ref: Nature 641, 98-105, 2025; Ref: Science 383, 388-394, 2024). A viable playground also unfolds to study the coupling of diverse single-crystalline 3D nanomembranes in fundamental physics from 2D heterostructures to 2D/3D (Ref: Science 384, 312-317, 2024), 3D/3D (Ref: Nature 626, 529-534, 2024; Ref: Nature Nanotechnology 20, 881-888, 2025), and beyond, without necessitating expensive facilities or lengthy process engineering.

Actions taken:

We have carefully revised our manuscript and further highlighted the novelty and impact in revised main text introduction and conclusion, as well as in Supplementary Note S27 (on Page 41, highlighted in yellow, shown below).

We greatly appreciate all the constructive comments by the reviewer that help us enhance our manuscript. With the careful revisions and clarifications made, we sincerely believe this work will have justified novelty and sufficient technical advances to be published on Nature, as a comprehensive framework for the versatile photonic vdW integration platform, encompassing ultrahigh thin-film material quality, competitive device performance, and technical key points on device implementation, with broad potential impact from nanomaterials community to heterogeneous integrated photonics.

> This work can serve as a comprehensive baseline on leveraging the versatile vdW integration platform for realizing various heterogeneous integrated photonic applications, with diverse functional freestanding 3D nanomembranes, covering thin film epitaxy, lift off, and device implementations with verified unique advantages. Both the single-crystalline film quality (with well-defined crystallographic orientations) and its freestanding form with artificially laminated vdW interfaces are the two keys for enabling boundless and high-performance photonic heterogeneous integrations reported in this work. We thus highlight the critical role of creating and integrating these freestanding 3D single-crystalline films in photonics, which were not clearly elucidated with careful attention in conventional hetero-integration strategies such as direct heteroepitaxy or wafer bonding. New opportunities await in further leveraging the versatile photonic vdW integration platform to develop 3D photonic integration[44] with ultracompact footprint and unparalleled multifunctionality[1,45,165,166]. An intriguing playground thus unfolds to coalesce various functional optical layers with optimal single-crystallinity but distinct crystal structures that are hardly accessible via direct heteroepitaxial approaches, permitting emerging opportunities for heterogeneous photonic integration[1,2,15,25] and nanomembranes-related physics and technologies[7,18,19,46-49,167-169].

Responses to Referee 4:

Comment:

I co-reviewed this manuscript with one of the reviewers who provided the listed reports.

Response:

We sincerely appreciate the reviewer on the careful assessment of our manuscript and the constructive suggestions.

We have thus carefully revised our manuscript accordingly, supplementing additional experiments verifying the high crystal quality and low defect densities of our freestanding 3D photonic nanomembranes, explicit device dark current measurements, and related numerical simulations illustrating the practical considerations and trade-offs in device design. Comprehensive benchmarks on the device performances to prior works are also performed, with detailed justifications highlighting the novelty and extended impact of this work for publication.

References for Reviewer 3 and Reviewer 4

1 Petraru, A., Schubert, J., Schmid, M., Trithaveesak, O. & Buchal, C. Integrated optical Mach Zehnder modulator based on polycrystalline BaTiO3. *Optics Letters* **28**, 2527-2529 (2003).

2 Abel, S. *et al.* Large Pockels effect in micro-and nanostructured barium titanate integrated on silicon. *Nature Materials* **18**, 42-47 (2019).

3 Alexander, K. *et al.* A manufacturable platform for photonic quantum computing. *Nature* **641**, 876-883 (2025).

4 Boyd, R. W. in *Nonlinear Optics* 511-523 (Springer, 2008).

5 Han, S. *et al.* High energy density in artificial heterostructures through relaxation time modulation. *Science* **384**, 312-317 (2024).

6 Mengxue, T. *et al.* Towards high quality transferred barium titanate ferroelectric hybrid integrated modulator on silicon. *Light: Advanced Manufacturing* **5**, 479-489 (2024).

7 Kim, H. *et al.* High-throughput manufacturing of epitaxial membranes from a single wafer by 2D materials-based layer transfer process. *Nature Nanotechnology* **18**, 464-470 (2023).

8 Bae, S.-H. *et al.* Graphene-assisted spontaneous relaxation towards dislocation-free heteroepitaxy. *Nature Nanotechnology* **15**, 272-276 (2020).

9 Cai, J. *et al.* Heterogeneously integrated lithium tantalate-on-silicon nitride modulators for high-speed communications. *Nature Communications* **17**, 3314 (2026).

10 Niels, M. *et al.* A high-speed heterogeneous lithium tantalate silicon photonics platform. *Nature Photonics* **20**, 225-231 (2026).

11 Sato, K., Okano, M. & Shoji, Y. Ultra-compact microring optical isolator using an aluminum-substituted cobalt ferrite thin film. *Optica* **11**, 889-895 (2024).

12 Serrano-Núñez, M. A., Shoji, Y. & Mizumoto, T. Small magnetless integrated optical isolator using a magnetized cobalt ferrite film. *IEICE Electronics Express* **19**, 20210500-20210500 (2022).

13 Xiang, C. *et al.* 3D integration enables ultralow-noise isolator-free lasers in silicon photonics. *Nature* **620**, 78-85 (2023).

14 Daudlin, S. *et al.* Three-dimensional photonic integration for ultra-low-energy, high-bandwidth interchip data links. *Nature Photonics* **19**, 502-509 (2025).

15 Wan, Y. *et al.* Integrating silicon photonics with complementary metal–oxide–semiconductor technologies. *Nature Reviews Electrical Engineering* **3**, 15-31 (2026).
16 Chelladurai, D. *et al.* Barium titanate and lithium niobate permittivity and Pockels coefficients from megahertz to sub-terahertz frequencies. *Nature Materials* **24**, 868-875 (2025).
17 Masubuchi, S. *et al.* Autonomous robotic searching and assembly of two-dimensional crystals to build van der Waals superlattices. *Nature Communications* **9**, 1413 (2018).
18 Chen, L. *et al.* Fully automatic transfer and measurement system for structural superlubric materials. *Nature Communications* **14**, 6323 (2023).
19 Nakatani, M. *et al.* Ready-to-transfer two-dimensional materials using tunable adhesive force tapes. *Nature Electronics* **7**, 119-130 (2024).
20 Zhao, Y. *et al.* Large-area transfer of two-dimensional materials free of cracks, contamination and wrinkles via controllable conformal contact. *Nature Communications* **13**, 4409 (2022).
21 Wen, Y., Chen, H., Wu, Z., Li, W. & Zhang, Y. Fabrication and photonic applications of Si-integrated LiNbO3 and BaTiO3 ferroelectric thin films. *APL Materials* **12**, 020601 (2024).
22 Zhu, D. *et al.* Integrated photonics on thin-film lithium niobate. *Advances in Optics and Photonics* **13**, 242-352 (2021).
23 Hu, Y. *et al.* Integrated electro-optics on thin-film lithium niobate. *Nature Reviews Physics* **7**, 237-254 (2025).
24 Baets, R. & Rahim, A. Heterogeneous integration in silicon photonics: opportunities and challenges: opinion. *Optical Materials Express* **13**, 3439-3444 (2023).
25 Kaur, P. *et al.* Hybrid and heterogeneous photonic integration. *APL Photonics* **6**, 061102 (2021).
26 Ramirez, J. M. *et al.* III-V-on-Silicon Integration: From Hybrid Devices to Heterogeneous Photonic Integrated Circuits. *IEEE Journal of Selected Topics in Quantum Electronics* **26**, 1-13 (2020).
27 Ortmann, J. E. *et al.* Ultra-Low-Power Tuning in Hybrid Barium Titanate–Silicon Nitride Electro-optic Devices on Silicon. *ACS Photonics* **6**, 2677-2684 (2019).
28 Eltes, F. *et al.* A BaTiO3-Based Electro-Optic Pockels Modulator Monolithically Integrated on an Advanced Silicon Photonics Platform. *J. Lightwave Technol.* **37**, 1456-1462 (2019).
29 Eltes, F. *et al.* Low-loss BaTiO3–Si waveguides for nonlinear integrated photonics. *ACS Photonics* **3**, 1698-1703 (2016).
30 Xiong, C. *et al.* Active silicon integrated nanophotonics: ferroelectric BaTiO3 devices. *Nano Letters* **14**, 1419-1425 (2014).
31 Eltes, F. *et al.* An integrated optical modulator operating at cryogenic temperatures. *Nature Materials* **19**, 1164-1168 (2020).
32 Kim, G. I., Yim, J. & Bahl, G. J. a. p. a. Low loss monolithic barium titanate on insulator integrated photonics with intrinsic quality factor> 1 million. (2025).
33 Jacob, B. *et al.* Surface Passivation of III–V GaAs Nanopillars by Low-Frequency Plasma Deposition of Silicon Nitride for Active Nanophotonic Devices. *ACS Applied Electronic Materials* **4**, 3399-3410 (2022).
34 Karvounis, A., Timpu, F., Vogler-Neuling, V. V., Savo, R. & Grange, R. BaTiO3: Barium Titanate Nanostructures and Thin Films for Photonics *Advanced Optical Materials* **8**, 2070094 (2020).
35 Abel, S. *et al.* A strong electro-optically active lead-free ferroelectric integrated on silicon. *Nature Communications* **4**, 1671 (2013).
36 Winiger, J. *et al.* PLD Epitaxial Thin-Film BaTiO3 on MgO − Dielectric and Electro-Optic Properties. *Advanced Materials Interfaces* **11**, 2300665 (2024).
37 Chu, Y.-H. Van der Waals oxide heteroepitaxy. *npj Quantum Materials* **2**, 1-5 (2017).
38 MacManus-Driscoll, J. L. *et al.* Strain control and spontaneous phase ordering in vertical nanocomposite heteroepitaxial thin films. *Nature Materials* **7**, 314-320 (2008).
39 Liu, Y., Huang, Y. & Duan, X. Van der Waals integration before and beyond two-dimensional materials. *Nature* **567**, 323-333 (2019).

40 Yang, X. *et al.* Highly reproducible van der Waals integration of two-dimensional electronics on the wafer scale. *Nature Nanotechnology* **18**, 471-478 (2023).
41 Kong, L. *et al.* Wafer-scale and universal van der Waals metal semiconductor contact. *Nature Communications* **14**, 1014 (2023).
42 Pecunia, V. *et al.* Guidelines for accurate evaluation of photodetectors based on emerging semiconductor technologies. *Nature Photonics* **19**, 1178-1188 (2025).
43 Tran, M. *et al.* Extending the spectrum of fully integrated photonics. *Nature* **610**, 54–60 (2022).
44 Loft, J. C. *et al.* Visible light propagation loss of LPCVD Si3N4 thin films and waveguides: impact of high-temperature annealing. *Optics Letters* **51**, 2332-2335 (2026).
45 Bi, L. *et al.* On-chip optical isolation in monolithically integrated non-reciprocal optical resonators. *Nature Photonics* **5**, 758-762 (2011).
46 Pintus, P. *et al.* Integrated non-reciprocal magneto-optics with ultra-high endurance for photonic in-memory computing. *Nature Photonics* **19**, 54-62 (2025).
47 Minemura, D. *et al.* Compact magneto-optical isolator by μ-transfer printing of magneto-optical single-crystal film on silicon waveguides. *Optics Express* **31**, 27821-27829 (2023).
48 Dötsch, H. *et al.* Applications of magneto-optical waveguides in integrated optics: review. *J. Opt. Soc. Am. B* **22**, 240-253 (2005).
49 Yan, W. *et al.* On-Chip Nonreciprocal Photonic Devices Based on Hybrid Integration of Magneto-Optical Garnet Thin Films on Silicon. *IEEE Journal of Selected Topics in Quantum Electronics* **28**, 1-15 (2022).
50 Wei, Z. *et al.* Recent development of magneto-optical thin films and integrated photonic devices. *Journal of Materials Chemistry C* **13**, 12628-12649 (2025).
51 Erdem, D. *et al.* CoFe2O4 and CoFe2O4-SiO2 Nanoparticle Thin Films with Perpendicular Magnetic Anisotropy for Magnetic and Magneto-Optical Applications. *Advanced Functional Materials* **26**, 1954-1963 (2016).
52 Shin, J. *et al.* Vertical full-colour micro-LEDs via 2D materials-based layer transfer. *Nature* **614**, 81-87 (2023).
53 Liu, S., Shoji, Y. & Mizumoto, T. TE-mode magneto-optical isolator based on an asymmetric microring resonator under a unidirectional magnetic field. *Optics Express* **30**, 9934-9943 (2022).
54 Carvalho, W. O. F. & Mejía-Salazar, J. R. Magneto-optical micro-ring resonators for dynamic tuning of add/drop channels in dense wavelength division multiplexing applications. *Optics Letters* **46**, 2396-2399 (2021).
55 Xiang, C. & Bowers, J. E. Building 3D integrated circuits with electronics and photonics. *Nature Electronics* **7**, 422-424 (2024).
56 Feng, H. *et al.* Integrated lithium niobate microwave photonic processing engine. *Nature* **627**, 80-87 (2024).
57 Yu, M. *et al.* Integrated femtosecond pulse generator on thin-film lithium niobate. *Nature* **612**, 252-258 (2022).
58 Boes, A. *et al.* Lithium niobate photonics: Unlocking the electromagnetic spectrum. **379**, eabj4396 (2023).
59 Rueda, A., Sedlmeir, F., Kumari, M., Leuchs, G. & Schwefel, H. G. Resonant electro-optic frequency comb. *Nature* **568**, 378-381 (2019).
60 Reynaud, M. *et al.* Electro-optic response in epitaxially stabilized orthorhombic mm2 BaTiO3. *Physical Review Materials* **5**, 035201 (2021).
61 Zhang, J. *et al.* Ultrabroadband integrated electro-optic frequency comb in lithium tantalate. *Nature* **637**, 1096-1103 (2025).
62 Wang, C. *et al.* Lithium tantalate photonic integrated circuits for volume manufacturing. *Nature* **629**, 784-790 (2024).

Responses Letter to Reviewers

We would like to first sincerely thank all the reviewers for their valuable comments and suggestions for our manuscript. It was fortunate for us to have a chance to further revise our work for further enhancements, accordingly. Below are our responses and revision details.

Responses to Referee 1 and 2:

Comment 1:

I appreciate the additional explanations and experimental data by the authors and have no further comments.

Comment 2:

I co-reviewed this manuscript with one of the reviewers who provided the listed reports.

Response:

We gratefully acknowledge the reviewers for their positive evaluation and constructive suggestions that helped us improve our manuscript all along the journey.

Responses to Referee 3 and 4:

Comment 3:

We would like to thank the authors for the extensive effort they have taken to address the concerns of the reviewers. We acknowledge the impressive work and effort that went into this manuscript and the response, however, we still feel that the work feels dis-jointed, attempting to cover too much material for one article. We don't feel it is appropriate for Nature in it's current form.

Comment 4:

I co-reviewed this manuscript with one of the reviewers who provided the listed reports.

Response:

We sincerely appreciate the careful assessment and considerate comments from the reviewers that greatly helped us to further improve and clarify our manuscript all along. We are also very grateful for the reviewers' positive acknowledgements regarding our work.

We thank the reviewers' thoughtful comment on enhancing the connections of different contents. We have thus carefully revised our manuscript text, accordingly, with reduced main text length but upgraded clarity and cohesion. Specifically, we have carefully rephrased our writing, enhancing the transitions and connections between different sections for a high-coherence story.

Regarding the 'amount of different materials' covered in this paper, we would like to explain and justify this work as the 'platform paper' for the heterogeneous photonic integration of different van der Waals (vdW) 3D nanomembranes. These various freestanding 3D nanomembranes, encompassing a wide spectrum of different material systems with essential optical functionalities for photonic integrated circuits, are unified by the same feature of 'artificially delaminated vdW interfaces' by advanced thin-film lift-off technologies, and the same purpose for 'heterogeneous photonic integration'. This comprehensive library of materials studied in this manuscript is also an exemplary advantage of this proposed vdW integration platform for photonics, with verified feasibility for multiple distinct and general 3D materials thin-films for maximized academic impact. We have thus thoroughly revised our manuscript to illustrate this concept.

Besides, we believe that proposing a viable new photonic platform for coalescing different high-quality functional thin-film materials has proven increasing significance in recent years, such as some prior references examples of Ref: Nature 578, 75–81 (2020), Ref: Nature, 81–87 (2023), and Ref: Nature 630, 346–352 (2024), which also have multiple materials reported in a single paper for integration.

Therefore, we sincerely hope our careful revisions and explanations may help clear the reviewers' concerns. To sum, we have carefully revised our manuscript for enhanced joint connections between different sections. We have thus also highlighted this work as a comprehensive framework on versatile photonic van der Waals (vdW) heterogeneous integration across multiple optoelectronic material systems, where these different nano-membranes are all indispensable functional components, to fit the wide audience and broad potential impact for publication on Nature.